Facilitation of Homogeneous Combustion with Oxygen Enrichment for High-Temperature Industrial Furnaces

by

Kumar Aanjaneya

A dissertation submitted in partial fulfillment
of the requirements for the degree of
Doctor of Philosophy
(Mechanical Engineering)
in the University of Michigan
2020

Doctoral Committee:

Professor Arvind Atreya, Co-Chair
Associate Professor Claus Borgnakke, Co-Chair
Professor Venkat Raman
Professor Margaret Wooldridge

Kumar Aanjaneya

kumaraa@umich.edu

ORCID iD: 0000-0003-1637-3648

Dedication

To my mother, Dr. Rupa Prasad, for a

lifetime of unflinching support, struggle, and sacrifices;

without which, I would not have been a tenth of whatever I am today.

Acknowledgements

Drawing inspiration from the Latin metaphor of dwarfs standing on the shoulders of giants, *"nanos gigantum humeris insidentes"*, Sir Isaac Newton famously wrote *"If I have seen further, it is by standing on the shoulders of giants"* in one of his correspondences with Gottfried Leibniz. While the Bibliography section of this thesis is an acknowledgement of previous researchers, this section presents a small note of thanks to the giants who have made my journey possible.

First, I would like to thank my advisors, Prof. Arvind Atreya and Prof. Claus Borgnakke for all the guidance, motivation, encouragement, and advice throughout my PhD journey. I am thankful to Prof. Atreya for giving me the opportunity to join his research group and especially, for ensuring that nothing was lacking for me even during his struggles on the health front. I am thankful to Prof. Borgnakke for all the insightful discussions we had, even when he was not officially my advisor, and for graciously stepping in and taking official charge during troubled times. I am also thankful to Prof. Venkat Raman and Prof. Margaret Wooldridge for agreeing to serve on my committee and for their astute comments and advice which has helped me a great deal. I have always been amazed by the tremendous depth (and breadth!) of knowledge my committee members possess, and I have always strived hard to be just a little more like them.

I am highly appreciative of Ms. Michelle Barnett, Ms. Rachel Casanova, Mr. Harald Eberhart, Mr. Matthew Jastrzembowski, Prof. Katsuo Kurabayashi, Mr. Matthew Navarre, Prof. Kevin Pipe, Prof. Kon-Well Wang, Mr. Charlie Weger, and Mr. Rick Wintergerst for often going way above and beyond their job descriptions to ensure smooth sailing for me. I owe a special debt of gratitude to Mrs. Liza Atreya for her support in the day-to-day running of the lab when Prof. Atreya was on a medical leave. I am also grateful for the support from Mr. Nick Cantu, Mr. Jonathan Klozik, Mr. Adam Mael, Mr. Matthew New, Mr. Kent Pruss and Ms. Laura Vespaziani.

Former labmates, Dr. Yawei Chen and Dr. Weiyu Cao created an environment in the lab which was highly conducive for academic research and critical thought while keeping everything non-stressful. I will forever cherish the experience of cooperating on experiments and bouncing ideas off of each other. Further, I am thankful to Yawei for his constructive criticism, encouragement, advice, guidance, a profoundly educational internship, and many, many more things than I can recount now.

My friends Aditi, Daljeet, Deepak, Harshad, Keval, Kunal, Mantha, Niket, Priyanka, Ripudaman, Saurabh, Shounak, Shriya, Sneha, and Vaibhav were like a family in Ann Arbor and ensured that I spent a sufficient amount of time outside of the lab indulging in the lighter side of life. A distinct note is owed to Vaibhav, who has been a wonderful roommate from my first day in Ann Arbor to my last. Sneha has been a steadfast source of support and has shepherded me through dark times and I'm especially beholden to her for that. I am thankful to friends not with me in Ann Arbor who have always taken the initiative to stay in touch, particularly because I'm singularly bad at it. Aditya, Dhritiman, Gaur, Gayathri, Saket, Soumyajit, Swayam, Vibhuti, and Vipul have continued to be great friends despite years elapsing between meets.

Finally, a big note of gratefulness goes to my mother (Dr. Rupa Prasad) and sister (Dr. Aparajita Sinha) for an epoch of support, love, motivation, and cheer. My uncles (Mr. Pius Kumar, Mr. Jitendra Sinha, Mr. Birendra Sinha), aunts (Mrs. Renu Kumar, Mrs. Leena Sinha, Mrs. Srishti Sinha), grandfather (Mr. Braj Prasad), grandmother (Mrs. Meena Prasad), and cousins (Shruti, Kruti, Ayush, Harshika, Aishwarya, and Anushka) have been a tightly knit unit and have kept me going through uncertainties with their unending love and good wishes. The mechanical engineers in my family (Mr. Braj Prasad and Mr. Pius Kumar) continue to be a source of inspiration and they are also a major reason as to why I chose this line of study in the first place.

Table of Contents

List of Tables

List of Figures

x

List of Abbreviations

Acronyms

ATAC	Active Thermo-Atmosphere Combustion
CDC	Colorless Distributed Combustion
EDC	Eddy Dissipation Concept
FLOX	Flameless Oxidation
HC	Homogeneous Combustion
HCCI	Homogeneous Charge Compression Ignition
HiTAC	High Temperature Air Combustion
HRR	Heat Release Rate
ISAT	In-Situ Adaptive Tabulation
MILD	Moderate or Intense Low-oxygen Dilution
NTP	Normal Temperature and Pressure
PIV	Particle Imaging Velocimetry
PPMVD	Parts-per-million volumetric on a dry basis
RANS	Reynolds-Averaged Navier-Stokes
RSM	Reynolds Stress Model
SJWJ	Strong-Jet/Weak-Jet
TCI	Turbulence Chemistry Interaction
THC	Total Hydrocarbons
UDF	User Defined Function
WSGGM	Weighted Sum of Gray Gases Model

Symbols

β	Ratio of tangential and axial component of velocity $= U_t/U_a$

ε	Turbulent dissipation rate, Emissivity
λ	Beam wavelength
ϕ	Equivalence ratio
ρ	Density
ρ_{sa}	Scattering to absorption ratio
σ	Standard deviation, Stefan-Boltzmann constant
τ	Reynolds stresses
τ_{flow}	Flow time scale
τ_{chem}	Chemical reaction time scale
μ	Viscosity
A	Cross sectional area
$C_{1\varepsilon}$	$k - \varepsilon$ model constant
C_{ξ}	Volume fraction constant (EDC)
C_{τ}	Time scale constant (EDC)
C_o	Initial concentration of reactant
c_o	Speed of light in vacuum
C_p	Specific heat capacity
d	Diameter of nozzle
Da	Damköhler number
d_i	Inner diameter
d_o	Diameter of oxidizer jet, outer diameter
h	Convective heat transfer coefficient, Planck's constant
$E_{\lambda,b}$	Spectral emissive power
J	Jet momentum $= mU_{av}$
f_v	Soot volume-fraction
I	Intensity of incident beam
I_o	Baseline intensity of beam
k	Boltzmann constant
k_f	Kinetic reaction rate constant (forward reaction)

k_r	Kinetic reaction rate constant (reverse reaction)
k_{ext}	Extinction function
L	Path length
l_{stag}	Stagnation length
m	Mass flow rate, Soot refractive index
m_r	Mass flow rate of recirculated gases
M_r	Momentum ratio $= J_o/J_f$
n	Order of reaction
q	Radiative heat-flux
q_{sp}	Heat release rate
r	Radial coordinate
Re	Reynold's number
r_s	Radius of soot particle
S	Swirl number $= 0.75\beta$
T	Temperature
T_{auto}	Auto-ignition temperature
T_{in}	Mass-weighted average temperature of fresh reactants at inlet
v_y, U	Velocity component along nozzle axis
U_a	Axial component of the velocity
U_t	Tangential component of the velocity
X	Mole fraction
Z	Axial distance downstream from nozzle exit, Axial coordinate

Subscripts

av	Averaged property
c	Property in the axial direction along nozzle axis line
f	Property at fuel nozzle exit
g	Property pertaining to the gaseous domain
gs	Property pertaining to the gas-soot domain

stag	Property in the horizontal plane containing the stagnation point
o	Property at oxidizer nozzle exit
s	Property pertaining to soot
w, wall	Property pertaining to the furnace wall

Abstract

A substantial portion of literature discussing highly efficient and low pollutant emission combustion systems comprises of Homogeneous Combustion (HC) or its variants (MILD, FLOX, CDC etc.). Qualitatively, they have: (i) a homogeneous reaction zone (small gradients of temperature and composition) and (ii) the absence of visible (or audible) flame fronts. The underlying theory among all of the aforementioned methods is the reduction of the Damköhler number (Da) to the order of unity. To attain high temperatures, industrial heating is often accomplished by using "enriched" oxidizer streams i.e. $X_{O2} >$ 21%. Extending the concept of HC to applications of industrial heating (e.g. glass melting furnaces) is a desirable but a challenging task. Higher reactant concentrations increase reaction rates. Fast reactions lead to an increase in temperature which in-turn accelerates the reaction rates and the heat release rate. This self-accelerating cycle causes a shift to the conventional mode of combustion (higher Da) with high NOx emissions. The broad research goal in this work is to keep $Da \sim 1$ to facilitate HC with enriched oxidizers.

The first strategy employed towards this was to enhance the heat removal from the reaction zone by enabling the presence of soot in the reaction zone. The conjecture was that presence of soot will augment heat radiation, reduce temperatures, and reduce NOx emissions; similar to what has been reported for highly luminous flames. Since natural gas (methane) does not soot except under high pressure environments, fuel blends containing small amounts of lightly sooting fuels like ethylene were investigated. It was found that while the presence of soot definitely improves radiation heat transfer and reduces specific NOx emissions, there is an optimal blend level. A multi-variate regression model was used to demarcate the radiation emanating from the wall and from the gaseous zone.

The second strategy employed was to engineer the flow in the furnace to enhance mixing and reduce Da. Experimentally studying the confined turbulent jet(s) flow in the furnace with limited optical access was infeasible and hence computational simulations

were utilized. A number of steps to reduce computational expenses were taken. These included utilization of furnace symmetry and writing external code to describe furnace recuperator operation. The 3-D flow within the furnace was described/understood by breaking it into a set of canonical flows. The utilization of a detailed mechanism (GRI Mech-3.0) enabled accurate capture of the NOx field to within a few ppm. It was discovered that optimizing geometry and flow is important to achieve HC with enriched oxidizers.

The third strategy focused on further enhancing jet dilution by modifying nozzle design. It was found that altering the nozzle shape caused essentially no reduction in NOx emissions from the furnace. It was also found that NOx emissions were independent of the inlet temperature of the reactants. Another strategy was to have a localized swirling injection for the oxidizer jet. While swirl did help in reducing NOx, there existed an optimal swirl number beyond which NOx emissions were aggravated to levels even higher than configurations with no swirl. Swirl, even though localized, was seen to affect the in-furnace flow even in the far-field (~75 diameters). A mutual competition was seen between swirl assisted and entrainment driven dilution; and at higher swirl intensities, the reduction in the latter overwhelmed the gains accrued by the former (in terms of NOx emissions). Other pollutants studied (THC and CO) were also found to be dictated by the same considerations as NOx, namely, oxygen content in the oxidizer stream and mixing.

Chapter 1:

Introduction

1.1 Background and Motivation

The scientific community continues to remain in pursuit of increasingly efficient utilization of energy resources and minimization of associated pollutant emissions. According to the *"Annual Energy Outlook"* released by the U. S. Energy Information Administration in 2015, the net consumption of energy in the US in the calendar year 2014 was approximately 97.1 quad[1] which is expected to grow to 105.7 quad in 2040 [1].
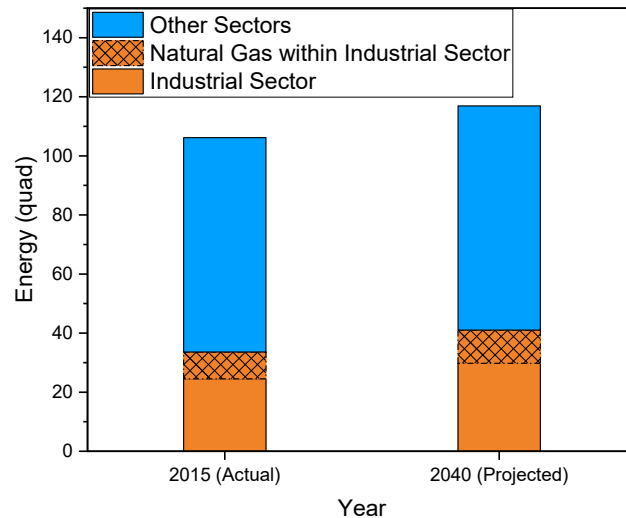
Figure 1.1: Current and future (expected) energy usage by sector.

The amount of energy consumed in the industrial sector was 24.5 quad and expected to grow to 29.8 quad. Within the industrial sector, natural gas constitutes approximately 37% of both the aforementioned numbers. It can therefore, be concluded that the combustion of natural gas in industrial settings forms a significant proportion of the net energy use in the nation. Most of this natural gas is used to fuel furnaces to serve

---

[1] quadrillion BTU = 10^{15} BTU = 2.93 x 10^{11} kWh

industrial heating needs and since these furnaces operate at high temperatures, they are a major source of NOx emissions; which are produced chiefly via the *"thermal"* route or Zel'dovich mechanism [2]. This calls for continuing research into newer combustion technologies to make them more efficient while having little accompanying pollutant emission penalties.

1.2 Thermal Route or Zel'dovich Mechanism

One of the first explanations of NOx formation in flames was provided by Zel'dovich in 1946. It was theorized and shown that NOx formation took place primarily in the high temperature regions of flames and that this process was highly sensitive to temperature; the explicit relation being that higher temperatures favor forward reactions (see Table 1.1). This mechanism was later expanded by Lavoie et al. with the inclusion of a reaction of atomic hydrogen with a hydroxyl radical.

Table 1.1: Thermal NOx pathways.

Reaction	k_f (m³/gmol s)	k_r (m³/gmol s)	Reference
$O + N_2 \rightleftharpoons N + NO$	$1.8 \times 10^8 e^{-38370/T}$	$3.8 \times 10^7 e^{-425/T}$	Zel'dovich [2]
$N + O_2 \rightleftharpoons O + NO$	$1.8 \times 10^4 e^{-4680/T}$	$3.8 \times 10^3 e^{-20820/T}$	Zel'dovich [2]
$N + OH \rightleftharpoons H + NO$	$7.1 \times 10^7 e^{-450/T}$	$1.7 \times 10^8 e^{-24560/T}$	Lavoie et al. [3]

1.3 Low Damköhler Number Combustion

Damköhler number (*Da*) is defined as the ratio of the reaction rate to that of the advective transport (mixing) rate (or that of the respective inverse time scales). For a general n$^{\text{th}}$ order chemical reaction A → B, the Damköhler number for a convective flow system is:

$$Da = kC_0^{n-1}\tau_{flow} = \frac{\tau_{flow}}{\tau_{chem}}$$

In conventional combustion with sharp spatial and temporal gradients in temperature fields, species distributions, and other parameters, Da tends to ∞ (Burke Schumann limit). These sharp gradients are manifested in the form of flames where the temperatures are high and consequently NOx formation is aggravated.

A substantial portion of literature discussing highly efficient and low emission combustion systems comprises of techniques which enable combustion with low Damköhler numbers. Different authors have used/coined different terms for subtly different but fundamentally similar processes. Qualitatively, they have a homogeneous reaction zone (small gradients of temperature and composition) and an absence of visible (or audible) flame fronts. Quantitatively, Damköhler number (Da) is controlled to be of the order of unity by intense dilution with products of combustion [4]. MILD (Moderate and Intense Low Oxygen Dilution combustion) [5–10] and HiTAC (High Temperature Air Combustion) [11–13] involve intense dilution and heating of the oxidizer stream with exhaust gases generally with high levels of external preheat. Preheat is important to ensure ignition even under ultra-dilute conditions. This technique extended to Gas Turbines has been called CDC (Colorless Distributed Combustion) [11,14–16] as the reaction zone is largely transparent and volumetrically distributed but with much higher volumetric HRR as compared to the other variants. When initially developed for 2-stroke engines, it was named ATAC (Active Thermo-Atmosphere Combustion) [17,18]; now known as HCCI (Homogeneous Charge Compression Ignition) [19–21], a term used for 4-stroke engines. FLOX (Flameless Oxidation) [22–28] is another popular name which is used to refer to volumetrically distributed oxidation of fuel with no visible (or audible) flame fronts.

1.4 Research Motivation, Objective and Outline

In applications such as engines or gas turbines, since the useful output is mechanical work, low temperature reactions are an excellent way to combat NO_x emissions; although it comes with its own set of challenges. However, in high temperature applications (such as steel or glass melting furnaces) where the goal is to heat materials (and also cause phase changes in some cases), it becomes imperative to have high temperature combustion. Such high temperatures are conventionally achieved by using enriched oxidizers ($X_{O2} > 21\%$)

for combustion [29–31]. Higher concentration of reactant species (oxygen) would accelerate reaction rates, thus increasing Da and causing a shift to conventional combustion with high NOx emissions. Additionally, less momentum being injected via the oxidizer stream (due higher oxygen concentration) would reduce mixing rates; thus increasing Da further. The overarching research goal for this work is to maintain low Da regime and hence low NOx operation while running with enriched oxidizers.

With the notable exception of a few [26,32], a majority of studies reporting oxy-fuel combustion in the HC (or MILD) regime do not use methane/natural gas as fuel. Biogas [33,34], propane [22], light-oil [35], and most prominently, coal [35–38] have been investigated with different levels of oxidizer enrichment by researchers. Methane (natural gas) is the most industrially relevant fuel (especially in the US [1]) and thus, further investigations are needed with industrial feasibility kept in mind.

1.5 Experimental Facility

The furnace used for the study consists of three parts as shown in Figure 1.2 and listed below:

- Main chamber
- Annular exhaust vent
- Preheat zone/recuperator

The furnace has a parallel jet configuration with four oxidizer jets arranged in a circle of radius $17.5d_o$ around the centrally located fuel jet. Reactants are injected vertically downwards into the main chamber where combustion takes place. Then the products travel radially outward through the exhaust ports and upwards through the annular exhaust vent. The hot gases exchange heat with the incoming reactants via metallic pipes (only one shown in Figure 1.2) in the preheat zone before leaving the furnace. Meanwhile, a water-cooled bottom plate simulates a thermal load which is typical of industrial furnaces.
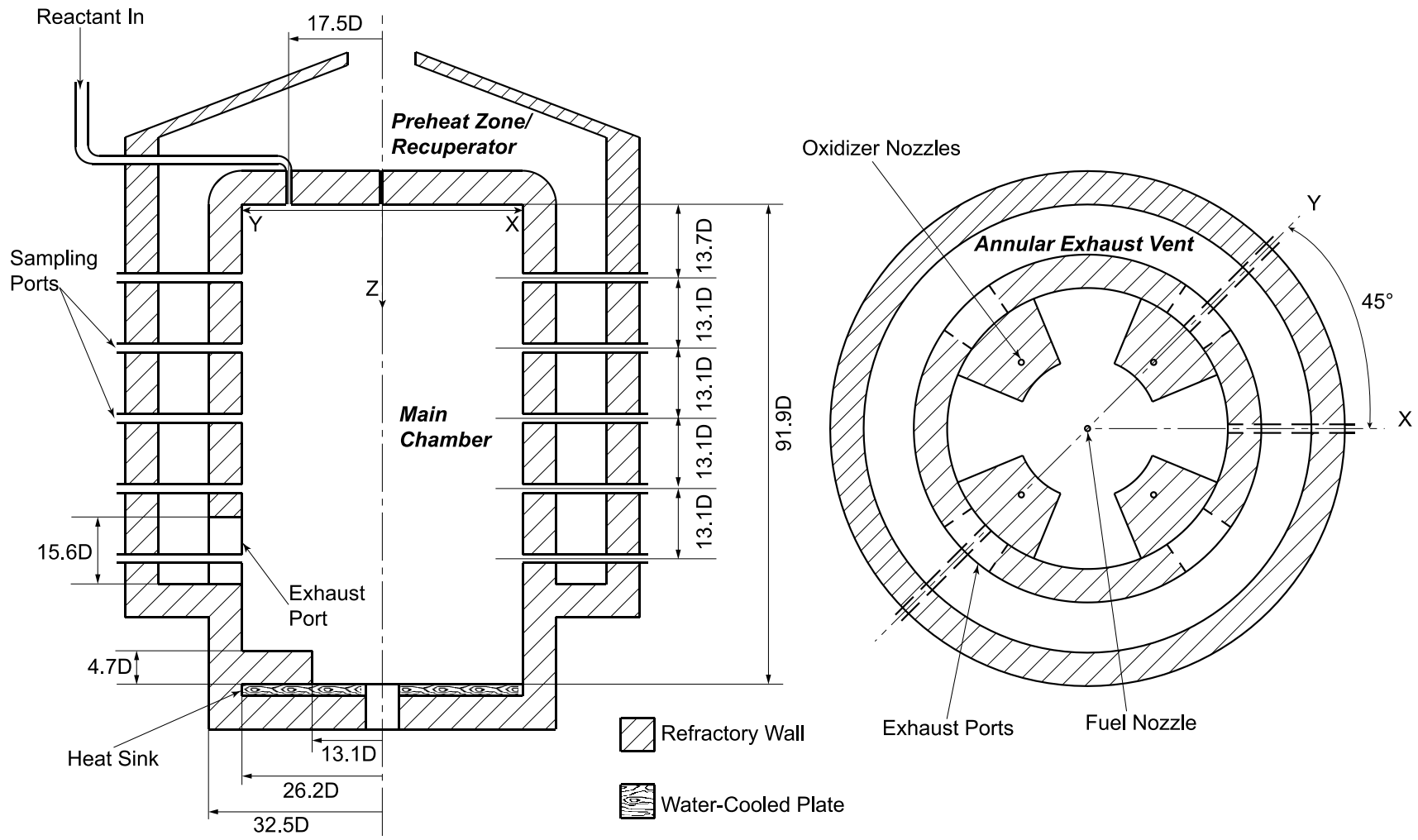
Figure 1.2: Furnace geometry ($D = d_o$ = 16mm)

There are three sets of radial ports to allow introduction of sampling probes. Two of the sets are located in a plane containing the central axes of oxidizer and fuel jets (referred to as the "Y-plane") while one set is located in a plane $45°$ to the Y-plane (referred to as the "X-plane"). These ports are located at distances of 220 mm, 430 mm, 640 mm, 850 mm, and, 1060 mm from the main chamber ceiling and are called Port 1, 2, 3, 4, and 5 respectively. During operation of the furnace, the ports are kept covered with cork plugs to ensure no introduction of ambient air into the main reaction chamber. The sampling probes are designed such that an airtight sealing exists between the probe and the port during the process of sampling. The furnace has been designed with practical implementation being a major consideration. Some highlights and comparisons with available literature are summarized in Section 3.2 and 3.3.1.

1.6   Thesis Outline

As mentioned in Section 1.4, the overarching goal of this thesis is maintaining low *Da* operation even with enriched oxidizers. The thesis discusses three strategies and their effectiveness towards this. They are as follows:

- Chapter 2: Arresting thermal runaway conditions by enhancing radiative heat transfer from the reaction zone.
- Chapter 3: Effect of the flow field, and specifically, the fuel nozzle diameter on NOx emissions from the furnace.
- Chapter 4: Effect of locally swirling injection and modification of nozzle shape on furnace homogeneity and NOx emissions.

The final chapter, Chapter 5 summarizes conclusions, limitations, and suggestions for future work in this field.

Chapter 2:

Enhancing Radiation With Soot

2.1   Research Problem: Thermal Runaway

Under normal conditions, combustion reactions are fast compared to molecular mixing and take place in layers that are much thinner than the typical diffusion or turbulent mixing length scales. These thin layers are manifested as flames and are the sites for thermal NOx formation [2]. Fast reactions lead to an increase in temperature which in-turn accelerates the reaction rates (and the heat release rate until it is balanced by the heat loss rate). This self-accelerating cycle (Figure 2.1) leads to "Thermal Runaway" conditions, which causes the formation of flames; and so, it must be altered to get homogeneous combustion where the reaction is volumetrically distributed. The reaction rates are also further increased for enriched oxidizers which are commonly utilized for industrial heating needs. Therefore, additional measures are needed to maintain oxy-enriched Homogeneous Combustion. A potential method to inhibit the cycle can be operation with lean premixed reactants. However, this would introduce additional safety issues. Additionally, lean mixtures would increase the content of non-radiative species (O_2, N_2) relative to the radiative species (H_2O, CO_2) in the reaction zone; which will impose an efficiency penalty.
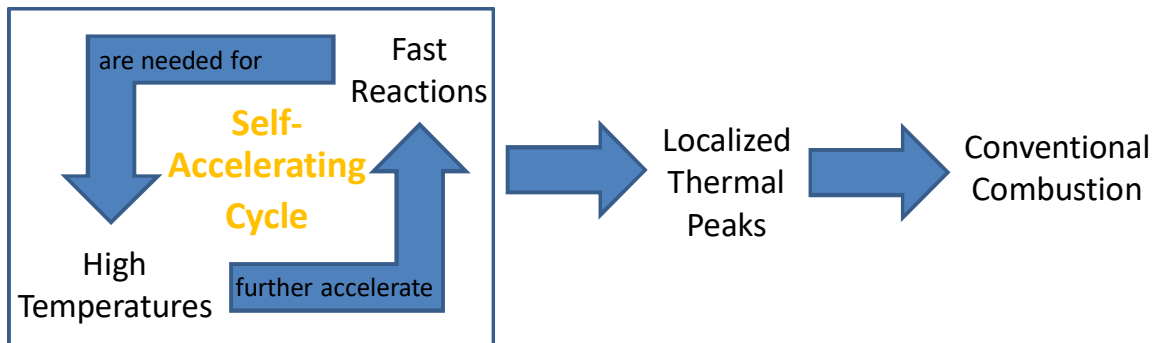
Figure 2.1: Research problem.

2.2   Proposed Solution: Soot Radiation

Radiation is the most effective mode of heat transfer in the high temperature regime under consideration. Carbon dioxide and water are radiative species and transfer most of the heat away from reaction zones [39–41]. To inhibit thermal runaway conditions, a proposed strategy is the enhancement of heat removal rates from the reaction zone (Figure 2.2). This enhancement can be brought about by the presence of soot particles as they have much higher emissivity than combustion product gases. Typical values for gas are $\varepsilon_g \approx$ 0.015 and for soot, $\varepsilon_s \approx 0.70$. The conjecture is that presence of soot will augment heat radiation, reduce temperatures, and reduce NOx emissions; similar to what has been reported for highly luminous flames [30,42–45]. Previous work involving soot with HC/MILD/FLOX combustion has largely looked at soot as a pollutant [5,46]; and consequently the focus has been on ensuring soot suppression. A novel aspect of this work is promotion of soot production and attempting productive usage of soot in the HC regime.

Fast Reactions → High Temperatures → Volumetrically Distributed Combustion

Faster Heat Removal
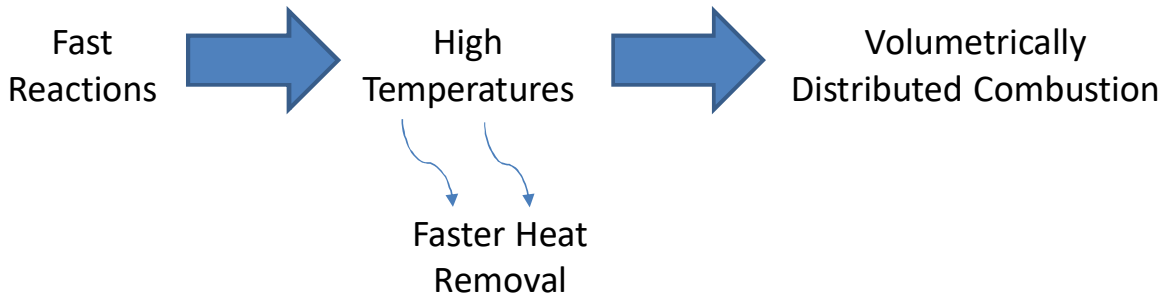
Figure 2.2: Proposed solution.

Since natural gas (methane) does not soot significantly except under high pressure environments [44], fuel blends containing small amounts ethylene ($X_{C2H4} \leq 20\%$) are investigated; which is selected as it is a lightly sooting fuel. Oxygen enriched combustion enhances furnace performance [41] due to increased concentration of radiative species (CO_2 and H_2O) and decreased concentration of non-radiative species (N_2). Increased radiation due to soot is expected to further boost furnace performance. This conjecture is tested, and the results are analyzed.

2.3   Experimental Set-up and Methods

2.3.1   Experimental conditions

A total of eight cases are tested by varying the oxidizer and fuel streams' compositions at a constant heat input of 91.7 kW and globally rich equivalence ratio (ϕ = 1.1). The compositions and names used to refer to individual cases are listed in Table 2.1.

Table 2.1: Inlet streams' composition for experiments.

Composition	$X_{C2H4} = 0\%$	$X_{C2H4} = 10\%$	$X_{C2H4} = 15\%$	$X_{C2H4} = 20\%$
$X_{O2} = 21\%$	NO21	E10O21	E15O21	E20O21
$X_{O2} = 30\%$	NO30	E10O30	E15O30	E20O30

Heat-flux, soot, temperatures, and gas species' measurements are taken and averaged over one minute each. These measurements are taken after ensuring wall and cooling water temperatures have attained a steady state; which is approximately 2 – 3 hours after furnace start up.

2.3.2   Soot measurement

A laser beam-extinction based measurement system (Figure 2.3) is constructed to measure the soot content in terms of line-of-sight averaged (in the radial direction) volume-fractions. These measurements are taken through five ports at different axial locations (see Section 1.5). A 532 nm (green), 10 mW photodiode laser beam is passed through an optical chopper rotating at a frequency of 1 kHz. The chopped beam passes through a 1:20 beam expander so that the beam extinction in the combustor takes place over a volume that is almost 400 times the volume without beam expansion. Thus, it results in a number which is a better representative of the soot volume-fraction. This widened beam is then reflected by a mirror (mounted at an angle of 45° to the vertical) through a port into the furnace where it undergoes attenuation and comes out via a diametrically opposite port. Another mirror reflects this beam onto a plano-convex lens which focusses it onto the receiver. A lock-in amplifier conditions the signal to eliminate ambient noise by filtering out all signals not at the chopper frequency. The mirrors are mounted on sliding posts so that measurements can take place at different axial locations within the furnace.

A derived form of the well-known Bouguer's and Lambert-Beer Laws, akin to those used in previous literature [47–49], is used to post-process the data. The baseline intensity I_o and the attenuated intensity I are determined experimentally and yield a soot volume-fraction after being processed through Equations (2.1), (2.2), and (2.3). The baseline intensity I_o is determined without combustion in the furnace.

$$E(m) = -Im\left[\frac{m^2 - 1}{m^2 + 2}\right] \tag{2.1}$$

$$k_{ext} = \frac{ln\left(I_o / I\right)}{L} \tag{2.2}$$

$$\frac{f_v}{k_{ext}} = \frac{\lambda}{6\pi E(m)} \cdot \frac{1}{1 + \rho_{sa}} \tag{2.3}$$

Because of the types of fuel, the concentrations of sooting component in the fuel (X_{C2H4}), and the equivalence ratio under consideration (Section 2.3.1), the assumption of Rayleigh limit (particles much smaller than beam wavelength; $\frac{2\pi r_s}{\lambda} \ll 1$) is reasonable. As a consequence of the Rayleigh limit assumption, intensity attenuation due to scattering can be assumed to be small. Thus, the scattering-to-absorption ratio can be neglected ($\rho_{sa} \rightarrow 0$) with less than 4% error in the soot volume-fraction [44,50–53].
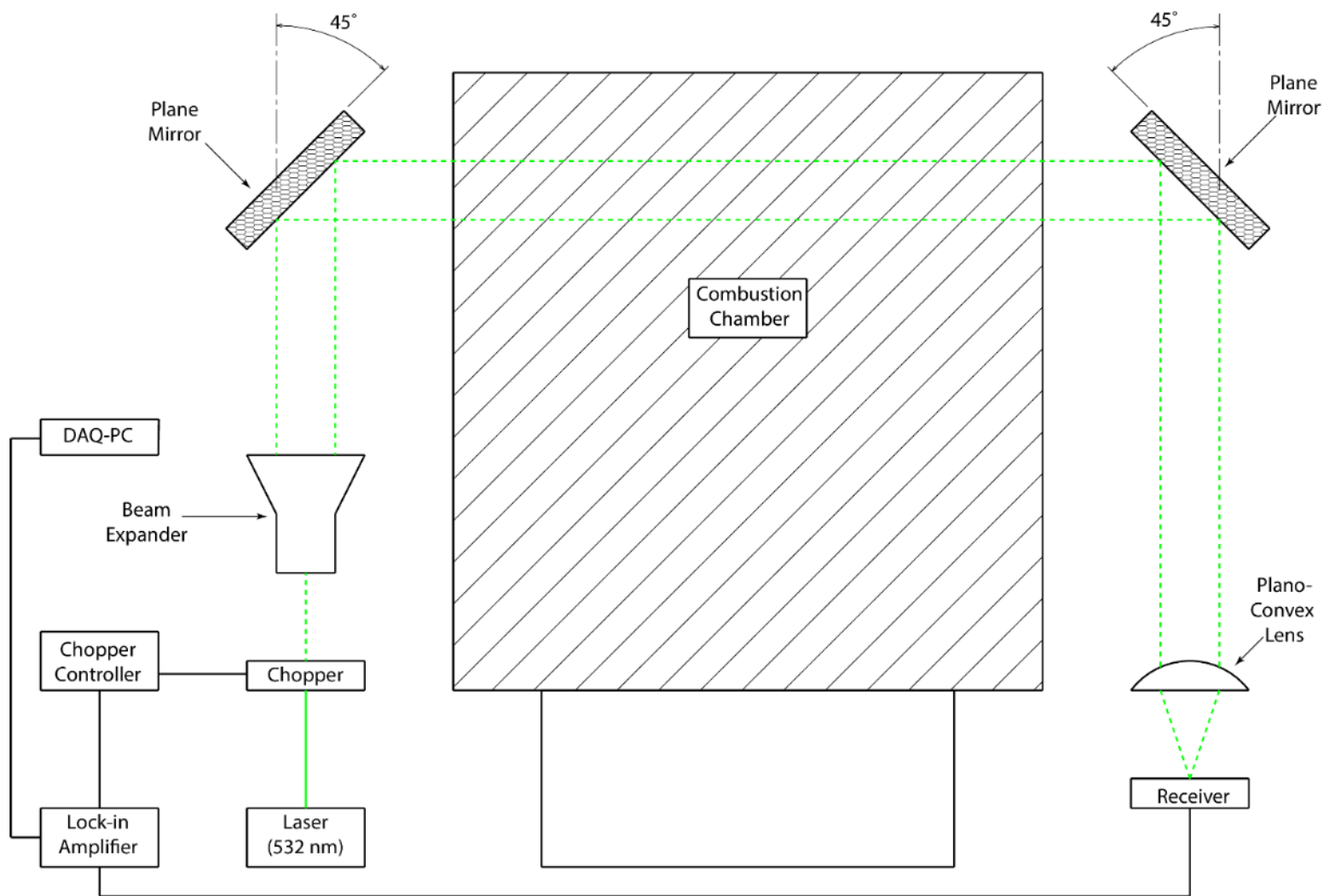
Figure 2.3: Schematic of the laser-extinction based soot measurement system.

The refractive index of soot and variation of its values with various parameters is a topic of contentious debate in literature. While the best known and most widely used value is the one given by Dalzell and Sarofim ($m = 1.57 - 0.56i$) [52,54], multiple other authors have reported different values (listed in Table 2.2).

Table 2.2: Soot refractive index values in literature.

Authors	m	$1/E(m)$	% difference in $1/E(m)$ as compared to Dalzell et al. [54]
Lee et al. [50]	$1.92 - 0.49i$	5.88	52.7
Wu et al. [55]	$1.73 - 0.53i$	4.76	23.6
Charalampopoulos et al. [56]	$1.75 - 0.54i$	4.76	23.6
Hu et al. [57]	Not reported	4.35	13.0
Wu et al. [55]	$1.73 - 0.59i$	4.17	8.3
Dalzell et al. [54]	$1.57 - 0.56i$	3.85	0.0
Choi et al. [53]	$1.57 - 0.56i$	3.85	0.0
Krishnan et al. [58]	$1.95 - 0.88i$	3.57	-7.3
Yang et al. [59]	$1.62 - 0.66i$	3.45	-10.4
Williams et al. [49]	$1.75 - 1.03i$	2.70	-29.9

Numerous researchers have also tried to determine the wavelength, temperature, and chemistry dependence of soot refractive index. However, the existence/absence of these dependencies is also inconclusive. Some have reported considerable wavelength dependence [60,61], others report no or negligible deviations with wavelength [58,62]. Similarly temperature dependence [56,63], temperature independence [50], chemical composition (fuel, ϕ, C/H ratio) dependence [54,56,63], and chemical composition independence [50,55,58,64] are also reported. Although the value of soot volume-fraction obtained by using Equations (2.1), (2.2), and (2.3) is highly sensitive to the value of soot

refractive index, this sensitivity is manifested only in the form of an upscaling or a downscaling; the underlying trend remaining unaffected. Since the value given by Dalzell and Sarofim [54] is most widely used, and also happens to yield a $1/E(m)$ that is (rudimentarily) close to a median of the values available in literature, it is selected for this work.

2.3.3 Heat-flux measurement

A Schmidt-Boelter sensor is utilized to measure the radiative heat-flux at the same five locations where soot volume-fractions are measured (schematic shown in Figure 2.4). The gauge has a sapphire window which ensures the measurement of only the radiative portion of the net incident heat-flux.
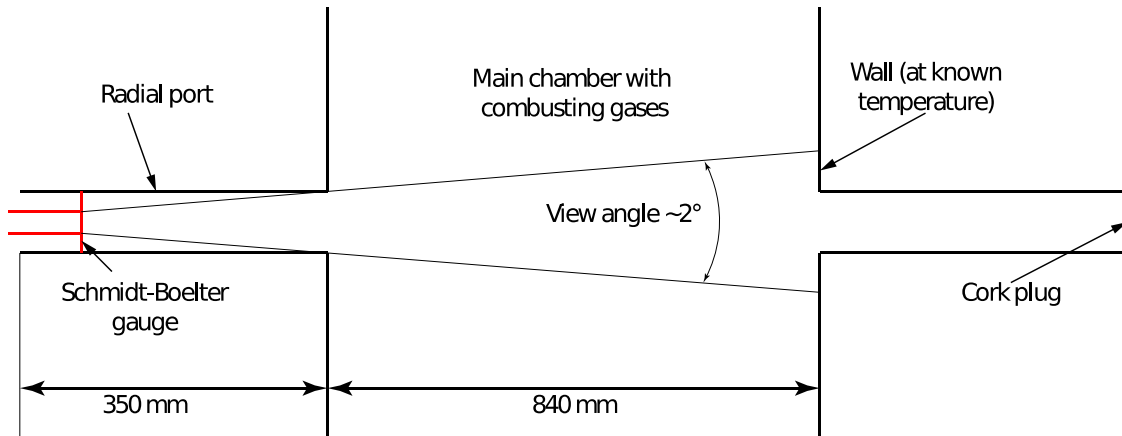
Figure 2.4: Heat-flux measurement schematic.

The gauge was manufactured by the *Medtherm Corporation* (model number 64P-5-24) and some details are as follows:

- Water-cooled
- 150° view angle (reduced to 2°; see Figure 2.4)
- Range of 0 – 5 Btu/ft^{2}sec (0 – 5.7 W/cm^2)
- NIST calibrated (responsivity: 0.2959 Btu/ft^{2}sec/mV)
- Linear response up to 110% of range maximum
- Wavelength range 200 – 5500 nm
- Time constant of 250 ms

13

The wavelength band mentioned above omits a large portion of the infrared (IR) region of the electromagnetic spectrum (700 nm – 1 mm). Soot emits in the continuous spectrum and as an initial approximation may be treated as a black body. For such a hypothetical blackbody, the amount of heat-flux not captured by the heat-flux gauge is quantified using the concepts of band emissions. The fraction of emitted radiation heat-flux in the 200 – 5500 nm band is calculated using Equation (2.5) and plotted as a function of temperature in Figure 2.5.

Using Planck distribution to calculate the spectral emissive power of a diffuse emitter:

$$E_{\lambda,b}(\lambda,T) = \frac{2\pi hc_o^2}{\lambda^5 \left(e^{hc_o/\lambda kT} - 1 \right)} \tag{2.4}$$

$$F_{\lambda_1 \to \lambda_2} = \frac{\int_{\lambda_1}^{\lambda_2} E_{\lambda,b} d\lambda}{\int_0^\infty E_{\lambda,b} d\lambda} \tag{2.5}$$
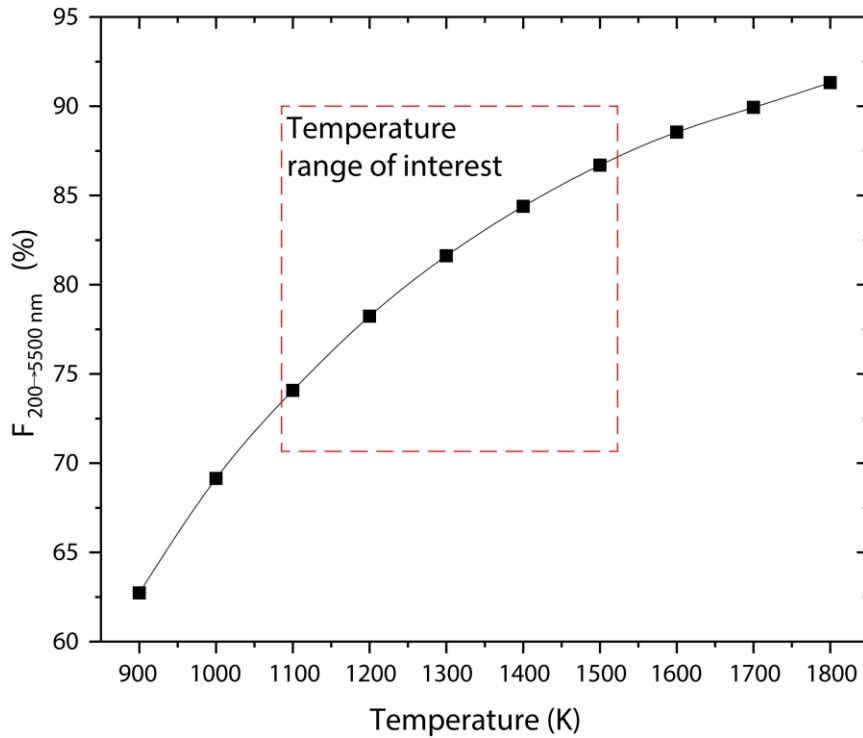
Figure 2.5: Emission fraction in the 200 - 5500 nm band.

For all the cases reported in Section 2.4, the measured (and corrected for radiation) temperatures of the gaseous zone are in the range of 1100 – 1500 K. The gases and soot

particles are expected to be in local thermal equilibrium, and so the heat-flux gauge is estimated to be capturing ~75% of the heat-flux emitted by soot in the worst-case scenario.

Although it was slightly crude, another step was taken to ensure that the experimental data more closely represented the effect of soot on radiative heat-flux. Through analytical reasoning and simple (skeletal chemistry) CFD computations, it was determined that the oxidizer-jets impinged on the plate at a location vertically below the oxidizer nozzles. And so, in these regions the convection heat transfer was the highest. Glass-wool refractory blocks were placed on the water-cooled plate to reduce the net heat transferred via convection (shown in Figure 2.6) and have heat removed by water to be more representative of radiation heat transfer.
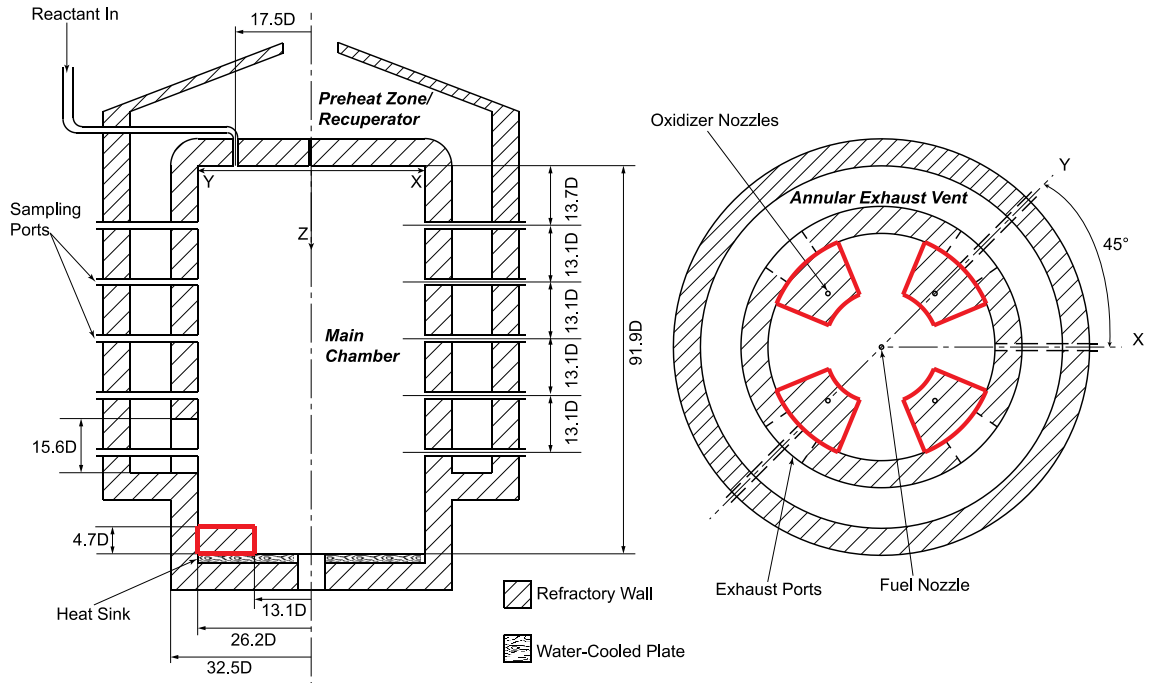
Figure 2.6: Glass-wool refractory blocks (marked in red) on water-cooled plate.

2.4   Results and Discussion

The measured soot volume-fraction (at axial locations described in Section 1.5) for $X_{O2} = 30\%$ cases are in general higher than $X_{O2} = 21\%$ (Figure 2.7). This can be attributed to:

- Higher temperatures aiding fuel pyrolysis and soot precursor (PAH) formation.
- Higher residence times due to lower volumetric flow rates allowing particle agglomeration and growth.

Higher O_2 may be expected to result enhanced soot oxidation rates. Soot is generally oxidized upon being attacked by the OH radical [42,65]. However, as compared to hydrocarbon chain branching or transfer reactions [66] the oxidation reaction is not the favored reaction for the radical.

(a) Soot f_v for X_{O2} = 21%   (b) Soot f_v for X_{O2} = 30%
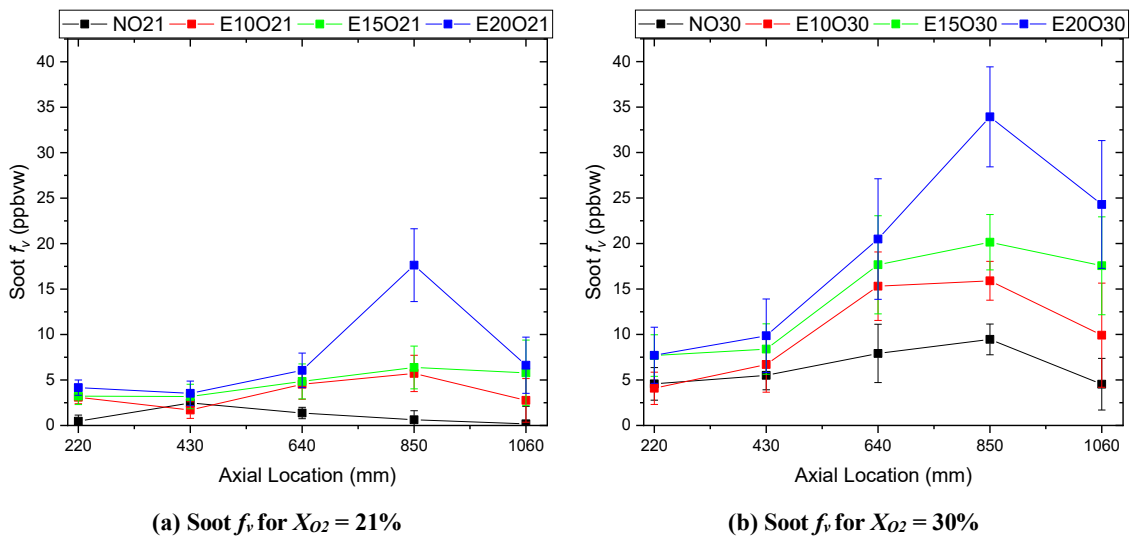
Figure 2.7: Soot volume-fractions at different axial locations.

The error bounds in Figure 2.7 are calculated using the standard deviation of the data sampled over one minute as $\overline{f_v} \pm 1 \times \sigma_{fv}$.

Heat-flux values are presented in Figure 2.8[2] (which has error bounds of the order of the size of the symbol). It is apparent that there is a trend of higher heat radiation for cases with higher soot content. However, this trend is followed only until $X_{C2H4} \leq 15\%$. Beyond that, a drop in q_{rad} values is observed along with appearance of flames (visually observed) in the furnace. This happens as ethylene is an unsaturated hydrocarbon with higher reactivity than methane; and at high enough concentrations shifts the mode of combustion away from homogeneous. This increase is also more noticeable in the Y-plane

---

[2] Due to a lack of optical access, soot volume-fraction measurements were not performed in the X-plane; so no corresponding soot content values are available for Figure 2.6(b) and (d).

as compared to the X-plane. The Y-plane is expected to have higher HRR as it contains the fresh-reactant jets. So this can be a presumptive indication of higher HRR being balanced by higher radiation until a definitive causation has been established between soot volume-fractions and radiative heat-fluxes. Also, the heat-flux values are higher for $X_{O2} = 30\%$ than $X_{O2} = 21\%$ cases. Attributing this to just higher soot content needs a more thorough analysis as this may have been caused by other factors like:

- Higher gas temperatures.
- Higher concentration of CO_2 and H_2O.

Two analyses are performed to establish this relationship and they are discussed in sections 2.4.1 and 2.4.2. Attempts were made to build a detailed radiation model, but these attempts failed; due to the presence of too many unknown parameters (intensity attenuation in gaseous zone, effect of flow, shape factors, wall emissivity, and gas volume geometry). Therefore, statistical tools (aided by physical insight) are utilized for the study.
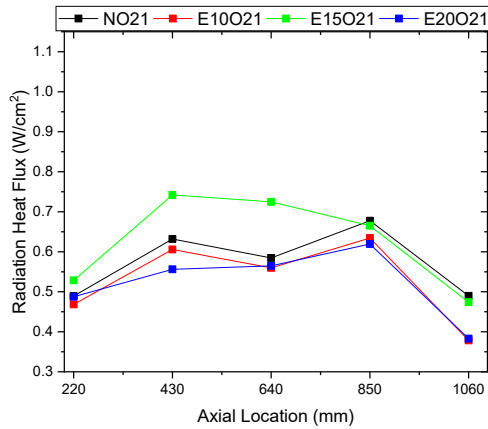
(a) Heat-flux in Y-plane[3] $X_{O2} = 21\%$ **(b) Heat-flux in X-plane**[4] $X_{O2} = 21\%$
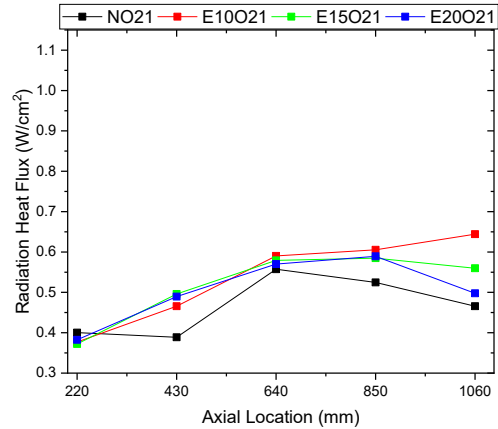
---

[3] plane passing through central axes of the fuel jet and the oxidizer jet (see Figure 2.6).
[4] plane at a 45° angle to the y-plane (see Figure 2.6).
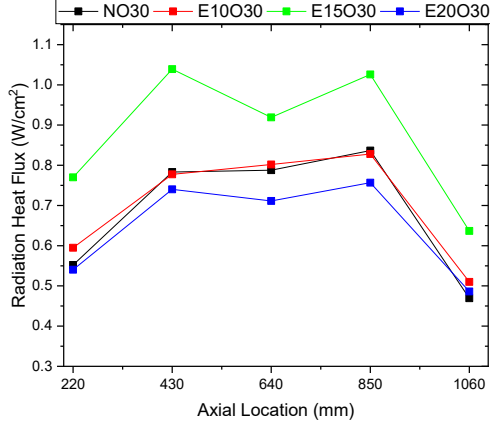
(c) Heat-flux in Y-plane X_{O2} = 30%.   **(d) Heat-flux in X-plane X_{O2} = 30%**
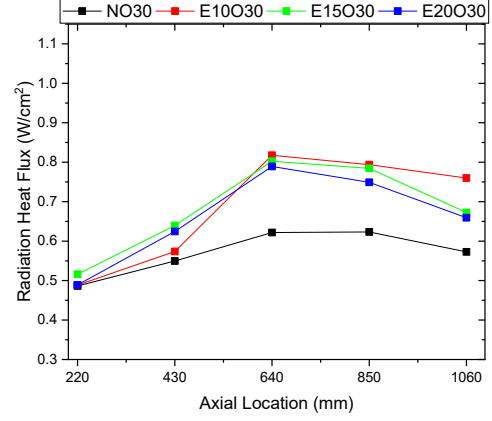
Figure 2.8: Radiation heat-flux.

2.4.1   Direct correlation

From Figure 2.9(a), it can be seen that there exists a definite positive correlation between soot volume-fraction and radiative heat-flux. Considering the gas-soot domain as a homogeneous phase with an averaged emissivity ε_{gs}:

$$\varepsilon_{gs} \propto f_v \tag{2.6}$$

and it is known that,

$$q_{rad} \propto \varepsilon_{gs} \tag{2.7}$$

Using equations (2.6) and (2.7), a linear relationship is inferred between q_{rad} and f_v, and hence, a linear fit is performed. During the experiments, cases with X_{C2H4} = 20% were found to have flames in large portions of the furnace. Other parameters (Figure 2.13) also showed abrupt changes (as compared to $X_{C2H4} \leq 15\%$ cases). It was deduced that E20O21 and E20O30 were being dictated by substantially different physics and therefore outside the scope of the simplistic descriptions offered by Equations (2.6) and (2.7). Consequently, the curve fits were performed for only $X_{C2H4} \leq 15\%$ cases.

The curve fits and the corresponding R^2 values are presented in Figure 2.9(b)-(f). Decently high R^2 values indicated a strong dependence of q_{rad} on f_v. It can further be seen from Figure 2.9(b)-(f) that X_{C2H4} = 20% cases show a large deviation from the general trends and the trendline.
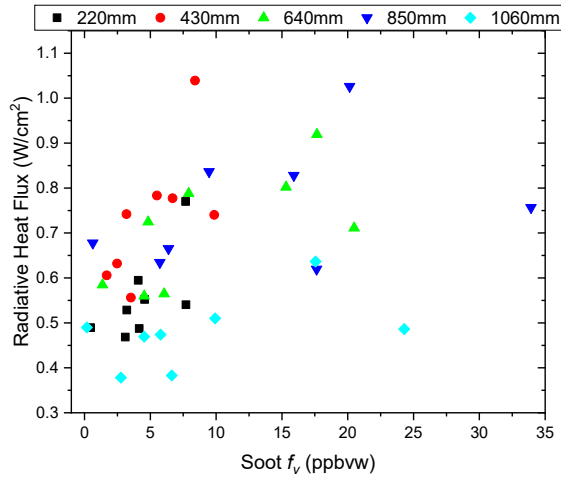
(a) All data points
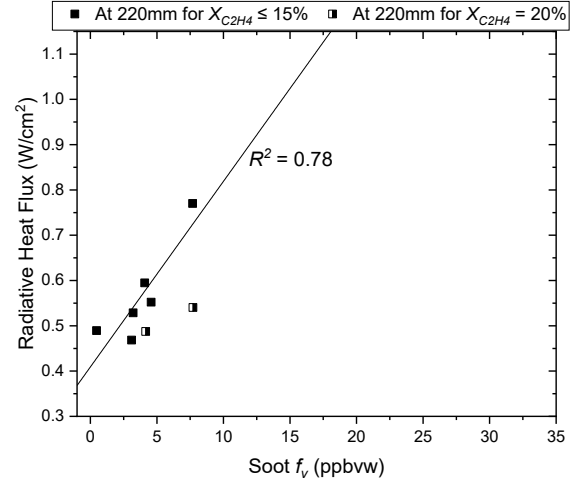
(b) Port 1
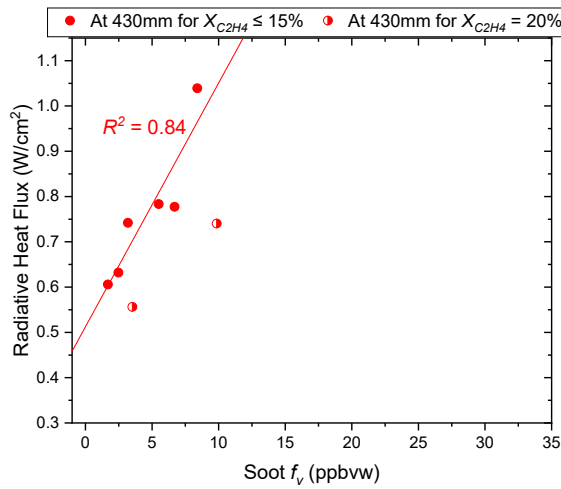
(c) Port 2
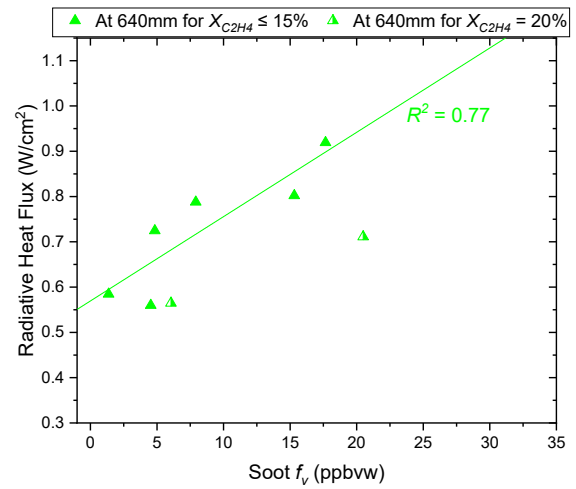
(d) Port 3
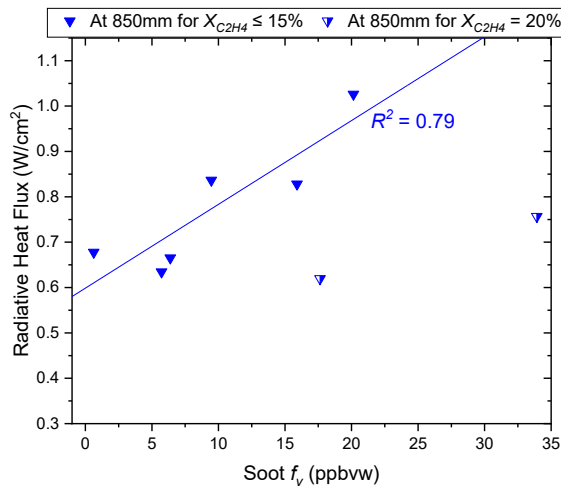
(e) Port 4
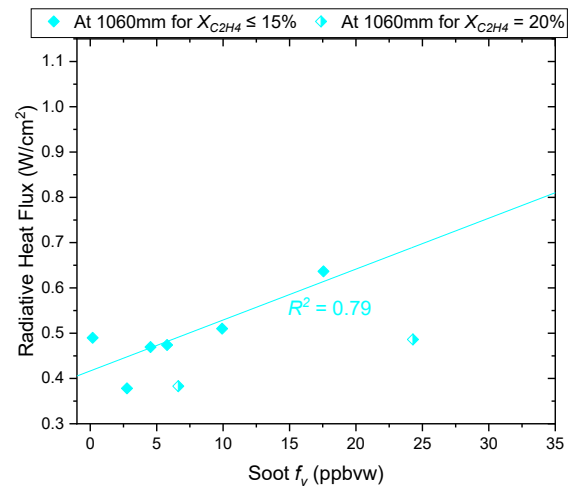
(f) Port 5

Figure 2.9: Soot volume-fraction and heat-flux (distances from furnace ceiling).

2.4.2 Multi-variate regression

This section furthers the analysis presented in Section 2.4.1. Radiation incident on the heat-flux gauge also has a component that originates from the hot wall of the main chamber that encloses the gaseous domain. So:

$$q_{rad} = q_{gs} + q_{wall} \tag{2.8}$$

Where:

$$q_{wall} \propto T_w^4 \tag{2.9}$$

And using arguments similar to Equations (2.6) and (2.7):

$$q_{gs} \propto \varepsilon_{gs} \propto f_v \tag{2.10}$$

Finally, using constants of proportionality A and B:

$$q_{wall} = AT_w^4 \tag{2.11}$$

$$q_{gs} = Bf_v \tag{2.12}$$

$$q_{rad} = AT_w^4 + Bf_v \tag{2.13}$$

In Equation (2.13):

- 'A' contains information of intensity attenuation on the path towards the sensor, shape factor and wall emissivity.
- 'B' contains information of gas volume geometry, attenuation and flow.

A term to account for the gas-soot domain temperature is conspicuously absent in Equation (2.13). The explanation is as follows:

It was found that for very similar radial profiles of temperature (Figure 2.10(b)), the radiation heat-fluxes were different by as much as ~35% (circled values in Figure 2.10(a)). So, the radiative heat-flux was a much weaker function of the gas phase temperature as compared to wall temperature and soot volume-fraction; and as a result, could be neglected from the model. To some extent, this was also a lucky finding as accounting for the radial profile of temperature would have required the radial profile of the soot volume-fraction. Obtaining the latter was not possible as it would have required higher powered lasers which were not feasible due to safety considerations in the current setup.
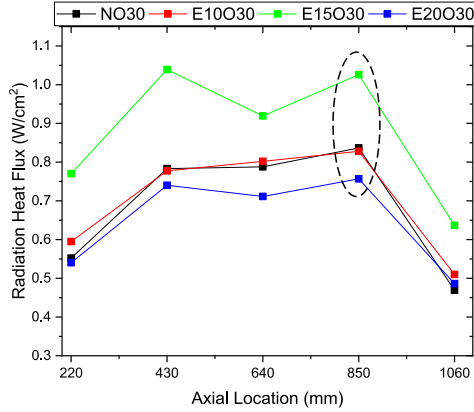
(a) Radiative heat-fluxes at port 4 (circled)   **(b) Gas temperature radial profile at port 4**
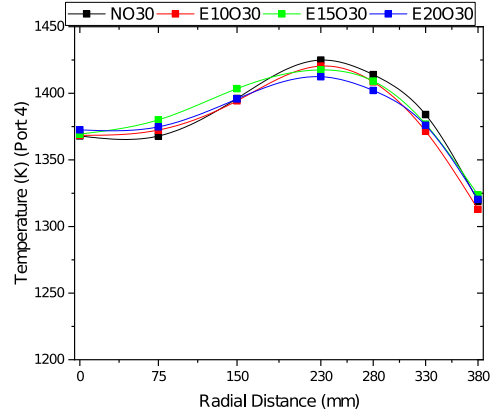
Figure 2.10: Explanation for exclusion of gas temperature from radiation model.

q_{rad}, f_v, and, T_w are experimentally determined and therefore, known quantities in Equation (2.13). Multi-variate regression analysis was performed to determine A and B (but by excluding E20O21 and E20O30 for reasons same as those mentioned in Section 2.4.1). A and B were found to be positive real numbers for all the ports. Negative values would have had unphysical implications by incorrectly suggesting that radiation reduced with increasing temperatures (for $A < 0$) or with increasing soot volume-fractions (for $B < 0$). Further, R^2 values for the multi variate regression were markedly better than those for the direct correlation (Figure 2.11).
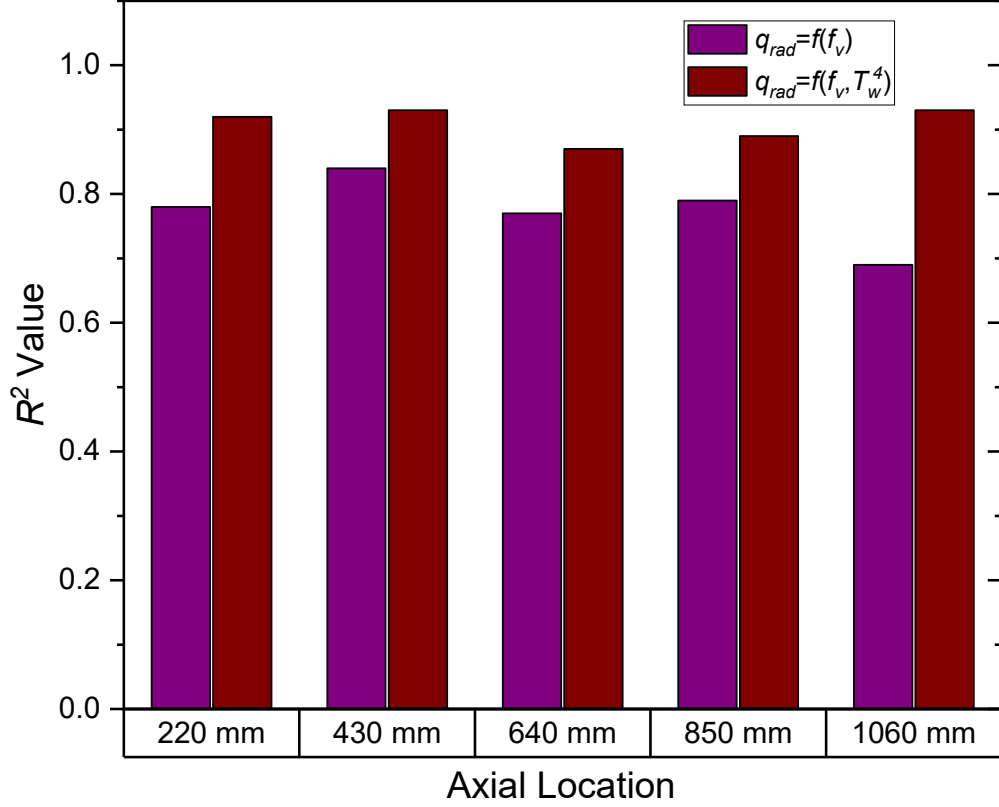
Figure 2.11: R^2 values for regression analyses.

In relative terms, better R^2 values for the multi variate regression suggest that more physics was successfully captured as compared to the direct correlation. In absolute terms, values around 90% suggest the satisfactory capture of most of the physics dictating the phenomenon. That is, even without accounting for gas temperatures, the analysis delivers quantitative confirmation of the conjectures made in Section 2.2.

By knowing B, a quantity q_{frac} was defined as the fraction of the net incident heat-flux which was emitted by the gas-soot phase.

$$q_{frac} = \frac{q_{gs}}{q_{rad}} \qquad (2.14)$$

where, q_{gs} is determined using Equation (2.12).

q_{frac} is plotted at different axial locations for different cases in Figure 2.12. It can be seen that this quantity is higher for cases with higher soot content; and this further buttresses the proof of the initial conjecture.
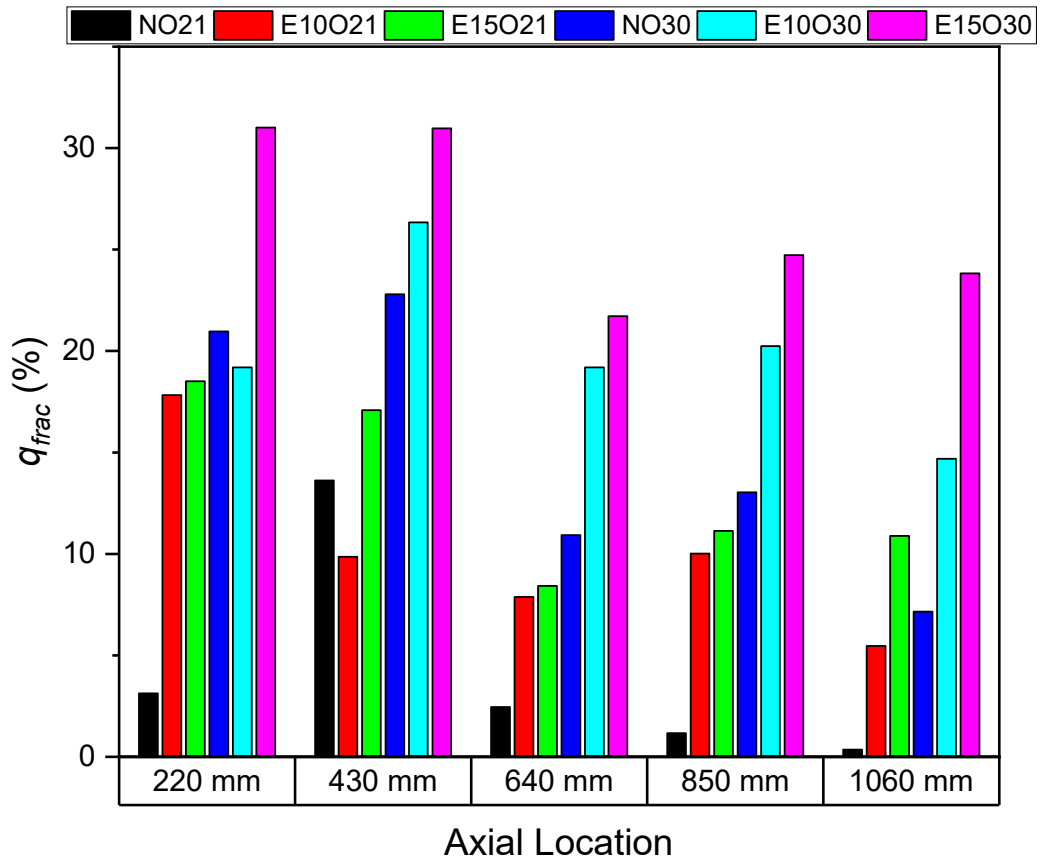
Figure 2.12: Fraction of net radiation emitted by gas-soot domain.

2.4.3   Specific NOx

A parameter to evaluate furnace performance was defined as NOx emissions per useful heat gained by the furnace (plotted in Figure 2.13). NOx emissions were measured in the exhaust in the "Preheat-Zone". Useful heat gained by the furnace was determined using the temperature difference of the inlet and outlet streams of water used to cool the "Water-Cooled Plate".
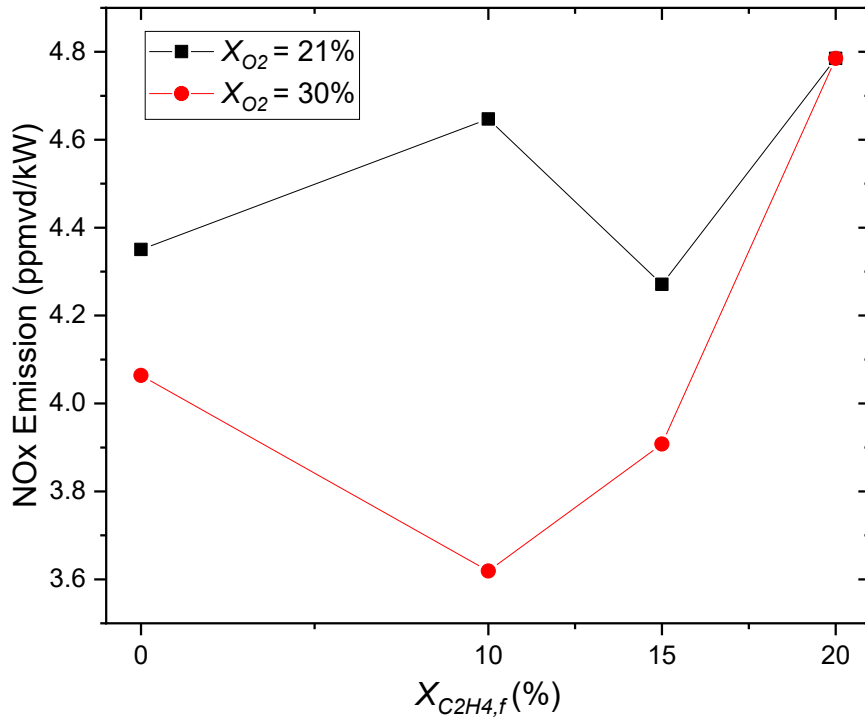
Figure 2.13: Specific NOx

Figure 2.13 is reflective of the two competing effects of ethylene blending on specific NOx, namely, enhancing performance with higher soot content and aggravating emissions due to a shift away from HC. By using enriched oxidizers, there is a gain of about 5% (X_{C2H4} = 0%) which grows to almost 25% for X_{C2H4} = 10%. Soot loading does not have any benefits for X_{O2} = 21% but a ~10% gain for X_{O2} = 30%. However, a blend ratio of 10 – 15% is seen to be an optimal value as beyond this, there is a reversal of all gains that were accrued due to:

- Shifting to HC mode.
- Shifting to oxygen enriched operation.
- Having higher soot content.

2.5   Concluding Remarks

Fuel blends with ethylene as an additive to natural gas were tested; with the conjecture that soot will enhance heat removal via radiation and inhibit the self-accelerating cycle which causes thermal runaway. Through the usage of physics based

24

regression models, soot was shown to enhance radiative heat-transfer. Further, it was observed that soot loading improved furnace performance and reduced emissions on a specific basis. Ethylene being an unsaturated hydrocarbon with higher reactivity tended to shift the mode of combustion away from the HC regime. While it did improve radiation, it simultaneously imposed a NOx penalty and thus, an optimal blend ratio was determined. The benefits outweighed the penalty for $X_{C2H4} \leq 15\%$; whereas beyond that, gains due to shift to HC regime, oxy-enriched operation, and soot loading were reversed.

Chapter 3:

The Effect of Flow on Homogeneous Combustion[5]

3.1   Introduction

Reiterating some of the discussion from Section 1.4, with the exception of a few [26,32], a majority of studies reporting oxy-fuel combustion in the HC regime do not use methane/natural gas as fuel. Biogas [33,34], propane [22], light oil [35], and most prominently, coal [35–38] have been investigated with different levels of oxidizer enrichment by researchers. As a sidebar - while coal has its own set of issues (ash deposits, fuel bound NOx, SOx etc), oxy-fuel HC with pulverized coal is a very practical and a realistic solution because:

- The reaction is constrained to the particle surface which reduces the global reaction rates (and thus, Da) for a given thermal input.
- Higher emissivity particles radiate heat away from the reaction zone better as compared to gaseous products of combustion.

Nonetheless, methane (natural gas) is the most industrially relevant fuel (especially in the US [1]) and is much less polluting than coal. Thus, further investigations are needed with industrial feasibility kept in mind.

Extremely high preheat of incoming reactants via specialized electric/gas-fired pre-heaters [67,68] is one of the most conventional ways to achieve HC; but it can be costly and fraught with safety issues at industrial scales. Indeed, enriching oxidizer streams is also costly (equipment, maintenance, and running) but can be a cheaper alternative for high temperature demands (in the US, electricity is ~3 times costlier than natural gas per kWh

[1]). Moreover, reduced exhaust flow rates (for oxygen enriched combustion) prolong the life of expensive catalytic converters (after treatment "scrubbers"). The recuperative furnace utilized in the present study uses waste heat from exhaust to achieve moderate preheat with a simple setup.

3.2   Literature Review

Sánchez et al. [26] reported very low NOx emissions with X_{O2} up to 40% for a 20 kW regenerative burner. The burner had a sophisticated "switching" mechanism in which the same set of nozzles operated alternatively to inject oxidizer and extract exhaust for 30 seconds each. Such an arrangement coupled with the cordierite honeycomb regenerators can be challenging for industrial settings due to cost and maintenance downtime concerns. Moreover, the heat load was imposed via cooling pipes running through the furnace chamber. This is more like a boiler and unlike industrial furnaces where the load is kept at one end of the furnace (generally acting as one of the "boundary walls" for the gaseous chamber). A similar heat extraction strategy was employed by Li et al. [32] who utilized external dilution of the reactants with CO_2 for a 13 kW burner; and in some test cases completely replaced N_2 in the oxidizer with CO_2. External dilution is an excellent way to reduce Da and achieve HC [15,32,69] as increased inlet jet momenta aid mixing and reduced reactant concentrations reduce reactivity. CO_2 is a better diluent than N_2 as it:

- has a higher specific heat
- lowers N_2 content available for NOx formation
- radiates away heat and cools the reaction zone
- promotes NO reduction [70].

The furnace used by Li et al. [32] was pressurized to avoid air ingress. This is also unlike industrial combustors which are operated at a pressure slightly lower than atmospheric due to safety considerations. Air ingress is a source of NOx emissions even if the inlet streams have no nitrogen content; as was observed by Krishnamurthy et al. (2–3 ppm NOx with pure propane and oxygen) [22]. Commercially available natural gas generally has an appreciable nitrogen content. As listed by Wünning et al. [71], pure

reactant streams (no nitrogen content), and perfect sealing (to avoid air ingress) are hard and costly to implement in practical systems. Furthermore, practical implementation of external recirculation of high temperature exhaust gas or displacing N_2 with CO_2 in the reactant streams at industrial scales is also difficult and costly. Relevant to practice, it must be emphasized that this study reports on a 91.7 kW furnace which would be easier to scale up as compared to the ones reported in [26,32].

Based on the discussion above, it can be seen that there is a need to study/develop oxy-fuel HC systems which are industrially feasible. The furnace used for this work:

- has the heat sink as the bottom wall of the furnace.
- operates at a pressure slightly lower than atmospheric.
- operates without any external preheat/dilution of reactants.

Also, since such systems would be expected to work with fuels and oxidizers having considerable nitrogen content, flows in these combustors would need proper engineering to ensure suppression of NOx forming and promotion of NOx reburning reactions. Consequently, understanding the flow in the reaction zone is important.

Flows in HC combustors are highly complex, turbulent, and driven by high-momentum inlet jets. Due to the SJWJ configuration (explained in Section 3.3.1), fuel-jets generally have low momentum. So, there is an opportunity to improve homogeneity by increasing the fuel jet momentum. This study is rooted in the conclusions presented by Li et al. [32] and Dally et al. [6] who found that externally premixing the fuel with an inert gas helped achieve MILD conditions. The effect of increasing fuel-jet momentum in enhancing internal dilution and thus potentially reducing NOx emissions is tested here. There appears to be a lack of reports on the effect of fuel-jet momentum on HC. There have been studies on the effect of oxidizer jet momentum [7,72], premixed jet momentum [67,73] and diluted fuel jet momentum (with CO_2, N_2) [32,68]. This appears to be a settled issue with the conclusion being that higher momenta of the jets cause greater entrainment and dilution of reactant streams, thus reducing NOx emissions. However, limited information is available about "pure" (as available commercially; < 5% inert content) fuel-jets.

In this work, attempts have been made to understand and explain the complex flow (mentioned above) by breaking it down into a set of canonical flows which are well understood. Parameters like momentum ratio and scaled distances are found to be representative of macro flow features and they have been used for analysis. Fuel jet momentum is varied by changing only the inlet nozzle diameter and not by including any inert content to increase the mass flow rate. The major part of this study is carried out numerically with the support of some experiments. This is done to gain a deeper insight into the complex 3-D flow in a furnace with limited optical access. To outline, the objectives of this study are to explore:

- HC with enriched oxidizers for industrial use.
- Complex flows in a parallel jet furnace.
- The effect of fuel jet momentum on emissions.

3.3   Numerical Model

3.3.1   Geometry

The details of furnace geometry are described in Chapters 1 and 2 and elsewhere in literature [74,75] and presented only briefly here. The furnace has a parallel jet configuration with four oxidizer jets arranged in a circle of radius $17.5d_o$ around the centrally located fuel jet. Reactants are injected vertically downwards into the main chamber where combustion and heat release take place. Then the products travel radially outward through the exhaust ports and upwards through the annular exhaust vent. The hot gases exchange heat with the incoming reactants via metallic pipes[6] in the preheat zone before leaving the furnace. Fresh reactants enter the main chamber with only a moderate degree of preheat and therefore the test cases cannot be categorized as being in the HiTAC mode of combustion [76,77]. Meanwhile, a water-cooled bottom plate simulates a thermal load which is typical of industrial furnaces.

Using the framework laid down by Arghode et al. [78,79], the furnace can be said to have a "forward-flow" design despite the conclusion of the "reverse-flow" design being

---

[6] Only one shown in Figure 3.1; four others not shown for clarity.

better in minimizing emissions. This is to enable heat sink positioning similar to industrial furnaces (as discussed in Section 3.2). Nonetheless, the overall flow structure has elements of the reverse-flow design; and these elements play a central role in determining the level of NOx emissions (detailed in Sections 3.4.1 and 3.4.2). A relatively strong fuel jet is utilized to have a high net momentum injection into the reaction chamber. The reasonably large jet separation distance ($17.5d_o$) helps to explicitly study the effect of internal dilution of the fuel jet. Also, the spread-out oxidizer jets ensure availability of high flow momentum throughout the furnace. Other similar works featuring fully non-premixed reactant streams deal with weak fuel jets which get entrained into strong oxidizer jets fairly upstream in the direction of flow (jet-separation distances $<10d$ [10,28,67,68,72,73,80]). Termed as Strong-Jet/Weak-Jet (SJWJ) [81] configuration, it comes about naturally due to the stoichiometric needs of combustion where the mass flow rate of fuel (m_f) is generally an order of magnitude lower than the oxidizer (m_o).

For the numerical model, geometric symmetry is utilized to reduce the size of computational domain to only a quarter of the main chamber (Figure 3.1 and Figure 3.3). It is expected (and confirmed via gas species measurements) that the reactions are completed in the main chamber. This raises the possibility of exclusion of Annular Exhaust Vent and Preheat Zone from the domain to be simulated; but it requires further justification which is presented later in this section.
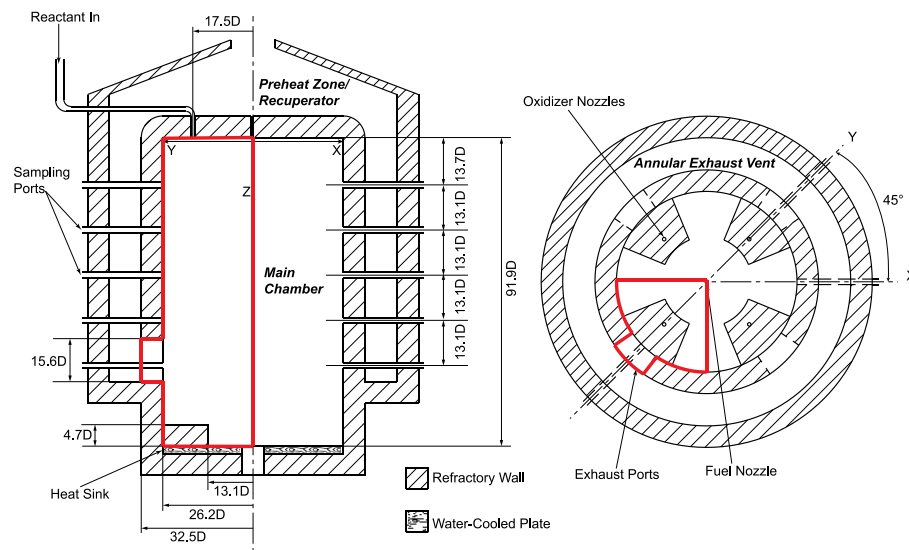
Figure 3.1: Portion of the furnace marked in red is simulated.

30

The heat exchange (between incoming fresh reactants and outgoing exhaust) in the preheat zone (Figure 3.2) is described using basic analytical relations for heat exchangers. A "User Defined Function (UDF)" (Appendix) code is written to dynamically determine the inlet temperatures of the fuel and oxidizer streams (mass flow inlets in Figure 3.3) per iteration as functions of the exhaust gas temperature (outflow in Figure 3.3). So, the annular exhaust vent and the preheat zone are excluded from the domain to be simulated. These measures help reduce the computational costs considerably.
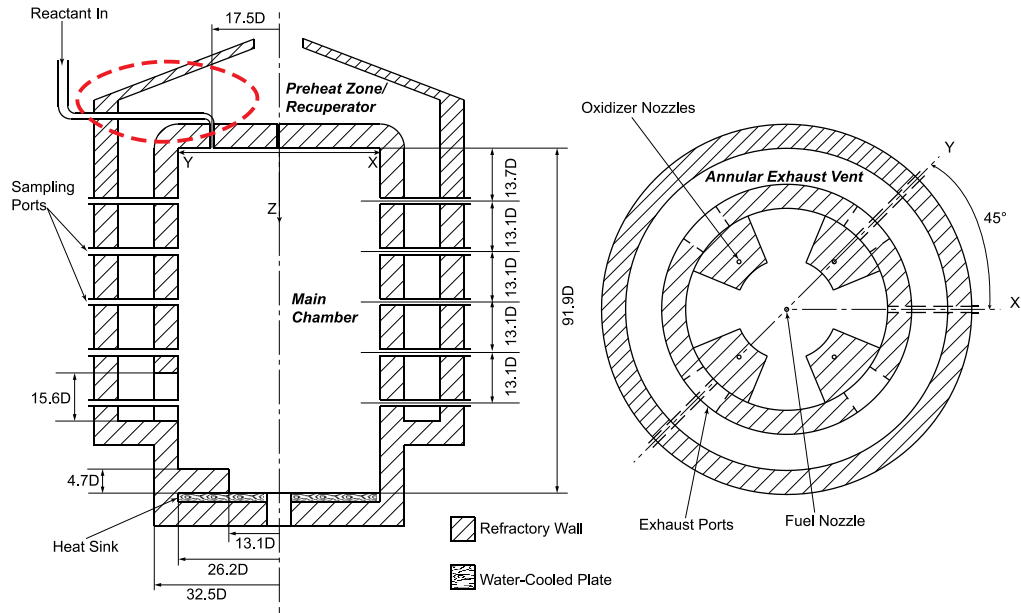
Figure 3.2: Heat transfer in the portion marked in red was described using analytical equations.
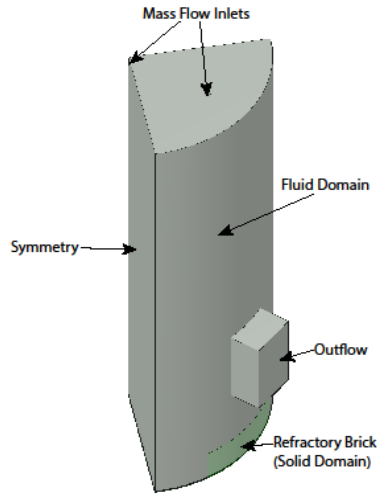
Figure 3.3: Simulated domain.

31

After a thorough grid independence study, a mesh with approximately 2.1 million elements (all hexahedral) is chosen. The average cell size is $\sim 3 \times 3 \times 3$ mm. Appropriate mesh refinement is performed in regions with expected high gradients and in the near-wall regions.

3.3.2   *Mathematical modeling*

ANSYS FLUENT is used for simulating the operation of the furnace under conditions listed in Table 3.1. Models used for the simulations are as follows:

- Turbulence: RANS, Standard k-ε, Enhanced Wall Function [82,83]
- Radiation: Discrete Ordinates, WSGGM [84,85]
- Chemical Mechanism: GRI Mech 3.0 [66]

Employing RANS allows the usage of symmetry boundary conditions. Radiation-energy coupling is turned off as it is mainly important for optically thick systems whereas, cases simulated here are expected to be optically thin. Turning it on would just have made the computation expensive while making little difference to the resulting thermo-chemical field. Radiation heat exchange with the walls is included in the model. Second-order discretization is used for all quantities and the SIMPLE algorithm is utilized to treat pressure–velocity coupling.

A coefficient for k-ε was modified ($C_{1\varepsilon} = 1.60$) as per Pope [86] because of the jets being round. Turbulence-Chemistry Interaction (TCI) was modeled using the Eddy-Dissipation Concept (EDC) model [87] with In-Situ Adaptive Tabulation (ISAT) [88]. EDC assumes that reactions occur in small turbulent structures (called the fine scales) over a finite interval of time. These fine scales and time intervals are modeled and used to calculate the source term in the species' conservation equations. While EDC was initially developed for conventional combustion, it has been shown to perform well for HC also [22,32] and validated for this study (Section 3.3.5). Modification of EDC coefficients (C_{ξ} and C_{τ}) as per Evans et al. [89] and De et al. [90] yielded erroneous thermal fields and hence, the usual values were used ($C_{\xi} = 2.1377$ and $C_{\tau} = 0.4083$). The authors believe that this is because these coefficients were optimized by Evans et al. [89] and De et al. [90] for combustion in highly diluted environments while that is not the case here. For other

parameters, the models available with the solver are utilized. Mathematical formulation, applicability, merits, demerits, and limitations of these models have been discussed in great detail in literature and therefore not discussed here in the interest of brevity.

3.3.3 Parameter Space and boundary conditions

Parameters kept constant for all cases are: mass flow rate of fuel (equivalent to 91.7 kW chemical heat input in the non-reduced domain), diameter of the oxidizer nozzle (d_o = 16 mm), and fuel-jet composition ($X_{CH4,f}$ = 95% and $X_{N2,f}$ = 5%). Parameters varied were equivalence ratio (ϕ), diameter of the fuel nozzle (d_f), and oxygen content in the oxidizer stream (X_{O2} as listed in Table 3.1 and the remnant is N_2). Steady-state simulations are performed for eighteen cases (Table 3.1). To facilitate easier discussion, cases have been henceforth referred to as X_Y_Z where X is d_f in mm, Y is one among "Rich", "Stoich", and "Lean" (standing for ϕ = 1.1, 1.0, and 0.9 respectively), and Z is X_{O2} in percent. Across cases, Reynolds number of the fuel jet varies due to different jet diameters while for the oxidizer jet, it varies due to varying mass flow rates. There are also minor variations due to varying temperature (see Section 3.3.1).

Only near-stoichiometric conditions have been explored due to industrial economic concerns. Lean and rich conditions are undesirable due to the costs associated with unburned enriched oxidizer and natural gas respectively. In addition, since the purpose is to attain high temperatures, any significant deviation from stoichiometric conditions is unwarranted.

Table 3.1: Details of computational cases. Quantities in the last three columns are found post-simulation.

Case	d_f (mm)	ϕ	X_{O2}	Re_f	Re_o	M_r[7]
10_Rich_30	10	1.1	30	9600	10100	6.41
10_Stoich_30	10	1	30	9900	11500	7.54
10_Lean_30	10	0.9	30	9900	13200	9.05
10_Rich_21	10	1.1	21	10200	16100	11.62
10_Stoich_21	10	1	21	10100	18200	13.63
10_Lean_21	10	0.9	21	10100	20600	16.35

---

[7] Defined as the ratio of oxidizer jet momentum to fuel jet momentum (J_o/J_f).

13_Rich_30	13	1.1	30	7400	10100	10.83
13_Stoich_30	13	1	30	7700	11500	12.74
13_Lean_30	13	0.9	30	7700	13200	15.29
13_Rich_21	13	1.1	21	7900	16100	19.64
13_Stoich_21	13	1	21	7800	18200	23.05
13_Lean_21	13	0.9	21	7800	20600	27.65
16_Rich_30	16	1.1	30	6200	10200	16.41
16_Stoich_30	16	1	30	6200	11500	19.30
16_Lean_30	16	0.9	30	6200	13200	23.17
16_Rich_21	16	1.1	21	6200	16100	29.74
16_Stoich_21	16	1	21	6400	18200	34.91
16_Lean_21	16	0.9	21	6400	20600	41.89

Boundary conditions are imposed based on the particular parameter set (Table 3.1) to be tested. The values are as follows:

- Mass flow rate of fuel; m_f = 0.0004583 kg/s (equivalent to 91.7 kW chemical heat input in the non-reduced domain)
- Fuel jet composition: see page 33
- Oxidizer jet composition: see page 33
- Mass flow rate of oxidizer; m_o: Calculated based on ϕ and X_{O2} of a particular case for the fixed m_f
- Wall temperature; T_w: Data taken from experiments
- Heat sink; Convective heat removal rate h = 424 W/m^{2}K; value taken from Shin [74] and Lee [75].

3.3.4 Steps in performing the simulation/computation

The simulations were performed in four steps with increasing degrees of refinement. These steps and the number of iterations in each step are described below:

- Step 1: An initial thermal field is obtained using a skeletal/global chemical mechanism, namely, Westbrook-Dryer 2-step mechanism [91] with one

radiation iteration every ten flow, energy, and chemistry iterations. (3000 iterations)

- Step 2: A crude solution is obtained using the detailed chemistry mechanism, GRI Mech 3.0, with a relatively high ISAT error tolerance of $\varepsilon_{tol} = 10^{-3}$. (4000 iterations)

- Step 3: The solution is refined with a finer ISAT error tolerance (discussed in Section 3.3.5) of $\varepsilon_{tol} = 10^{-4}$. (8000 iterations)

- Step 4: The solution is run with one radiation iteration every one flow, energy, and chemistry iteration until the solution is stable and converged. (~6000 – 10000 iterations).

The simulations were performed on a 24 core system with the University of Michigan FLUX computing cluster and the total walltime[8] taken for the simulations was ~25 days.

3.3.5 Model validation

To validate the numerical model, comparisons have been made against experimental data for 16_Rich_21 at 35 points in the Y-plane within the furnace (Figure 3.4). Temperatures are measured using a fine wire thermocouple and corrected for radiation. Gas analysis is performed for CO_2 (infrared two-beam alternating light method), O_2 (paramagnetic effect by the alternating pressure method), and NO (chemiluminescence due to reaction with ozone).

Numerical and experimental data are found to be in decent agreement with minor deviations (especially considering diffusivity introduced in the data due to gas sampling via suction). Relatively larger deviations in the thermal field are seen in the radially outermost regions. However, considering the fact that no such deviations are seen in any of the species' fields (which have close interdependence with the thermal field; NOx being particularly sensitive to temperature), it was concluded that the experimental data for temperature in these regions may not be entirely accurate; possibly due to uncertainties in the parameters used for radiation correction. Another expected source of errors is the inexact radial positioning of the sampling probes due to manual operation.

---

[8] Physical time taken for a computation to be performed.

A test was also performed to determine the optimal ISAT error tolerance. A smaller error tolerance entails a more accurate solution but also comes with a penalty of increased walltime. For the test-case, reducing the error tolerance from 10^{-4} to 10^{-5} caused an increase of computational time by a factor of ~3. It can be seen from Figure 3.2 that an order of magnitude decrease in ε_{tol} beyond 10^{-4} causes minimal influence on the species' and thermal fields. Thus, $\varepsilon_{tol} = 10^{-4}$ is the smallest value used for the computations (Section 3.3.4).

(a) CO₂-distribution

(b) O₂-distribution

(c) NOx-distribution **(d) Temperature field**
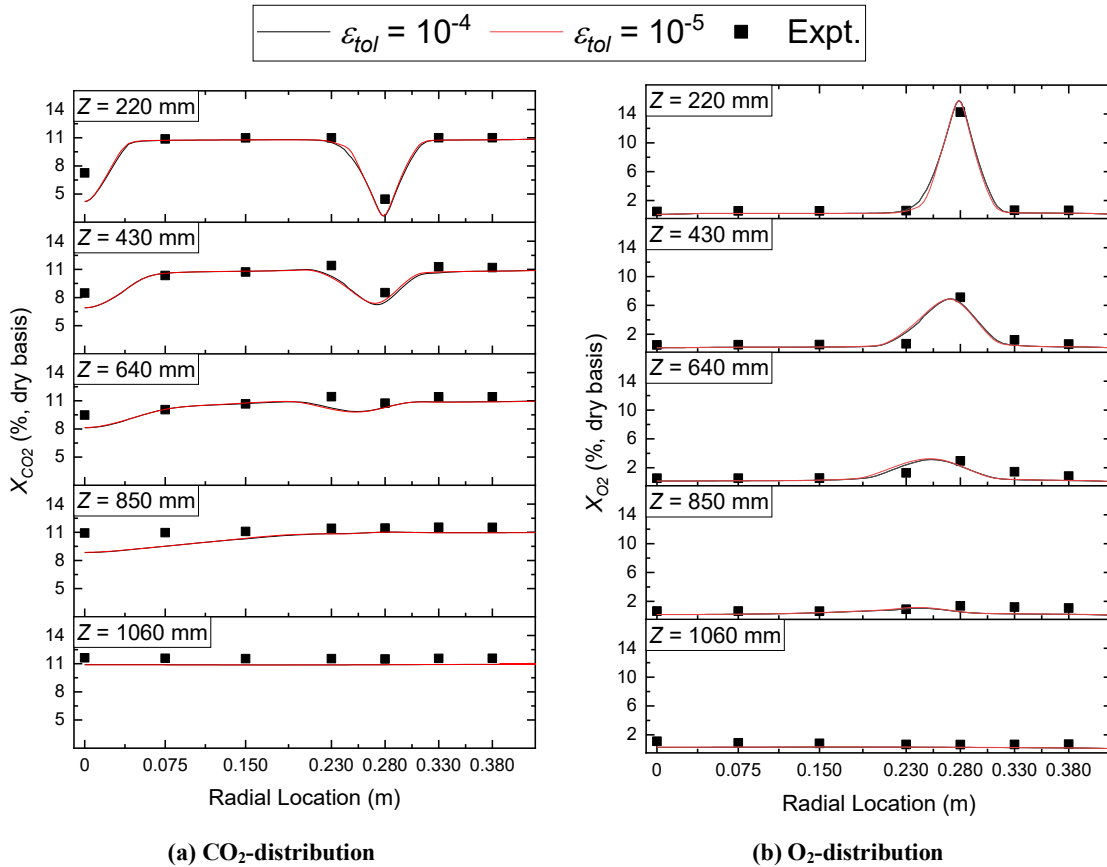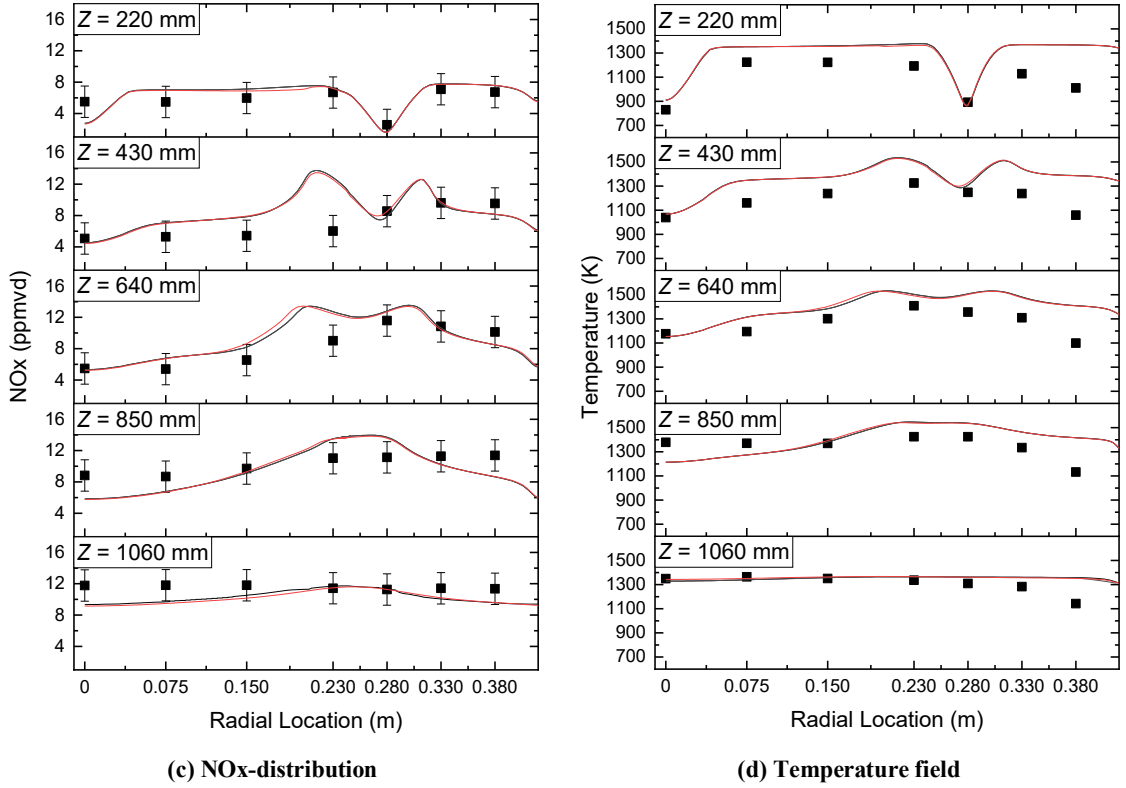
Figure 3.4: Validation of the model. For symbols with no error bounds shown, the error is of the order of the size of the symbol.

3.4 Results and Discussion

3.4.1 Flow

The test cases are expected to have similar levels of turbulence and hence the effect of turbulence on chemistry is not discussed in detail. Moreover, since the focus was to understand the performance of a fairly large furnace, RANS has been employed and fine scales have not been resolved with a precision which can provide for informed discussion on the matter.

Recirculation rate (K_v) is frequently used to asses HC [5,71] and is therefore the first parameter studied here. A higher K_v represents more entrainment of burnt gases and hence more dilution of the fresh reactants. For a cross sectional area, A, in a flow field where the reactant nozzles issue in the negative-y direction:

$$K_v = \frac{m_r - (m_f + m_o)}{m_f + m_o} \tag{3.1}$$

37

where,

$$m_r = \int_A \rho v_y dA \mid v_y < 0 \qquad (3.2)$$

Figure 3.5 presents three cases with exactly the same $(m_f + m_o)$ values. It is verified that a smaller fuel nozzle improves recirculation rates and therefore, entrainment driven dilution. However, due to the low fuel mass flow rates, the improvement is not as significant as it is with a similar decrease in size of oxidizer nozzles [5].
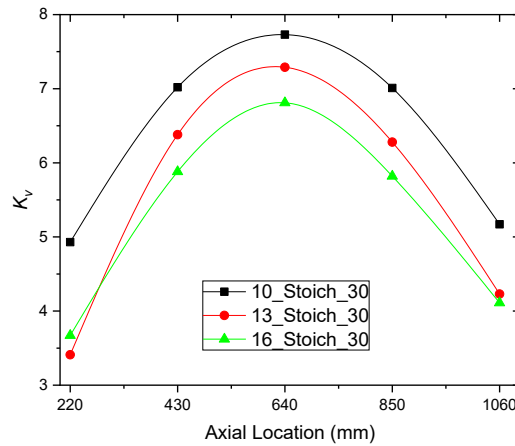
Figure 3.5: Recirculation rate improvement with a smaller fuel nozzle.

The flow fields for all the cases are qualitatively similar (Figure 3.6 and Figure 3.12). The oxidizer jet shows a slight (radially) inward bend which can be attributed to:

- strong recirculation between the oxidizer jet and the wall (shown in Figure 3.12).
- the stepped refractory brick lining sitting on the water-cooled plate.

The oxidizer jet impinges on the refractory brick (for all the cases tested here) before turning radially inwards and upwards to meet the fuel-jet head-on; thereby creating a recirculation zone just above the water-cooled plate. This structure is very similar to the case of counter-flowing jets and there exists a "stagnation point" directly underneath the fuel jet where the vertical component of velocity becomes zero (components orthogonal to it are zero by definition due to symmetry boundary conditions).

38
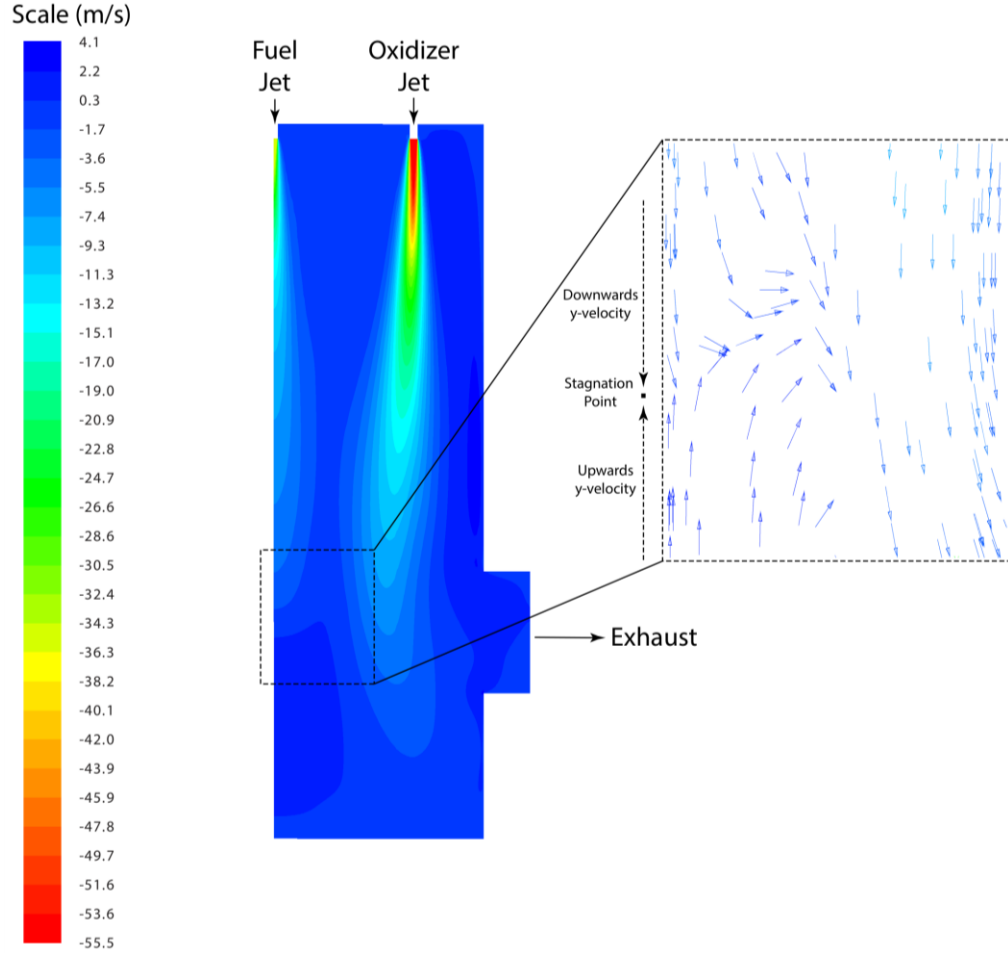
Figure 3.6: Vertical component of velocity (16_Rich_30) on a plane containing fuel and oxidizer jet axes (Y-plane). Velocity vectors shown in inset.

Stagnation length (l_{stag}) is defined as the vertical distance from the fuel nozzle exit to the stagnation point. Momentum Ratio is defined as the ratio of the oxidizer and fuel jet momenta at respective nozzle exits (Equation (3.3)).

$$M_r = \frac{J_o}{J_f} \tag{3.3}$$

The distance of the bottom wall from the nozzle exit is 1.44 m. 10_Rich_30, 10_Stoich_30, and 10_Lean_30 have the lowest M_r's and for them, the fuel jet impinges on the bottom plate. Thus, the stagnation length for them is 1.44 m. l_{stag} is plotted against M_r and a power-law curve ($y = a(x - b)^c$) is fit through the data (excluding cases with fuel jet impingement). The power-law based fit was chosen as with a non-zero J_f, l_{stag} can only asymptotically

approach zero for $M_r \to \infty$. The fit (Equation (3.4)) yielded a correlation with $R^2 = 0.98$ (Figure 3.7).

$$l_{stag} = 1.63(M_r - 7.65)^{-0.20} \tag{3.4}$$

The slight deviations from the fit curve can be explained by irregularities in flow caused by the stepped brick. The behavior is expected to be tighter with a fully flat bottom surface. This correlation predicts $M_r = 9.51$ for the onset of impingement; which is a reasonable value as the cases with impingement have M_r lower than this.
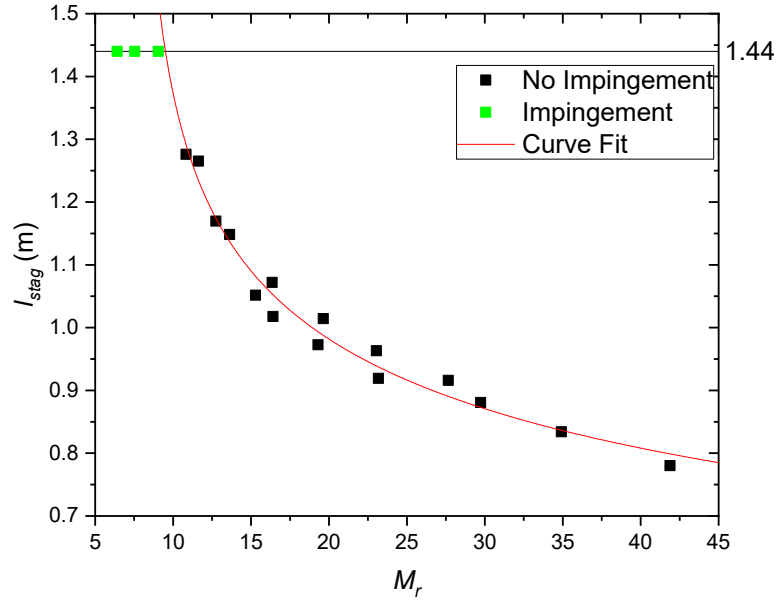
Figure 3.7: Stagnation length as function of momentum ratio. Nozzle exit-bottom wall distance is 1.44 m which is the maximum possible l_{stag}. (Green symbols represent cases with impingement i.e. $l_{stag} = 1.44$ m).

Nozzle diameter is one of the most usual (length) scaling parameters in flows but in setups with multiple (different sized) nozzles dictating the flow, a single diameter would not work. l_{stag} can be a better scaling parameter because it accounts for both the nozzles via its M_r functionality. Jet-center velocities (U_c) scaled by the velocities at nozzle exit (U_f, U_o) are plotted against downstream distance (Z) normalized by l_{stag} in Figure 3.8(a) and (b). Also depicted, are comparisons of the fuel and oxidizer jets with the canonical free jet [92] in Figure 3.8(c) and (d). For clarity, only a few cases (including either M_r extremity) are depicted in Figure 3.8(a) and (b) while only both the M_r extremities are presented in Figure 3.8(c) and (d).

(a) Velocity under fuel jet

(b) Velocity under oxidizer jet

(c) Fuel jets compared to free jet [92]

(b) Oxidizer jets compared to free jet [92]
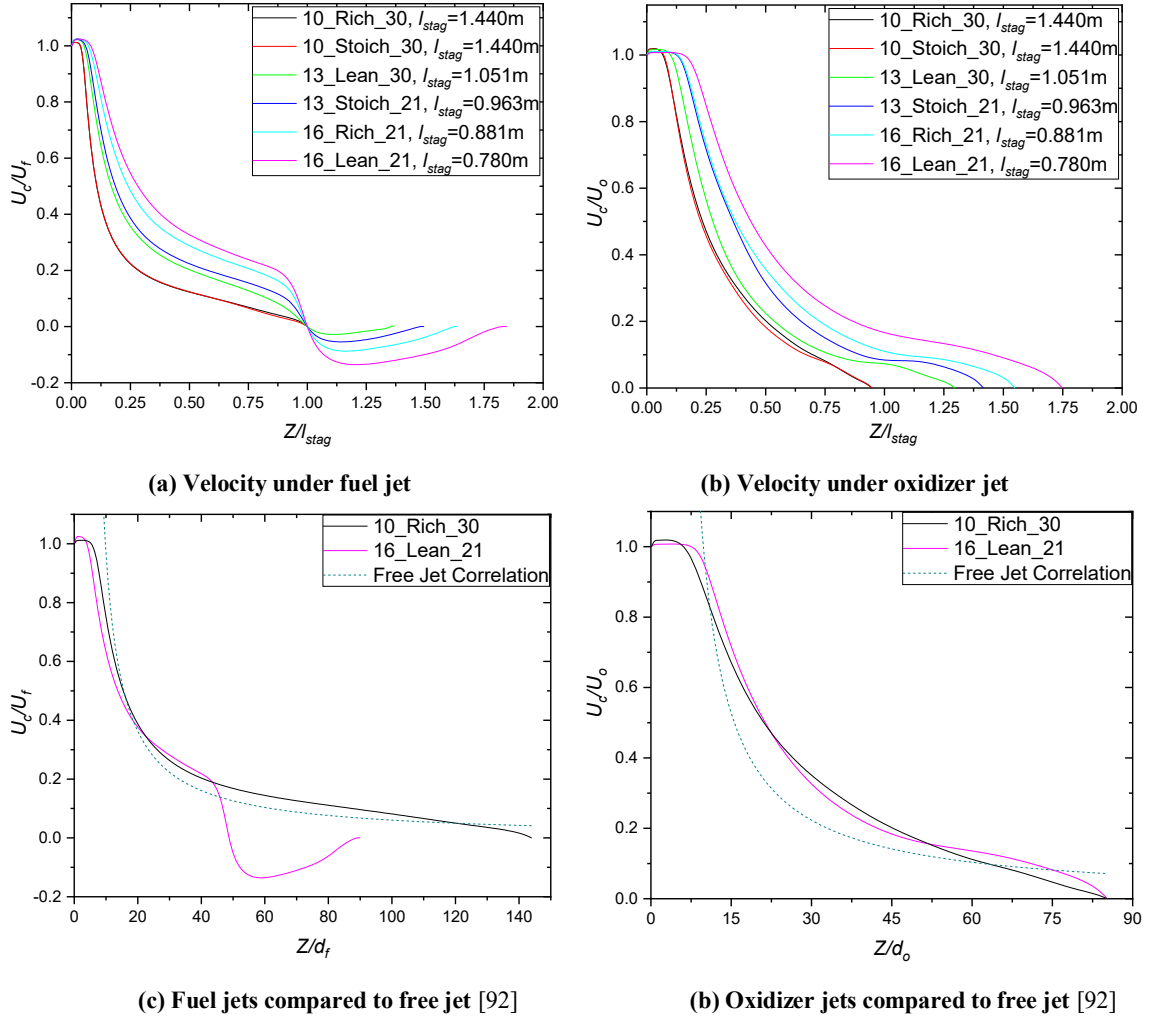
Figure 3.8: Scaled velocity plots of reactant jets.

From Figure 3.7(a), it is observed that some fuel-jet velocity plots resemble the canonical case of a free jet while others resemble the canonical case of counter-flowing jets; with a gradual transition from the former to the latter based on decreasing l_{stag} or (increasing M_r). And all oxidizer jets resemble the canonical case of a free jet.

Further analysis from Figure 3.8(c) and (d) reveals that all jets behave like a free jet in the upstream portion ($< 40d_f$). Whereas, the behavior in the downstream portion is dictated by the relative strength (M_r) of the jet.

- Low M_r or "strong" jets continue on behaving like a free jet with little effect of confinement and of the presence of other jets. This profile is also seen with other parameters (Figure 3.9).

41

- High M_r or "weak" jets show a substantial divergence from the free jet profile due to confinement and other jets. Like counter-flowing jets, there is also a sharp gradient near the stagnation point i.e. $Z/l_{stag} = 1$. Just like strong jets, this profile is also seen for other parameters (Figure 3.10).
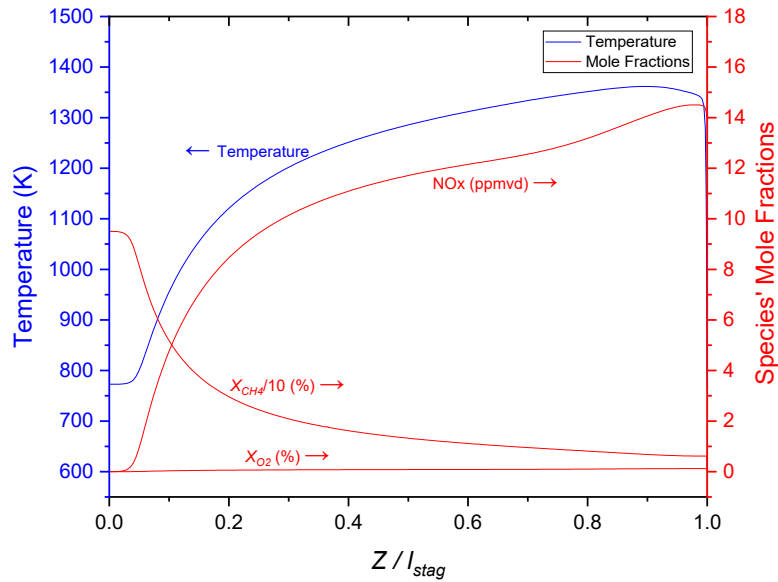
Figure 3.9: Parameters under fuel jet resemble profiles of free jets for 10_Rich_30 (low M_r of 6.41).
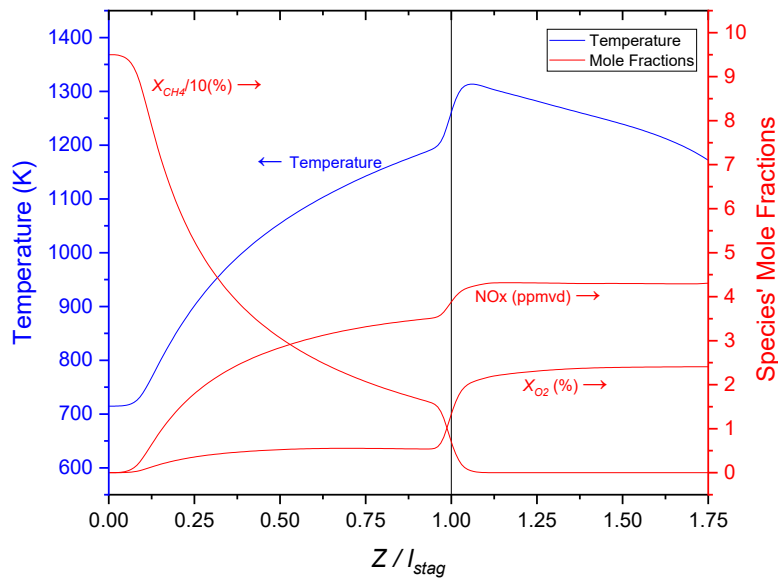
Figure 3.10: Parameters under fuel jet resemble profiles of counter-flow jets for 16_Lean_21 (high M_r of 41.89).

The jets can therefore be categorized as:

- Strong: Some fuel jets and all oxidizer jets.

42

- Weak: Some fuel jets.

In summary, the velocity-curves are functions of l_{stag} (and hence of M_r) and do not appear to be dependent on chemistry. To affirm the argument, some additional simulations were performed (Table 3.2). Using Equation (3.4), l_{stag} is predicted for these cases and compared to values obtained from numerical simulations. Cases 1 and 2 establish the weak influence of chemistry and buoyant forces respectively in determining the flow field; which is largely controlled by inertial forces (M_r).

Table 3.2: Generality l_{stag} – M_r of correlation.

Case	Details	M_r	l_{stag} actual (m)	l_{stag} predicted (m)	Error (%)
1	GRI Mech 2.11 [93] instead of GRI Mech 3.0.	19.64	1.015	0.988	2.7
2	Air at NTP flowing through both nozzles.	36.33	0.882	0.828	6.1

Finally, a set of simulations was performed on a shorter furnace (height = 1.2 m) and a similar l_{stag} – M_r correlation was observed (results not discussed here). These plots together constitute a set of powerful tools which can be used to predict macro flow structures in confined reacting/non-reacting turbulent jets just by knowing the conditions at the inlet (mass flow rate, density, and diameter of the jet). Undoubtedly, such predictions (numerical coefficients in Equation (3.4)) will vary for setups with a different number of nozzles or having differing geometries (number of jets, jet arrangement, jet-separation, bottom wall distance etc.).

3.4.2 NOx emissions

For this study "NOx" refers to NO and NO_2 but the former is seen to constitute >99% of NOx for all cases. To understand and explain NOx formation within the furnace, more discussion on the flow field is necessary. HC is established via intense dilution of incoming fresh reactant jets and hence the understanding of the dynamics of dilution is

important. In the parallel jet configuration studied here, two processes foster jet decay and dilution:

- Entrainment (for strong and weak jets).
- Counter-flow due to a recirculated "jet" (for weak jets).

The recirculated jet is composed of hot products of combustion being driven by the oxidizer jets and the 3-D flow occurring outside the plane containing the jets. The two aforementioned processes are found to be mutually competing for fuel jets i.e. a stronger fuel jet enhances the former but diminishes the latter and vice versa. The jet core is the slowest to get diluted for any jet. Figure 3.11 presents the lowest X_{CH4} along the fuel jet centerline for various M_r's. For any given inlet chemical composition (ϕ, X_{O2}), the weakest fuel jets are the fastest to fully decay (in terms of penetration length into the furnace), which indicates the importance of counter-flow driven dilution.
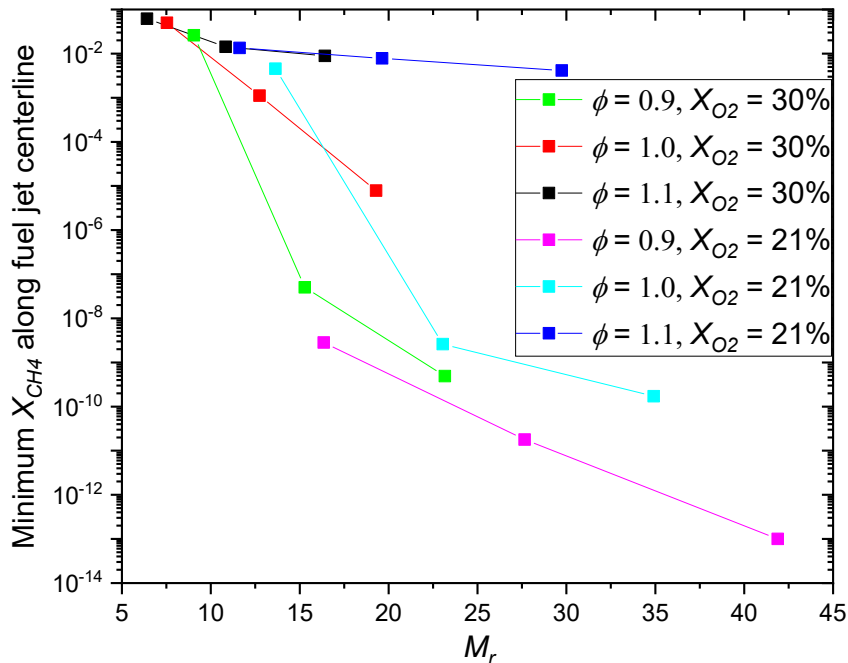
Figure 3.11: Minimum methane concentration along fuel-jet center-line (throughout the length of the furnace). The three highest M_r's correspond to cases with impingement.

As can be seen in Figure 3.6 and Figure 3.12, upon meeting the recirculated flow, the fuel jet turns radially outward and encounters the spreading oxidizer jet. This region, close to the horizontal plane containing the stagnation point, is anticipated to have the most intense chemical reactions and subsequently, the highest temperatures.

44
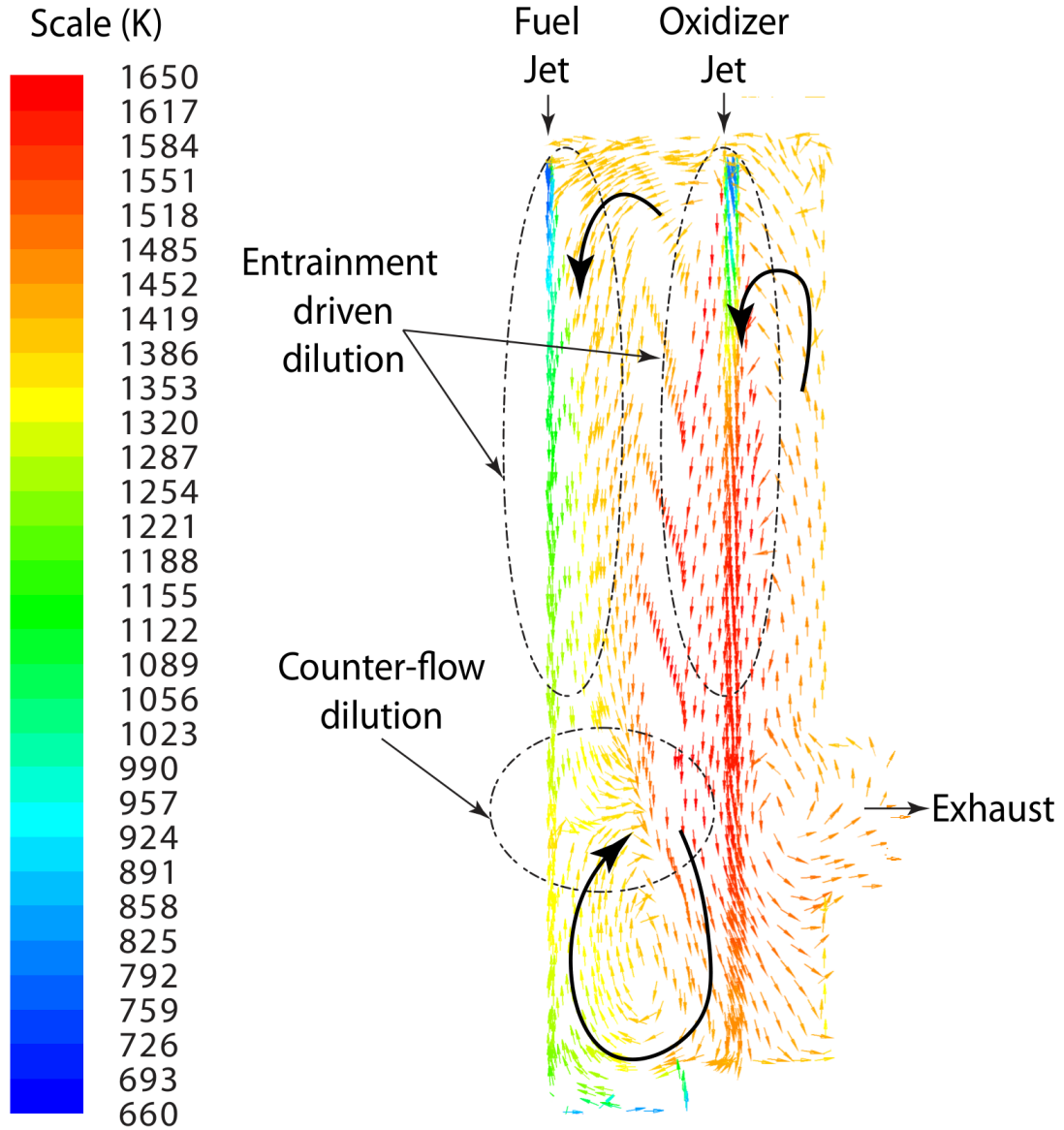
Figure 3.12: Velocity vectors colored by temperature (16_Rich_30) (vector lengths not to scale).

This expectation of high temperatures in the region is verified by defining a parameter, ΔT_{max} (Equation (3.5)) and plotting it against M_r (Figure 3.13).

$$\Delta T_{max} = \frac{T_{max,vol} - T_{max,stag}}{T_{max,vol}} \tag{3.5}$$

Where:

- $T_{max,vol}$ is the maximum temperature in the volumetric domain (K).
- $T_{max,stag}$ is the maximum temperature in the stagnation plane (K).

45

Except for the three cases with impingement (where stagnation plane is coincident with the water-cooled plate), ΔT_{max} is within 5% for all the cases; and close to 0% for a majority of the cases.

Consequently, axial positioning of this region (l_{stag}) is important with regards to NOx formation. It must be pointed out that the flow near the stagnation point and in the recirculated jet is highly three-dimensional in nature; but a discussion limited to the plane shown in Figure 3.6 and Figure 3.12 is sufficient to explain NOx emissions (elaborated below).
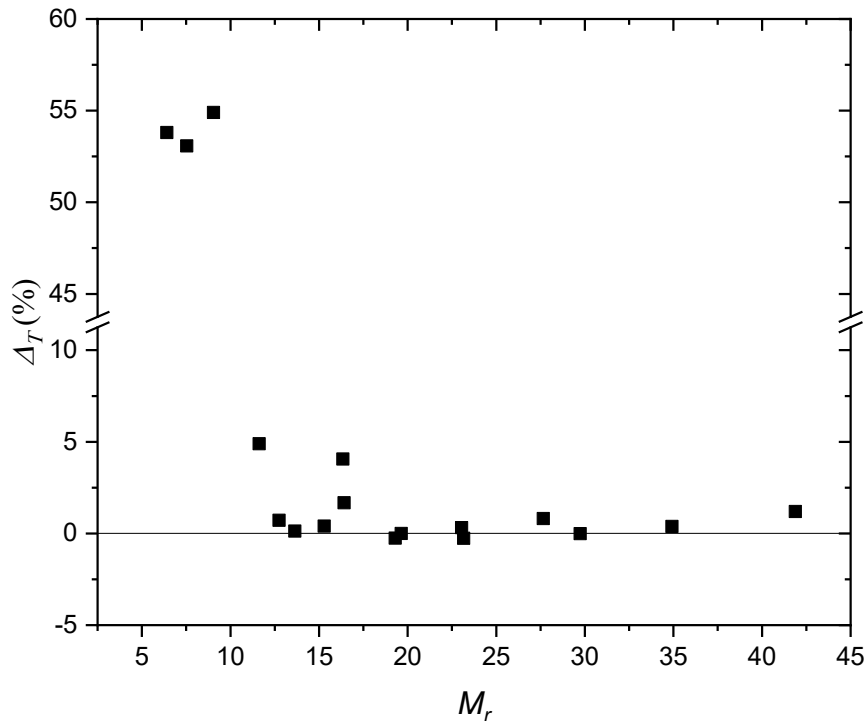
Figure 3.13: Maximum temperatures occur in the stagnation plane.

For any given inlet chemical composition, inlet temperature of reactants (T_{in}[9]) is seen to have limited to no bearing on the NOx emissions (Figure 3.14); and hence, only briefly discussed.

Higher inlet temperatures (with/without external preheat) are one of the most established ways to achieve HC [76,77] which led to the coinage of the term "High

---

[9] Defined as the mass-weighted average temperature (K) of the two inlet streams and calculated as described in Section 3.3.1.

Temperature Air Combustion (HiTAC)". The cases tested here have only moderately preheated incoming reactants and do not satisfy the temperature criteria for HiTAC [76,77] or for MILD as listed by Cavaliere et al. [5]:

- $T_{in} > T_{auto}$

- $(T_{max} - T_{in}) < T_{auto}$

where T_{max} is the maximum temperature in the domain and T_{auto} is autoignition temperature for the reactant mixture.

Non-adherence to criteria for MILD and HiTAC is the reason behind the $NO_x - T_{in}$ functionality being different from what is conventionally known for HiTAC and MILD.
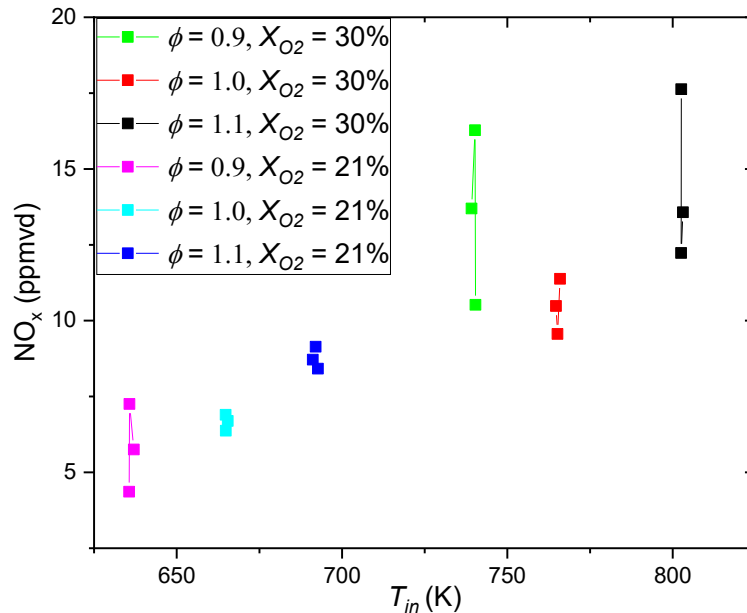
Figure 3.14: Influence of inlet temperature on NOx.

For the cases under discussion, decreasing M_r for a given inlet chemical composition equates to an increase in the net momentum injection (stronger fuel-jet). From Figure 3.15, it is apparent that a decrease in M_r has little influence on cases with low oxygen content ($\phi \geq 1.0$ with $X_{O2} = 21\%$) while showing a non-monotonous behavior for cases with higher oxygen content. This is a counter-intuitive finding as for a jet-driven combustor, more homogeneous conditions and reduced NOx are expected with increased net momentum input and increased K_v.
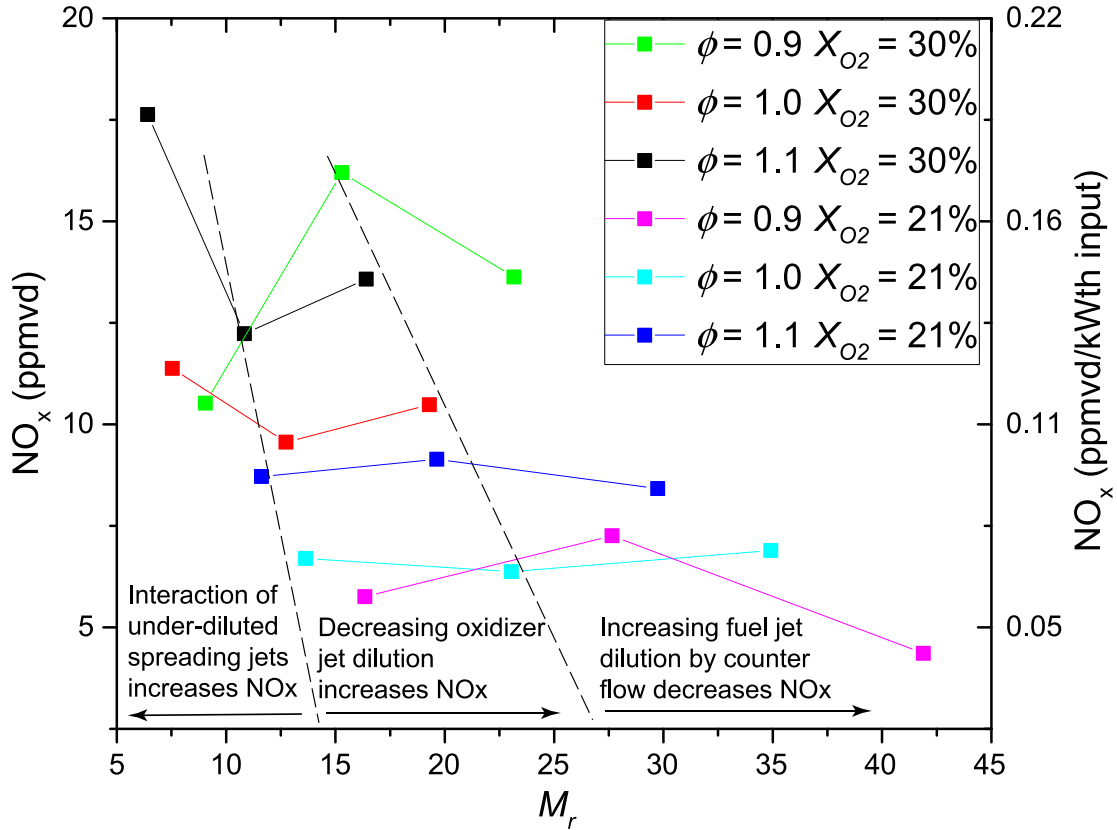
Figure 3.15: NOx dependence on M_r.

NOx formation is dependent on a complex interplay of mutually competing effects. Three regions in the M_r space are loosely identified as shown in Figure 3.15. It must be noted that the M_r region ranges are different for different inlet chemical compositions. The effect most dominantly dictating NOx trend in each region is as follows:

- Low M_r: Counter-flow driven dilution is almost non-existent with the stagnation plane being coincident with the water-cooled plate. The interaction of under-diluted spreading jets causes high temperatures and high NOx.

- Intermediate M_r: With increase in M_r in this region, l_{stag} reduces and the stagnation plane shifts upwards causing the fuel to come into contact with less diluted oxidizer jet. The oxidizer jet only undergoes entrainment driven dilution and dilution is proportional to distance (Figure 3.16).

- High M_r: Further increase of M_r beyond the previous region enhances counter-flow driven dilution of the fuel jet. The increased dilution is so overwhelming that it renders the reduced dilution of the oxidizer jet irrelevant.
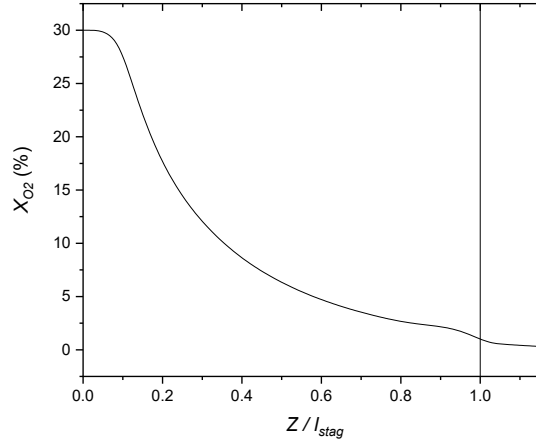
Figure 3.16: Oxygen concentration under the oxidizer jet for 13_Stoich_30. Higher gradient near $Z/l_{stag} = 1$ is due to aggressive reactions.

To summarize: A short stagnation length causes the fuel to come into contact with insufficiently diluted oxidizer (which only undergoes entrainment driven dilution). A very long stagnation length results in curtailing the counter-flow dilution of the fuel jet and allowing the spreading jets to interact directly. From Figure 3.15 it can be seen that for each inlet chemical composition, there exists an optimal M_r to minimize NOx emissions. The stagnation length is an important indicator of the overall flow pattern and needs to be optimal so that benefits of both, entrainment and counter-flow driven dilution can be attained.

One additional simulation is performed in each of the three regions and the resulting NOx values were intermediate of either edge value (Table 3.3) except for a close outlier from a narrow range (NOx for intermediate M_r).

Table 3.3: Additional tests in each M_r region.

Region	Chemical composition	M_r bounds for region	Test M_r	NOx bounds for region	Test NOx
Low M_r	$\phi = 1.1$, $X_{O2} = 30\%$	[6.41,10.83]	8.62	[17.63,12.23]	16.08
Intermediate M_r	$\phi = 1.1$, $X_{O2} = 21\%$	[11.62,19.64]	15.1	[8.71,9.14]	8.63
High M_r	$\phi = 1.1$, $X_{O2} = 21\%$	[19.64,29.74]	24.03	[9.14,8.41]	8.74

Figure 3.15 also illustrates NOx emissions per kW thermal input. The values range from 0.05 – 0.20 ppmvd/kWth which are well within the typical range for HC. The maximum

49

NOx among all the cases tested here is approximately 18 ppmvd or 9ppmvd @ 15% O_2 or 17 ppmvd @ 3% O_2[10]. Said et al. [94] reported approximately 40 ppmvd NOx @ 15% O_2 for a 6.25 kW combustor (but higher combustion intensity than this work) with $X_{O2} = 27\%$ at $\phi = 0.8$ and showing an increasing trend with ϕ. Sánchez et al. [26] reported 2 ppmvd NOx with $X_{O2} = 30\%$ but the design used for the current work is much simpler and more practical for industries (explained in Section 3.2). Comparisons with Li et al. [32] (32 ppmvd NOx @ 3% O_2 with 1.28% N_2 in fuel and 0% in oxidizer) and Krishnamurthy et al. [22] (2 – 3 ppm NOx with 0% N_2 in fuel and oxidizer) are not appropriate due to the vast difference in the N_2 content in the reaction zone. Others like Khalil et al. [69,95] did not report NOx for the same reason (0% N_2 in fuel and oxidizer for oxygen-enriched cases). To the best of the author's knowledge, NOx emissions reported in this work are hitherto among the lowest reported for a combustor which fulfils the criteria of:

- fueled by natural gas.
- no external dilution of reactants.
- no external preheat devices; moderate internal preheat.
- heat extraction strategy similar to industrial furnaces.

3.4.3   NOx reburn

In GRI Mech. 3.0, reaction number 244 to 256 represent reaction of NO with CH_i species ($i = 0 – 3$) and its subsequent reduction. The summation of their kinetic rates is the net rate of reburn. The average NOx reburn rates along the oxidizer jet center-line are of the order of 10^{-7} kgmol/m^3s for all the cases regardless of fuel nozzle sizes. For $d_f = 16$ mm cases, the NOx reburn rates under the fuel jet are of the order of 10^{-9} kgmol/m^3s with a marginal improvement to be of the order of 10^{-8} kgmol/m^3s for $d_f = 10$ mm cases. Nevertheless, this improvement is still too minuscule to have any significant effect on the furnace emissions; the effect of NOx aggravation due to insufficient dilution is much larger in comparison.

---

[10] For more information on parameters used to report NOx, please see Appendix A.

3.4.4 Other pollutant emissions

Other pollutants considered in this study were CO and THC (CH_4, C_2H_2, C_2H_4, C_2H_6, and C_3H_8) (depicted in Figure 3.17). In contrast to NOx, CO is seen to be direct function of equivalence ratio and is affected by geometry to only a minor extent. THC shows similar behavior and along expected lines, it is almost completely consumed for all lean cases and the emissions are essentially zero; while there is a small content in the exhaust for stoichiometric and rich cases. The effect of reduced counter-flow diffusion of fuel is also seen (best visible for rich cases). Both CO and THC emissions are higher for cases with $X_{O2} = 30\%$ which may be attributed to reduced mixing rates of the reactants due to lower inlet momentum.
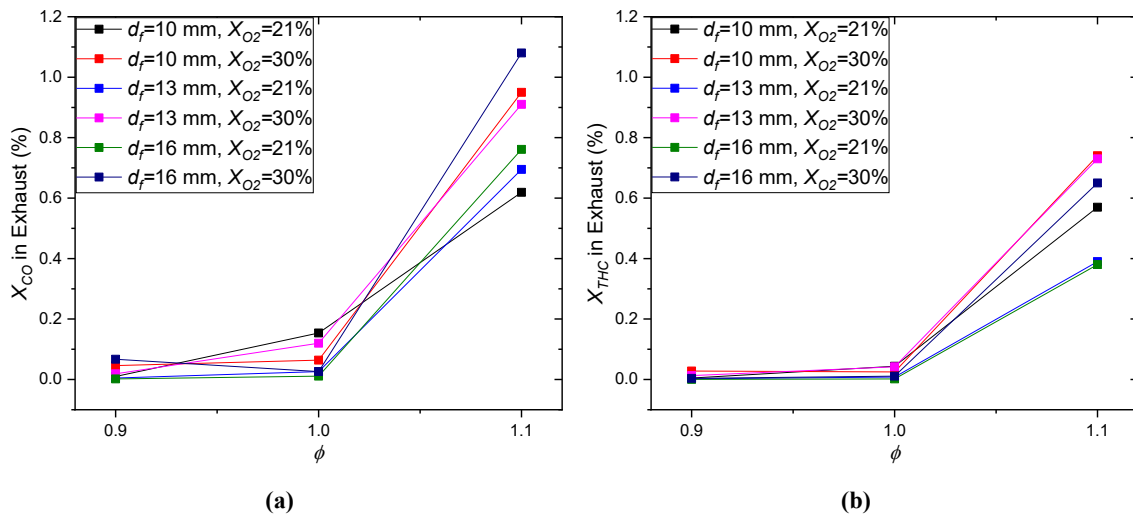
Figure 3.17: THC and CO emissions.

This behavior with equivalence ratio is consistent with some reports in the literature [11,16] and contrary to some others [15,79]. The trends are analogous to what can be expected from a "Perfectly Stirred Reactor (PSR)". However, that is not to imply that the combustor operates as a PSR.

3.4.5 Mode of combustion

The author does not claim that the cases reported adhere to the MILD or FLOX or HiTAC or flameless or CDC regime. The terms are mentioned as the cases reported here are conceptually similar to them. The author has not tried to establish a particular mode of combustion. The aim was to minimize NOx emissions in a setup that closely mimicked actual industrial furnaces.

Based on the definition of HC as a mechanism to suppress NOx formation [68], all the cases can be said to be in HC mode. However, this is a highly subjective categorization. To quantify it, NOx emissions have been combined with other metrics and the behavior is analyzed. The metric of approximately 15% variation in temperature [8] is unfit for cases reported in this work as all of them lie very close to the 15% "borderline" (Figure 3.18(a)). Maximum concentration of flame marker OH radical (Figure 3.18(b)) is seen to behave poorly for enriched oxidizer cases. Standard deviation of heat release rate (σ_{HRR}) (Figure 3.18(c)) is seen to be the best metric (working for both regular and enriched-oxidizer cases) in identifying the tendency of shift towards conventional combustion.

(a)

(b)

(c)
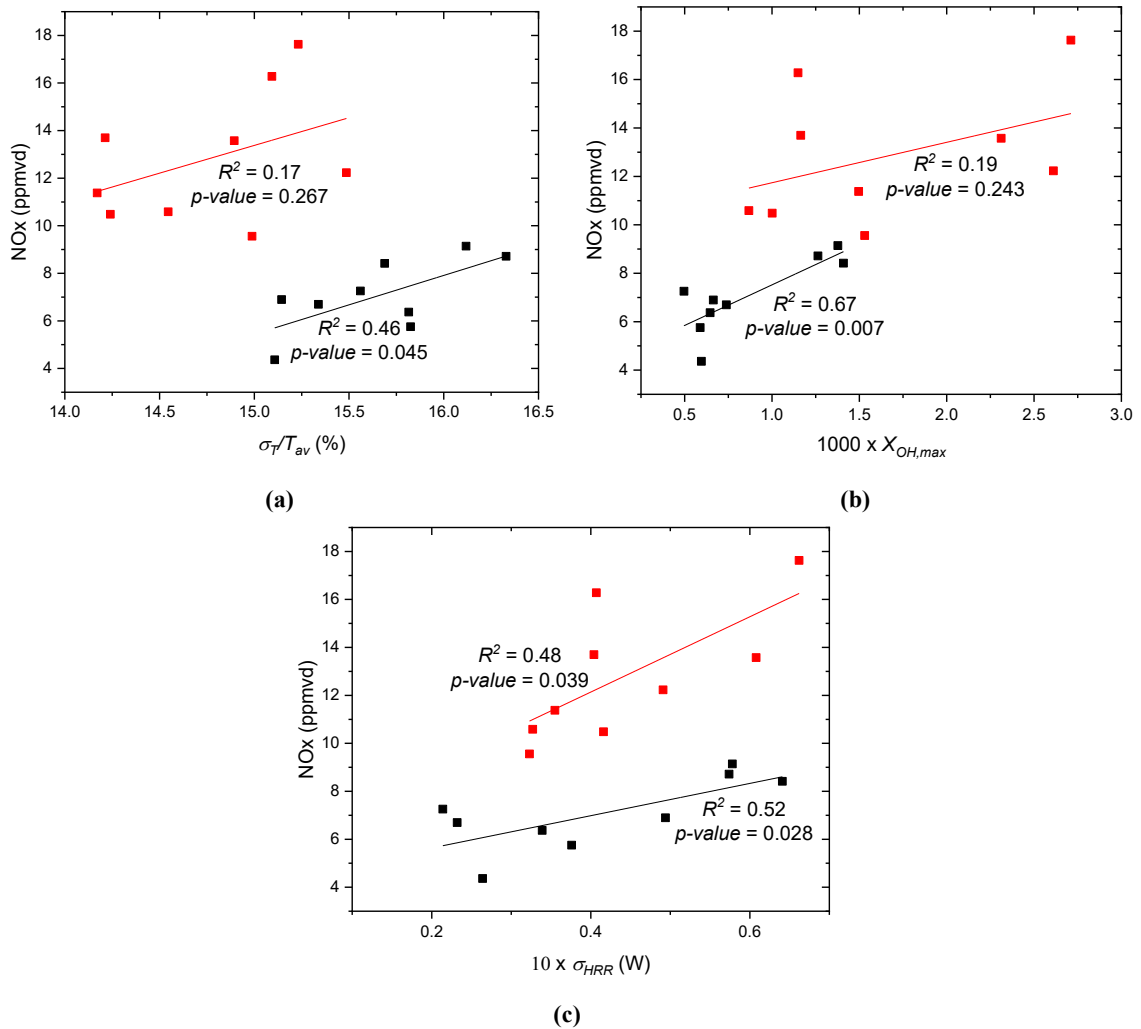
Figure 3.18: Mode of combustion. Red = Cases with X_{O2} = 30%, Black = Cases with X_{O2} = 21%. All parameters on the x-axis are calculated for the Y-plane and not for the whole volumetric domain.

3.4.6 Damköhler number

Two *Damköhler* numbers (*Da*) are defined as described in Equations (3.6) and (3.7).

$$Da = \frac{\tau_{flow}}{\tau_{chem}} = \frac{2k/\varepsilon}{\rho\left(\frac{Y_{CH4}}{\dot{\omega}_{CH4}} + \frac{Y_{O2}}{\dot{\omega}_{O2}}\right)} \tag{3.6}$$

$$Da = \frac{\tau_{flow}}{\tau_{chem}} = \frac{2k/\varepsilon}{\dfrac{\rho C_p (T - T_{in})}{q_{sp}}} \tag{3.7}$$

Equation (3.6) describes *Da* based on the main reactant species where while Equation (3.7) describes *Da* based on a progress variable (using temperature as a progress variable).

Only three[11] *Da* contours each (for 10_Stoich_30, 13_Lean_30, and 16_Rich_21) are shown in Figure 3.19 and Figure 3.20 but all the profiles have characteristics described as follows. The profiles using both approaches are qualitatively similar. The absolute values are reasonably low and close to unity. The shape of the profile is found to be a function of only the inlet chemical composition (ϕ, X_{O2}). And it forms a balloon around regions of low availability, i.e.:

- around the oxidizer nozzle for rich cases
- around the fuel nozzle for lean cases.
- thin sheet between the nozzles for stoichiometric cases.

Also, for $X_{O2} = 21\%$, the contours are slightly offset from the fuel/oxidizer nozzle just like a lifted flame. Whereas, for $X_{O2} = 30\%$, the profile is seen to be attached to the fuel/oxidizer nozzle like an anchored flame. This behavior is confirmed to not be a function of momentum. For example, for 16_Rich_21, despite the comparatively low momentum of the oxidizer jet, the profile is offset from the nozzle.

---

[11] This set is selected to have representation of at least one of each of the varied parameters (d_f, ϕ, X_{O2}).
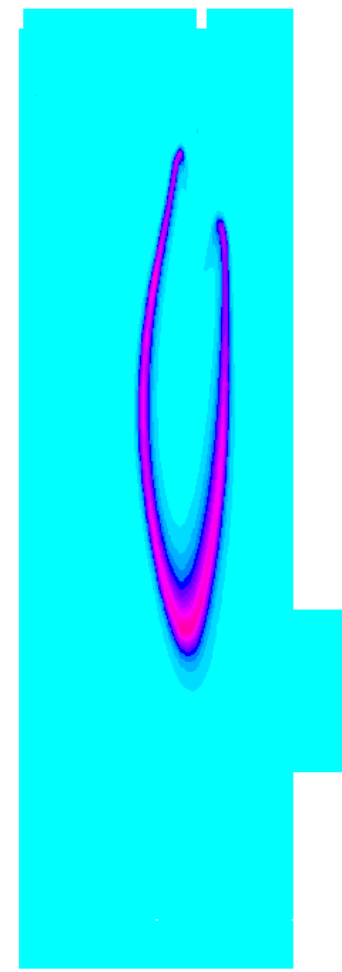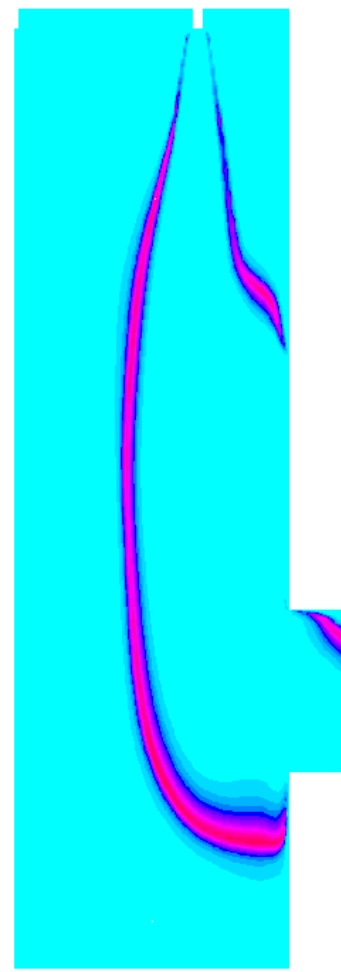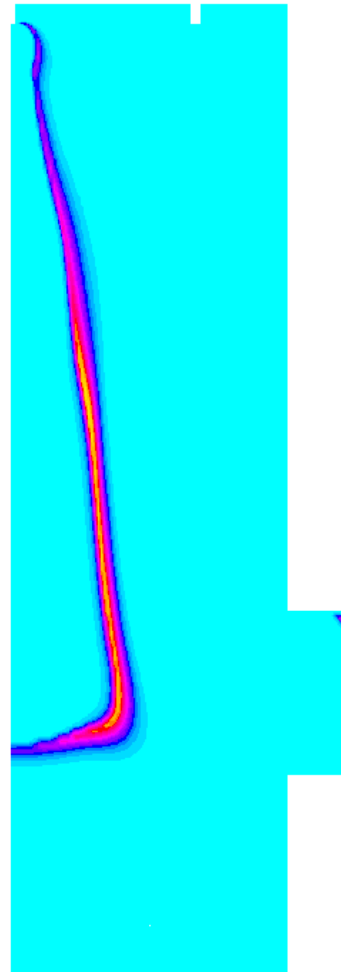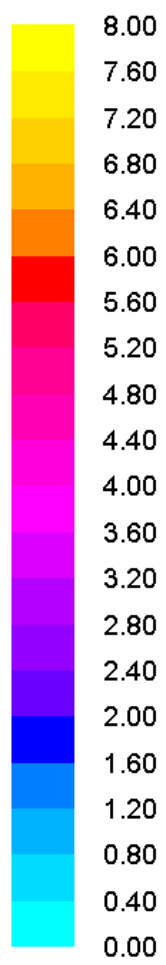
(a) 13_Lean_30 **(b) 10_Stoich_30** **(c) 16_Rich_21**

Figure 3.19: *Da* **contour plots based on main reactant species (Equation (3.6)).**
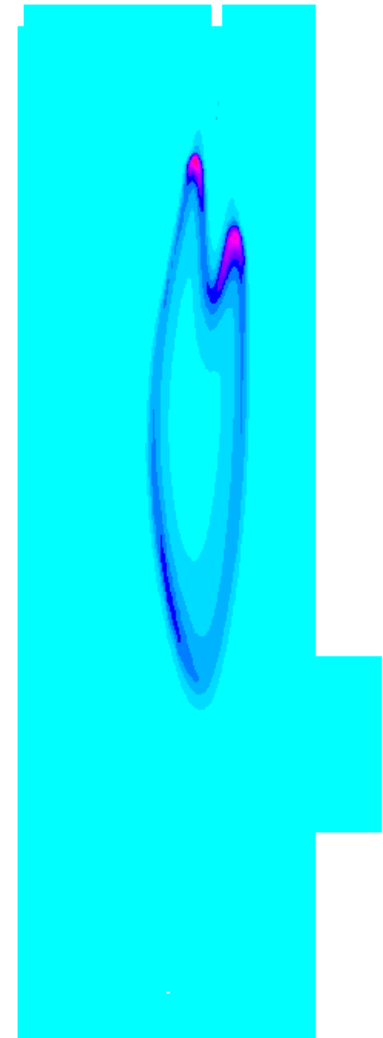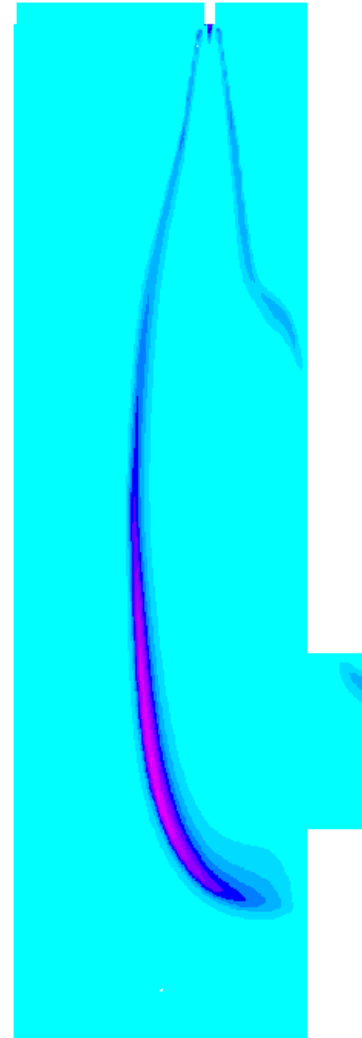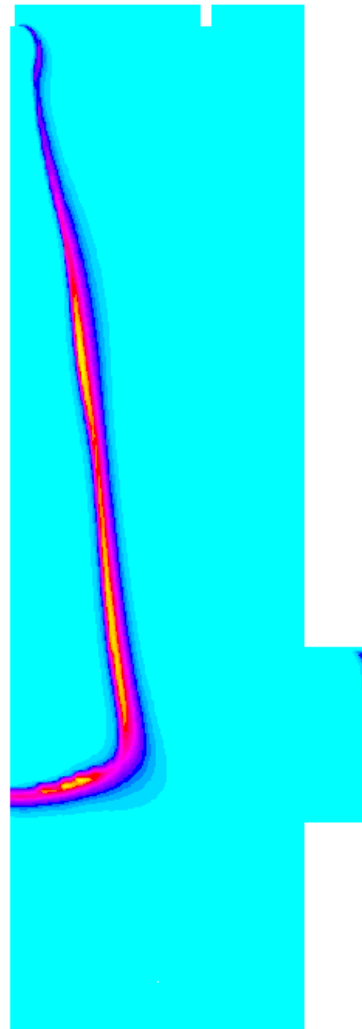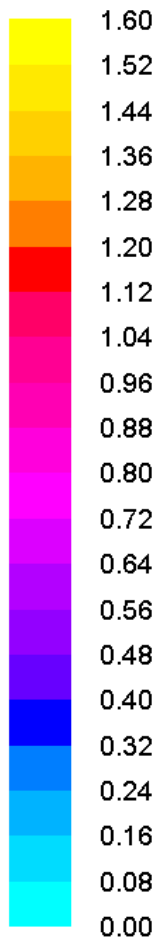
(a) 13_Lean_30 **(b) 10_Stoich_30** **(c) 16_Rich_21**

Figure 3.20: *Da* **contour plots based on a progress variable (Equation (3.7)).**

55

3.5   Concluding Remarks

Homogeneous Combustion (HC) with enriched oxidizer streams has been investigated numerically on a 91.7 kW furnace to facilitate design for the industry. The furnace studied had a parallel jet configuration and by comparing the flows with canonical flows, predictive tools were developed for the flow underneath the jets. These were found to essentially be independent of the inlet chemical composition of the incoming reactants and hence may be applicable to a broad range of reacting/non-reacting confined turbulent jet setups. Increasing recirculation rates by reducing fuel-jet size was shown to have negligible influence on NOx emissions.

Stagnation length was suggested as a length scaling parameter to account for the influence of multiple nozzles. It performed well in describing a variety of cases with the shape of the velocity curve dependent only on inlet momentum ratio. Stagnation length was also seen to be indicative of the macro flow structure and it emerged as a parameter of interest in analyzing NOx emissions. A stronger fuel jet was seen to improve NOx reburn but the improvement was not significant enough to reduce overall emissions.

It was shown that HC can be attained with enriched oxidizer streams for high-temperature industrial applications. Conditions which promote and inhibit HC were reported. CO and THC emissions were found to be dependent on the global equivalence ratio and largely independent of the geometry. Unlike the behavior of HC with respect to oxidizer-jet momentum, the behavior with respect to fuel-jet momentum was nuanced and not straightforward. It was opined that future work into expanding HC to attain low NOx performance with enriched oxidizers has to be guided by geometry and flow optimization; as opposed to high preheat of the incoming reactants (which is one of the most well-established ways to attain HC for $X_{O2} \leq 21\%$ [76]). Such work can potentially lead to development of ultra-low NOx systems while suffering no (or minimal) CO and hydrocarbon emissions penalty.

Chapter 4:

The Effect of Nozzle Design on Homogeneous Combustion

4.1   Introduction

Intense dilution of incoming reactants enables the overall control of Da close to unity and the establishment of HC. A parallel-jet configuration is commonly used for industrial furnaces and Chapter 2 & 3 discuss strategies to establish HC in such setups. Two processes driving the dilution and decay of the fuel-jet in a parallel-jet SJWJ configuration are discussed in Chapter 3. Whereas, the oxidizer jet undergoes dilution through only one mechanism i.e. entrainment. As efforts are made to expand Homogeneous Combustion (HC) to higher rates of oxygen enrichment (X_{O2}), the oxidizer jet presents an opportunity i.e. potentially a secondary process of jet dilution. For a given thermal input and equivalence ratio (ϕ), increasing oxygen enrichment (X_{O2}) reduces the oxidizer jet momentum which reduces its entrainment driven dilution; and also reduces the counter-flow driven dilution of the fuel-jet in a parallel jet setup. Therefore, enabling an additional mechanism for oxidizer jet dilution attains more significance with increasing X_{O2}.

HC combustors are generally driven by high-momentum reactant inlet jets which is also true for the setup being studied for this work. Nozzle design and injection strategy, therefore, expectedly become topics of interest in this endeavor. This work studies two such strategies, namely, the effect of nozzle shape and, the effect of localized swirling injection on HC. Discussed in greater detail in Section 4.2, a localized swirling injection strategy can have some advantages as opposed to a tangential injection strategy which produces a global swirl within the combustor. Just like Chapter 3, this study also lays emphasis on practicality considerations in terms of:

- heat extraction strategy.

- no external dilution of reactants.
- no specialized external devices or regenerators for preheat; moderate preheat via a simple internal recuperative setup.

4.2   Literature Review

The effect of geometry on HC has been extensively reported on in literature. Tu et al. [96] have worked on optimizing the furnace chamber shape and report that compared to a cuboidal chamber, a chamber shaped like a frustum of a pyramid is better to enhance recirculation and reduce NOx. Work has also been done on chamber configuration and Reddy et al. [97] settled on a staged combustion approach whereas, Arghode et al. [16,78,79] concluded that a single-stage, "reverse-flow" configuration resulted in the highest homogeneity and least NOx. More discussion on this is available in Chapter 3.

As far as nozzle geometry is concerned, previous studies have reported on nozzle configuration [98], number of nozzles [98], and nozzle size [7,80,99]. The conclusions here appear to be that smaller oxidizer nozzles are conducive to better HC, fuel nozzle size has to be optimal, and nozzle number/configuration should be subjectively decided for individual geometries. A knowledge gap here is the utilization of non-circular nozzle geometries with sharp corners (e.g. square nozzles). The effect of square nozzles on HC and NOx emissions is tested and reported in this work. The conjecture is based on reports by Callender et al. [100,101] and Tam et al. [102] who have investigated such geometries (chevron nozzles) for aircrafts. However, they investigated such nozzles for downstream applications as the aim was reducing acoustic signatures of aircraft engines. They concluded that the higher vorticity arising from the sharp edges enabled better mixing of the hot products of combustion with ambient cold air and thus reduced noise. The anticipation for this work is that higher vorticity arising from the sharp corners can enhance the dilution of the reactant jets; thus, creating favorable conditions for HC and thereby reducing NOx.

Another strategy that has been extensively studied for HC combustors is utilization of a swirling flow field. While this is a fairly established technique with commercial applications in conventional gas turbine combustors, it is an active topic for research as far

as applications in HC combustors are concerned. Listed by Sheen et al. [103], swirling flow fields are generally established by one of the following methods:

- Tangential entry into the reaction chamber.
- Turning vanes or similar inserts in the injection nozzle.
- Mechanical rotation devices (impellers, rotating reaction chamber wall, precessing injection nozzle etc.).

Tangential entry (Figure 4.1) enables a global or a chamber wide swirling flow field whereas turning vanes/nozzle inserts (Figure 4.2) produce a localized swirling flow emanating from the injection nozzle (like a corkscrew).
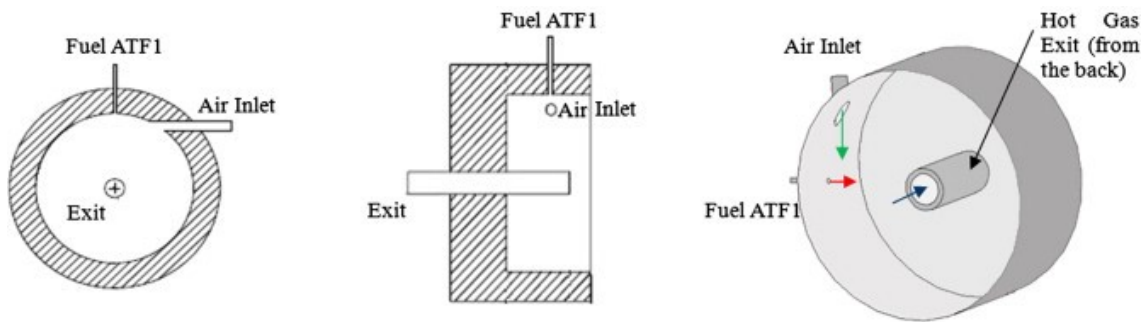
Figure 4.1: Tangential entry or global swirl design used by Khalil et al. [104].

The biggest advantage offered by swirling vane inserts over tangential injection is the possibility of retrofitting into currently existing setups with minimal intrusion. Modifying current setups to have tangential injection will require major changes to the overall furnace design. Most work on swirling flow-fields with HC employ global swirl or tangential injection [104–108] while some have employed bluff-body generated swirl [109]. A limited number of studies have utilized the turning vane or localized swirl approach for HC [35,110]. Studies by Reddy et al. [97,111] have utilized both approaches together while Gupta et al. [112–115] utilize the turning vane approach to inject premixed reactants into small chambers such that a chamber-wide swirling structure is observed. A limited number of reports are available for swirl-assisted HC with natural gas as the fuel [105–107,112] or for swirl-assisted HC with oxygen enrichment [113]. Studies on HC with localized swirl have used kerosene/JP-8 [97,110,111], diesel/light-oil [35,97], gasoline [97], coal [35], biogas [104], syngas [104], landfill-gas [104], propane [114,115],

coke-oven gas (H_2 + CH_4) [112,113,115] and ethanol [110]. Natural gas/methane is the most industrially relevant fuel in the US [1] and therefore a study of methane burning with enriched oxidizers is necessitated. It should be pointed out that Khalil et al. [104] simulated biogas and landfill-gas by mixing methane with CO_2 or N_2 with the highest tested CH_4 concentration being 80%. This is conceptually similar to external dilution or premixing employed by Li et al. [32], Szegö et al. [68], Sorrentino et al. [108], and Khalil et al. [110]. The benefits and practicality concerns of such premixing are discussed in detail in Section 3.2. This study reports on "pure" fuel (as available commercially with less than 5% inert content) reacting with oxy-enriched oxidizers ($X_{O2} > 21\%$ with remnant being N_2). Further discussion on available literature on oxy-enriched HC and the knowledge gap therein is available in Chapter 3.

The major part of this study is carried out numerically with the support of some experiments. This is done to gain a deeper insight into the complex 3-D flow in a furnace with limited optical access. To summarize: This investigation reports on efforts to establish HC with natural gas and oxygen-enriched oxidizers; with emphasis on the influence of the following:

- Square nozzles.
- Swirling injection of oxidizer.
- Swirl intensity (in terms of Swirl Number (S)).

4.3   Numerical Model

4.3.1   Geometry

The details of furnace geometry are described in Chapters 1, 2, & 3 and therefore, not discussed here. Since only the oxidizer jet has a swirling component, the arguments of symmetry (Section 3.3.1) are still valid and only a quarter of the furnace is simulated.

The only modification in the geometry is in the design of the oxidizer jet (shown in Figure 4.2). To facilitate the placement of turning vanes, a nozzle would have to be annular. For the numerical simulations an annular profile is used but no turning vanes are modeled. The tangential component of velocity is provided via a boundary condition input. D_o and

D_i are selected such that $D_i = 0.4D_o$ and the annular cross section area is the same as a circle with $d = 16$ mm. Since comparisons are made with non-swirling cases as the baseline, having the same cross-sectional area enables fair comparisons as the axial component of the momenta are the same for straight injection and swirling injection cases (for a given mass flow rate). All other geometric details are the same as stated in (Section 3.3.1).
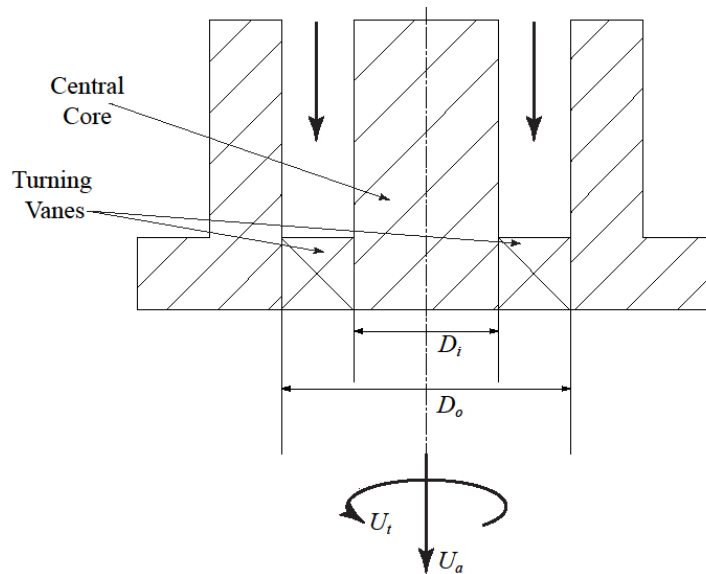
Figure 4.2: Annular oxidizer nozzle for localized swirl (not to scale).

Most of the analysis is performed on the Y-plane (plane containing both, fuel and oxidizer jets) along various axial and radial lines. These are shown in Figure 4.3 and correspond to the locations where sampling was done for the experiments (Section 4.3.5).

4.3.2 Mathematical modeling

A finite volume code, ANSYS FLUENT is used for simulating the operation of the furnace under conditions listed in Section 3.3.3. Models used for the simulations are as follows:

- Turbulence: RANS, Reynolds Stress Model (RSM), Enhanced Wall Function [83,116–118]
- Radiation: Discrete Ordinates, WSGGM [84,85]
- Chemical Mechanism: GRI Mech 3.0 [66]
- Turbulence-Chemistry Interaction (TCI): Eddy-Dissipation Concept (EDC) model [87] with In-Situ Adaptive Tabulation (ISAT) [88]

61
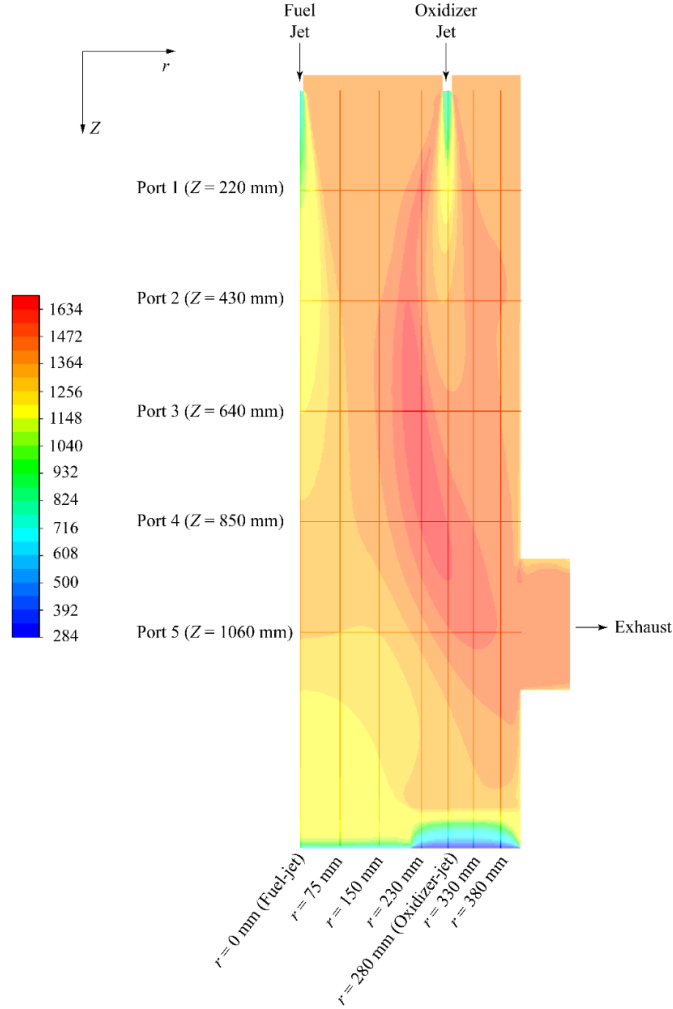
Figure 4.3: Temperature contours in the Y-plane for one of the cases (Swirl_10_35; see Section 4.3.3 for further details). Also shown are some radial and axial lines along which parameters are plotted for analysis.

For accurate capture of swirling flow-fields with combustion, the superiority of RSM over $k - \varepsilon$ in addressing turbulence closure has been established by Khalil et al. [105], Liu et al. [119], Sorrentino et al. [108], and others. Unlike the two-equation $k - \varepsilon$ model [82], RSM does not work on the isotropic eddy-viscosity hypothesis. Instead, the closure is obtained by solving transport equations for the Reynolds stresses ($\tau'_{ij} \equiv \rho \overline{u'_i u'_j}$) along with an equation for the dissipation rate ($\varepsilon_{ij} \equiv 2\mu \overline{\frac{\partial u'_i}{\partial x_k} \frac{\partial u'_j}{\partial x_k}}$). The increased computational cost for solving seven additional transport equation is justified because of the more rigorous treatment of swirl, rotation, and rapid changes in strain rate. A test was performed to see the differences in the flow fields yielded by the two turbulence models. Two computations were performed for a case with high degree of swirl (Swirl_15_30; see Section 3.3.3) using

62

$k - \varepsilon$ and RSM. Figure 4.4 presents the X-component of velocity at various axial distances from the nozzle exit. The difference in the velocity fields is the most pronounced close to the oxidizer nozzle ($r = 280$ mm and $Z = 220$ mm) which has swirling injection; and it grows progressively smaller with increasing distance from the nozzle. After a thorough grid independence study, a mesh with approximately 2.2 million elements (all hexahedral) is chosen. The average cell size is ~3 × 3 × 3 mm. Appropriate mesh refinement is performed in regions with expected high gradients and in the near-wall regions.

Like in Chapter 3, modification of EDC coefficients (C_ξ and C_τ) as per Evans et al. [89] and De et al. [90] yielded erroneous thermal fields and hence, the usual values were used ($C_\xi = 2.1377$ and $C_\tau = 0.4083$). For other parameters, the models available with the solver are utilized. Mathematical formulation, applicability, merits, demerits, and limitations of these models have been discussed in great detail in literature and therefore not discussed here in the interest of brevity.
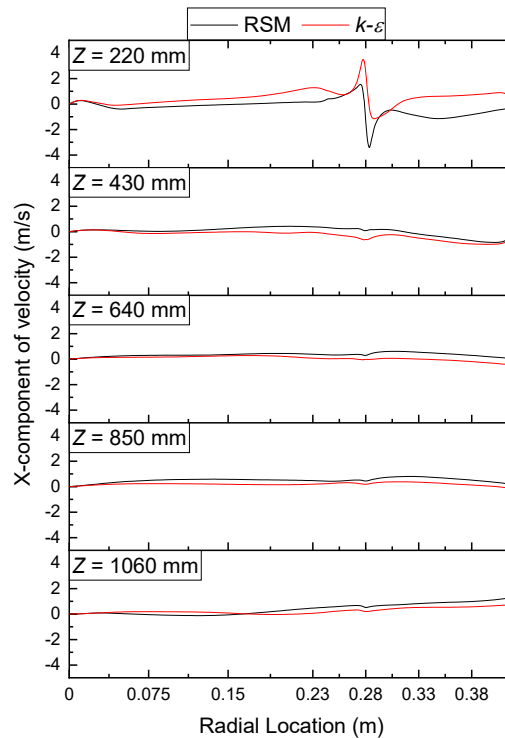
Figure 4.4: Comparison of RSM and $k - \varepsilon$ turbulence models.

4.3.3 Parameter Space and boundary conditions

Parameters kept constant for all cases were:

- mass flow rate of fuel (equivalent to 91.7 kW chemical heat input in the non-reduced domain)
- cross sectional area of the nozzles (A_f = 132.73 mm^2 and A_o = 201.06 mm^2)
- fuel-jet composition (X_{CH4} = 95% and X_{N2} = 5%)
- equivalence ratio (ϕ = 1.0).

Parameters varied were oxygen content in the oxidizer stream (X_{O2} as listed in Table 4.1 the remnant is N$_2$) and swirl number of the oxidizer jet (S). The latter is defined as per Sheen et al. [103], "like" a ratio of axial flux of tangential momentum (J_t) and axial flux of axial momentum (J_a).

$$S = C \frac{J_t}{R_o J_a} \tag{4.1}$$

$$J_t = \int_0^{R_o} (U_t r) \rho U_a \cdot 2\pi r dr \tag{4.2}$$

$$J_a = \int_0^{R_o} (U_a) \rho U_a \cdot 2\pi r dr \tag{4.3}$$

Sheen et al. [103] termed this as a modified swirl number and used 0 instead of R_i for the lower bounds of the integrals in Equations (4.2) and (4.3). This was done so that for mean axial and tangential velocities, Equation (4.1) simplifies to Equation (4.4). Paraphrasing the authors, the modified swirl number has a greater physical meaning as it is linearly proportional to the ratio of mean tangential and axial velocities ($\equiv \beta$) [103].

$$S = 0.75 \frac{U_t}{U_a} = 0.75\beta \tag{4.4}$$

One more case was simulated to ascertain the impact of nozzle shape (last case in Table 4.1). It had square nozzles for fuel and oxidizer injection.

Table 4.1 lists out some details of the computational cases. Reynolds numbers for the jets are calculated post-simulation. Across cases, Re varies for fuel-jets because of varying

temperatures while for oxidizer-jets[12] it varies because of varying mass flow rates and temperatures. See Section 3.3.1 for more details on inlet temperatures.

Table 4.1: Details of cases simulated.

Case	X_{O2}	S	β	Re_f	Re_o
Circular_21	21	0	0	7800	11900
Swirl_05_21	21	0.05	0.075	7900	12000
Swirl _10_21	21	0.10	0.15	7900	11900
Swirl _15_21	21	0.15	0.225	7900	12000
Circular_30	30	0	0	7700	7500
Swirl _05_30	30	0.05	0.075	7700	7500
Swirl _10_30	30	0.10	0.15	7700	7500
Swirl _15_30	30	0.15	0.225	7700	7500
Circular_35	35	0	0	7500	6000
Swirl _05_35	35	0.05	0.075	7500	6000
Swirl _10_35	35	0.10	0.15	7500	6000
Swirl _15_35	35	0.15	0.225	7500	6000
Circular_40	40	0	0	7200	5200
Swirl _05_40	40	0.05	0.075	7300	5200
Swirl _10_40	40	0.10	0.15	7300	5200
Swirl _15_40	40	0.15	0.225	7300	5300
Square_30	30	0	0	6600	10100

Boundary conditions are imposed based on the particular parameter set (Table 4.1) to be tested. The values are as follows:

- Mass flow rate of fuel; $m_f = 0.0004583$ kg/s (equivalent to 91.7 kW chemical heat input in the non-reduced domain)
- Fuel jet composition: see page 33

---

[12] *Re* for oxidizer-jets are calculated based on only the axial component of the velocity.

- Oxidizer jet composition: see page 33

- Tangential component of oxidizer jet: β from Table 4.1 with axial component as unity.

- Mass flow rate of oxidizer; m_o: Calculated based on X_{O2} of a particular case for the fixed m_f and ϕ.

- Wall temperature; T_w: Data taken from experiments

- Heat sink; Convective heat removal rate $h = 424$ W/m^{2}K; value taken from Shin [74] and Lee [75].

4.3.4 Steps in performing the simulation/computation

The simulations were performed in four steps with increasing degrees of refinement. These steps and the number of iterations in each step are described below:

- Step 1: An initial thermal field is obtained using a skeletal/global chemical mechanism, namely, Westbrook-Dryer 2-step mechanism [91] with one radiation iteration every ten flow, energy, and chemistry iterations. (3000 iterations)

- Step 2: A crude solution is obtained using the detailed chemistry mechanism, GRI Mech 3.0, with a relatively high ISAT error tolerance of $\varepsilon_{tol} = 10^{-3}$. (4000 iterations)

- Step 3: The solution is refined with a finer ISAT error tolerance of $\varepsilon_{tol} = 10^{-4}$. (8000 iterations)

- Step 4: The solution is run with one radiation iteration every one flow, energy, and chemistry iteration until the solution is stable and converged. (~8000 – 18000 iterations).

The simulations were performed on a 36 core system with the University of Michigan Great Lakes computing cluster and the total walltime[13] taken for each computation was ~25 days.

4.3.5 Model validation

To validate the numerical model, comparisons have been made against experimental data (for the same conditions as those in Section 3.3.5) at 35 points in the Y-

---

[13] Physical time taken for a computation to be performed.

plane within the furnace (Figure 4.5). Temperatures are measured using a fine wire thermocouple and corrected for radiation. Gas analysis is performed for CO_2 (infrared two-beam alternating light method), O_2 (paramagnetic effect by the alternating pressure method), and NO (chemiluminescence due to reaction with ozone).

Numerical and experimental data are found to be in decent agreement with small deviations (especially considering diffusivity introduced in the data due to gas sampling via suction). Relatively larger deviations in the thermal field are seen in the radially outermost regions. However, considering the fact that no such deviations are seen in the species' fields (which have close interdependence with the thermal field; NOx being particularly sensitive to temperature), it was concluded that the experimental data for temperature in these regions may not be entirely accurate; possibly due to uncertainties in the parameters used for radiation correction. Another expected source of errors is the inexact radial positioning of the sampling probes due to manual operation.

(a) CO_2-distribution   (b) O_2-distribution

(c) NOx-distribution

(d) Temperature field
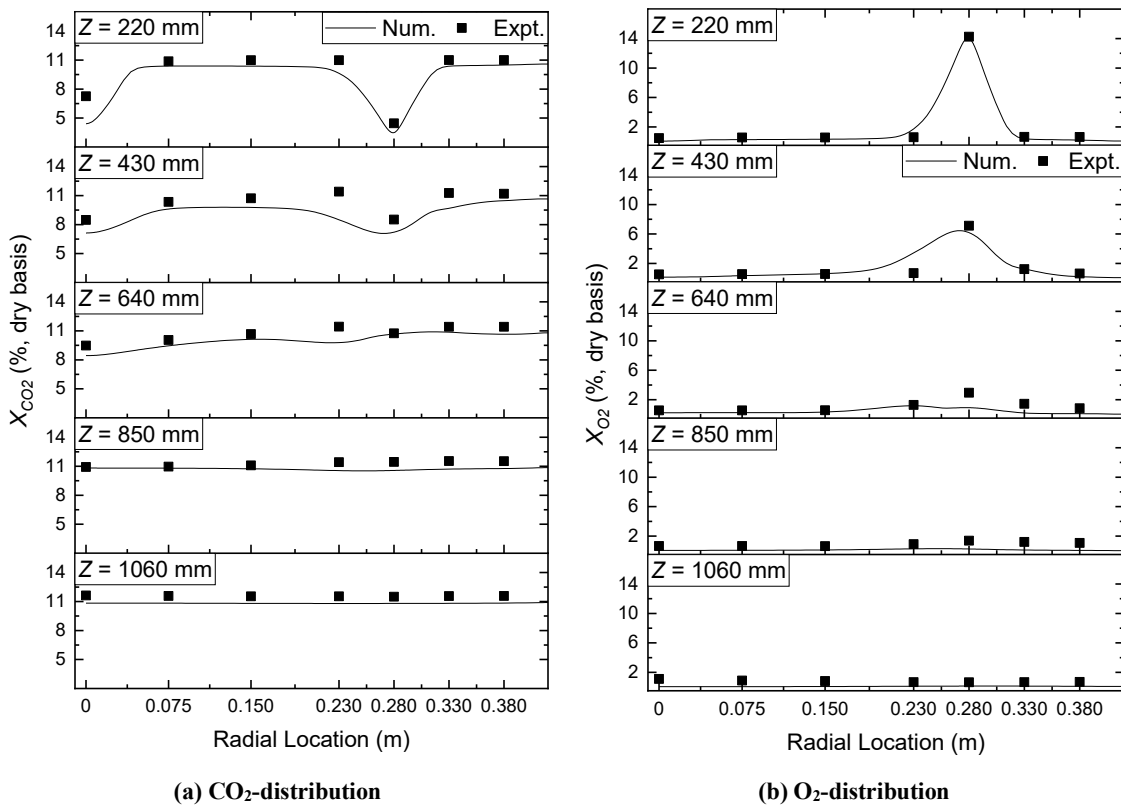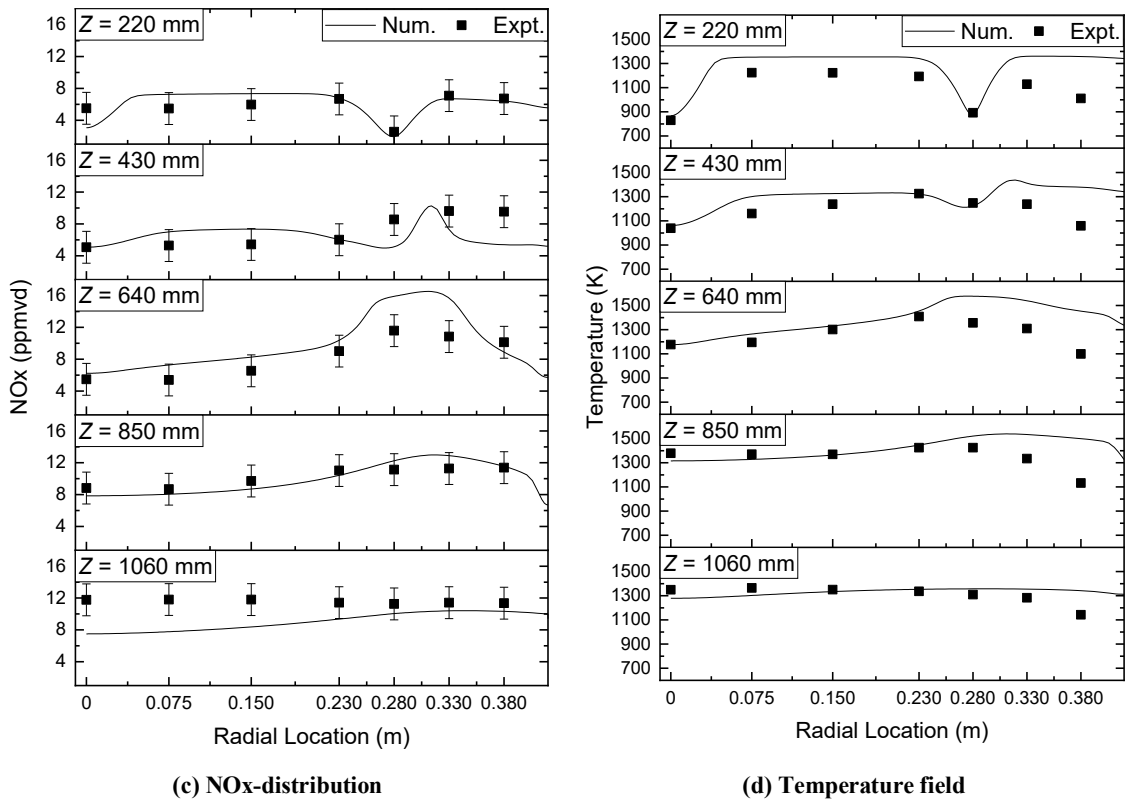
Figure 4.5: Validation of the model. For symbols with no error bounds shown, the error is of the order of the size of the symbol.

4.4   Results and Discussion

4.4.1   *NOx dependency on nozzle shape and reactant preheat*

For this study "NOx" refers to NO and NO_2 but the former is seen to constitute >99% of NOx for all cases. Inlet temperature of the reactants (mass-weighted; T_{in}) was found to have negligible influence on NOx emissions from the furnace (Figure 4.6). This is just like the finding discussed in Chapter 3 and the reasons behind it are also the same as the ones in Chapter 3.

To ascertain the influence of nozzle shape, a computation was carried out with square-shaped fuel and oxidizer nozzles. The nozzles were sized so that they had the same cross-sectional areas as mentioned in Section 3.3.3.

68
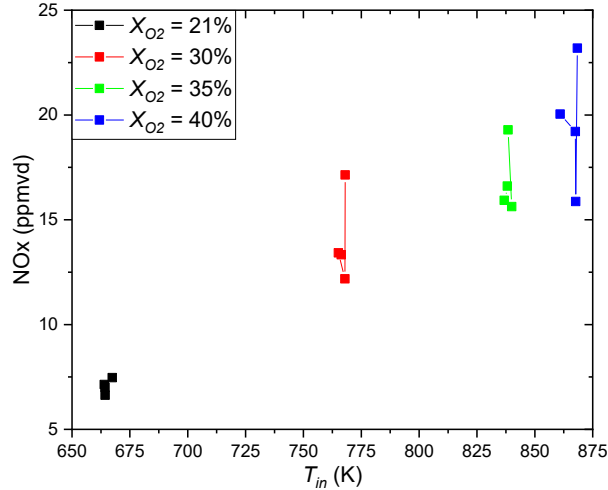
Figure 4.6: NOx as a function of T_{in}.

Fuel (methane) concentrations are plotted under ($r = 0.00$ m) and near ($r = 0.075$ m) the fuel-jet (Figure 4.7(a)). Similarly, oxidizer (oxygen) concentrations are plotted under ($r = 0.280$ m) and near ($r = 0.230$ m) the oxidizer-jet (Figure 4.5(b)). The differences in concentrations for the two nozzle shapes are seen to be minimal; suggesting that the conjecture of increased vorticity due to sharp corners may be proven wrong.

(a) CH₄ concentration
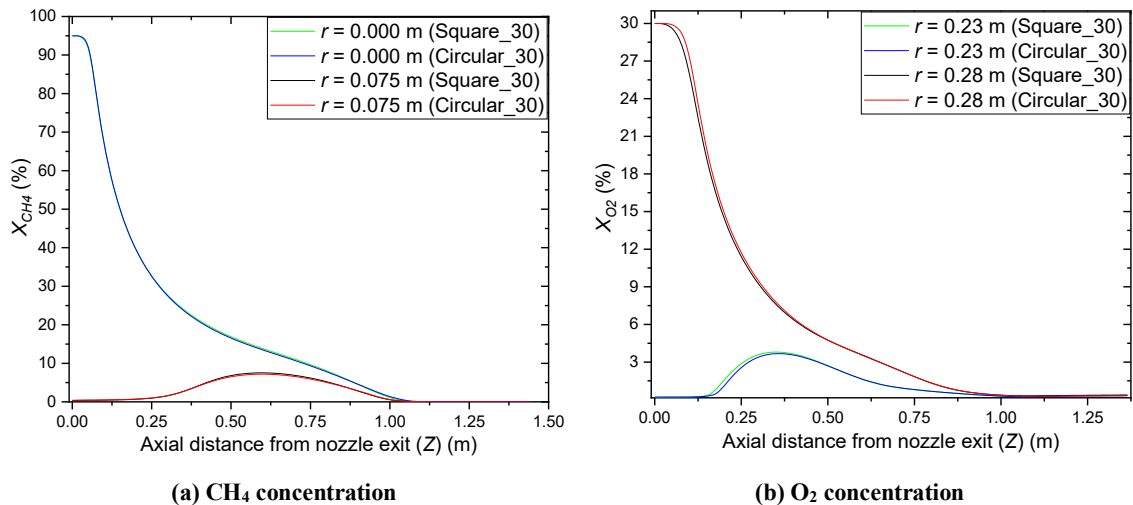
(b) O₂ concentration

Figure 4.7: Reactant concentration under and near the jets.

The vorticity magnitude ($\nabla \times \vec{U}$) near the jets was also plotted for both the nozzle designs. Figure 4.8 shows the vorticities ear the fuel and oxidizer jets for both nozzle designs. The peaks correspond to the high-shear layer near the jet periphery and the fuel-jets have expectedly lower vorticity than the oxidizer jets (lower axial momenta). Furthermore,

Figure 4.8 confirms that the change in nozzle shape facilitates limited to no enhancement in vorticity.

Together with the fact that the overall flow patterns are largely similar (M_r, l_{stag}), similar vorticity patterns ensure no change in the NOx emissions from the furnace (Figure 4.9). The failure of the conjecture can be attributed to the fact that the tests reported by Callender et al. [100,101] were performed under conditions where compressibility effects are non-negligible. Whereas, the Reynolds (Table 4.1) and Mach numbers in this work are much lower in comparison. With increasing X_{O2}, Re_o decreases further and therefore higher X_{O2}'s are not tested for square nozzles.
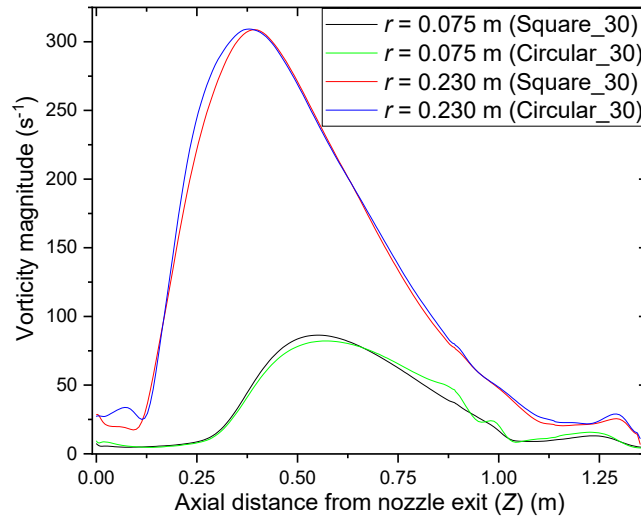
Figure 4.8: Vorticity near the jets.
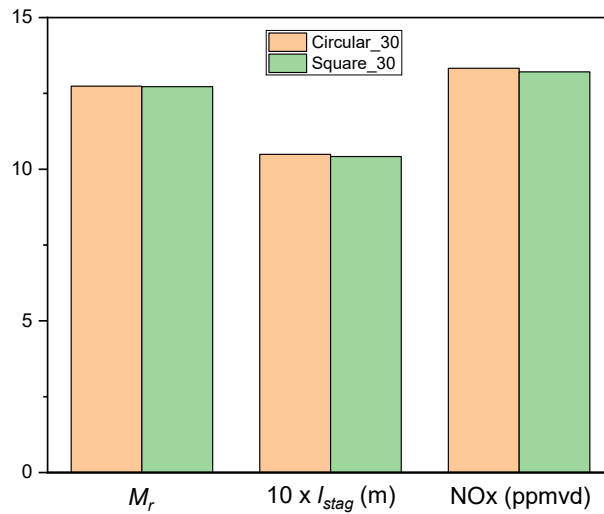
Figure 4.9: Comparison of cases to ascertain the influence of nozzle shape.

4.4.2 NOx dependency on oxygen concentration and swirl

Increasing X_{O2} causes a monotonic increase in NOx emissions. Swirl intensity (in terms of swirl number, S) is also seen to have a definite bearing on NOx emissions; with the effect being most pronounced for oxy-enriched cases ($X_{O2} \geq 30\%$). However, the relationship is not monotonous. A swirl number of 10% ($S = 0.10$) is seen to be optimal for the oxy-enriched cases in minimizing NOx emissions (Figure 4.10); beyond which, a sharp increase occurs. This is a counter-intuitive finding as highly swirling flows are expected to increase reactant dilution and thus, reduce NOx. The reasons behind this finding are investigated and the results are presented in detail in the following part of this section. Figure 4.10(b) presents NOx emissions at 15% O_2 (for more information on NOx reporting standards, see Appendix A). A similar trend is seen with $S = 0.10$ being the most optimal swirl number.

(a) NOx emissions   (b) NOx emissions @ 15% O_2
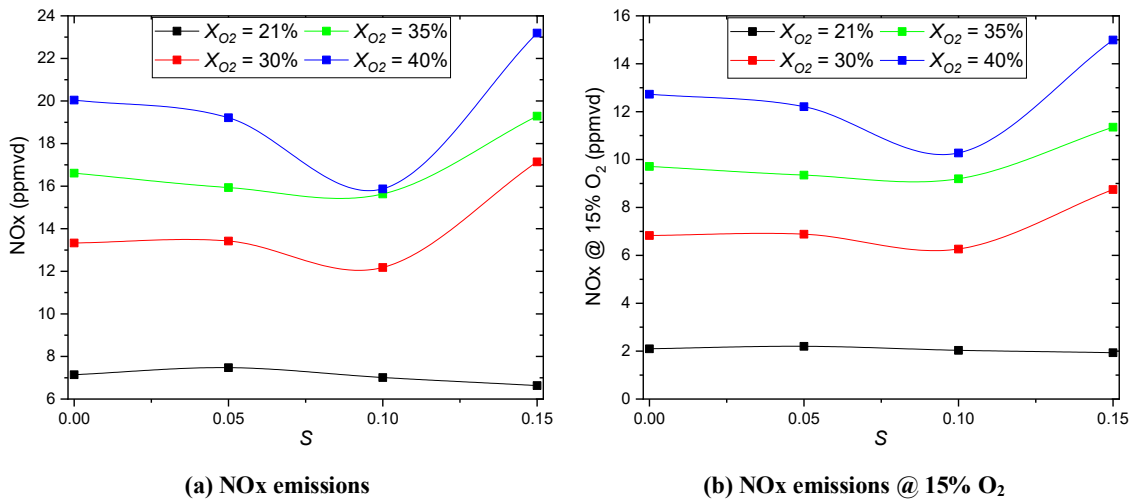
Figure 4.10: NOx emissions from furnace.

Peak temperatures in the fluid domain (T_{max}) for each case also show a trend closely resembling NOx (Figure 4.11(a)). Direct comparisons of NOx and T_{max} (Figure 4.11(b)) show that for oxy-enriched cases ($T_{max} > 1560$ K), the two quantities are strongly correlated whereas for $X_{O2} = 21\%$ cases ($T_{max} < 1500$ K), the correlation is essentially non-existent. This suggests that the thermal route is the most prominent route of NOx formation for $X_{O2} \geq 30\%$ cases; which is along expected lines.

(a) Peak temperatures　　　　　**(b) Peak temperatures v/s NOx (curve fits)**
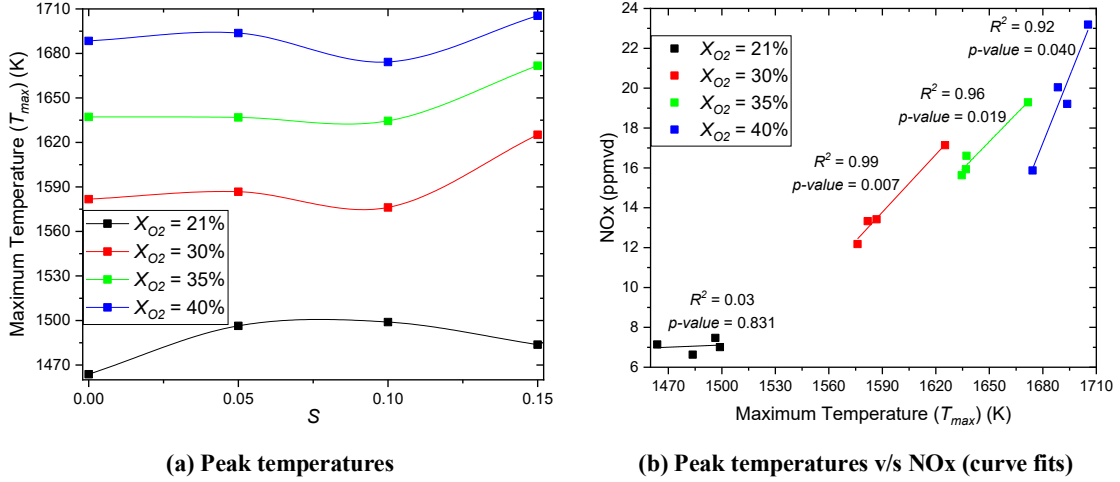
Figure 4.11: Peak temperatures for the simulated cases.

From the discussion above, it can be inferred that there must be a phenomenon competing with increased dilution of the oxidizer jet facilitated by higher swirl intensities. And for $S > 0.10$, the aforesaid phenomenon overwhelms the gains accrued due to increased jet dilution.

Reactant species' concentration at the respective jet-cores (along the jet axis) is representative of the overall jet-dilution. Instead of plotting the reactant concentrations directly, the difference of reactant concentrations with respect to a non-swirling case i.e. Circular_40 (Equation (4.5) and (4.6)) has been plotted in Figure 4.12.

$$\Delta X_i = 100 \times \left(X_i - X_{i,\text{Circular\_40}} \right) \tag{4.5}$$

$$\Delta X_i = 100 \times \frac{\left(X_i - X_{i,\text{Circular\_40}} \right)}{X_{i,\text{Circular\_40}}} \tag{4.6}$$

While the plots have been presented only for cases with ($X_{O2} = 40\%$), similar behavior is seen for each X_{O2} and therefore the following discussion is valid for all cases. It must be pointed out that Equation (4.5) yields the difference in percentage points (p.p.) (Figure 4.12(a) and (b)) while Equation (4.6) yields the difference in percentages (Figure 4.12(c) and (d)). Figure 4.12(c) and (d) have been truncated at 75 diameters, as beyond that, low absolute values of $X_{i,\text{Circular}}$ result in trivial values of ΔX_i. Furthermore, these low absolute values are also not critical with regards to NOx formation. It should also be noted that in Figure 4.12(b) and (d), axial distance is scaled by the characteristic length of the oxidizer jet i.e. $d_c = 4A_o/P$.

72
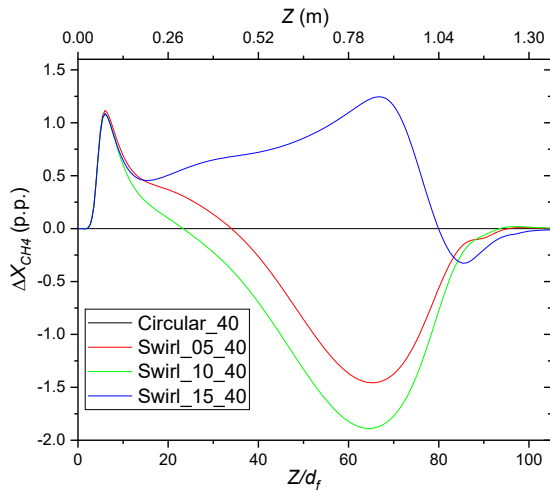
(a) Difference in CH_4 concentrations at $r = 0$ mm (fuel-jets) in percentage points (p.p.)
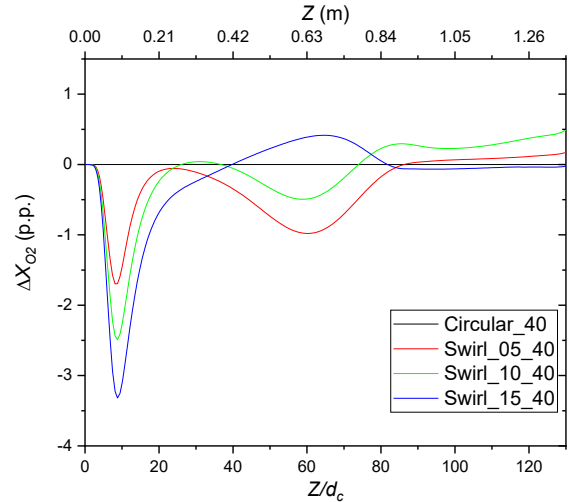
(b) Difference in O_2 concentrations at $r = 280$ mm (oxidizer-jets) in percentage points (p.p.)
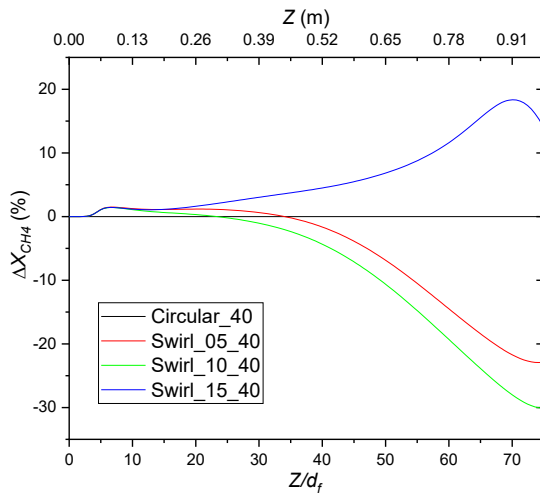
(c) Difference in CH_4 concentrations $r = 0$ mm (fuel-jets) expressed as percentages
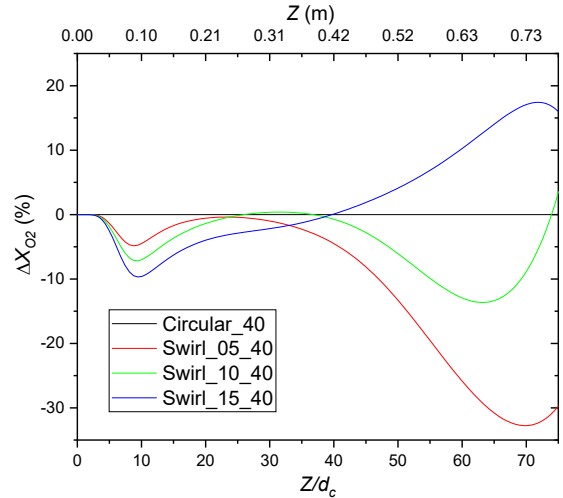
(d) Difference in O_2 concentrations at $r = 280$ mm (oxidizer-jets) expressed as percentages

Figure 4.12: Influence of swirl in reactant species' concentrations.

Figure 4.12(b) shows that fuel jets (axial injection) show different behaviors with swirling and non-swirling oxidizer jets. Further, the swirling injection, despite being localized and low intensity, alters the flow field throughout the furnace. That is, the effects of swirl can be manifested over length scales of ~75 diameters because of confinement. Based on axial distances from the nozzle exit, these effects can be classified into two categories, namely:

- Near-field effects
- Far-field effects

In the near field for oxidizer jets ($< 20d_c$), as per expectations, swirl enables better dilution with increasing swirl intensities. Somewhat unexpectedly, effects in the near field for fuel jets ($< 20d_f$) are seen as well. Fuel jets undergo reduced dilution with a swirling oxidizer jet and the reduction appears to be independent of swirl intensity for the cases tested. This is an important finding as unlike the findings in Chapter 3, the upstream portion of the jets do not remain isolated from each other; and that, there may be direct interaction between the jets in the near-field region. Moreover, the inherent nature of the flow is highly 3-dimensional in nature. Therefore, any simplified, 2-dimensional definitions of the flow structure (like in Chapter 3) are not feasible.

In the far-field ($20d_c - 75d_c$), the oxidizer jet for $S = 0.15$ is seen to have higher reactant concentrations than the non-swirling case. And within the swirling cases reactant concentrations counter-intuitively increase with increasing swirl intensities. The reason behind this was found to be reduced axial velocities (or momenta) (Figure 4.13) which in turn reduced the dilution due to entrainment. The importance of oxidizer-jet velocity/momentum and entrainment driven dilution has been established earlier in the text (Chapter 3 and Section 4.1) and in literature [7,72].

Figure 4.13 presents the axial components of velocity along the oxidizer nozzle central axis. Velocities along the axis are largely ($1d_c - 100d_c$) in the downward axial direction ($\pm 2°$). In the distance $< 1d_c$, strong recirculation under the nozzle core causes upwards velocities while beyond $100d_c$, 3-dimensional flow effects take relevance due to impingement. While the peak difference in the velocities occurs around $15d_c$, differences are noticeable until $\sim 40d_c$.

It can be deduced from Figure 4.13 that despite very similar axial components of velocity at inlet (Table 4.2), the axial components of velocity along the jet central axis are lower for higher swirl numbers. Higher swirl intensity causes more shear driven decay of jet axial velocity. This would, in turn, cause a reduction in dilution. Also, reduced axial momentum of the oxidizer jet would cause a decrease in the counter-flow driven dilution of the fuel-jet and this is responsible for the reduced dilution of the jet in the far-field. In summary, while swirl causes better dilution in the near-field, it also causes a loss of axial

momentum due to increased shear; and the effects of reduced dilution due to the latter are manifested most prominently in the far-field region.
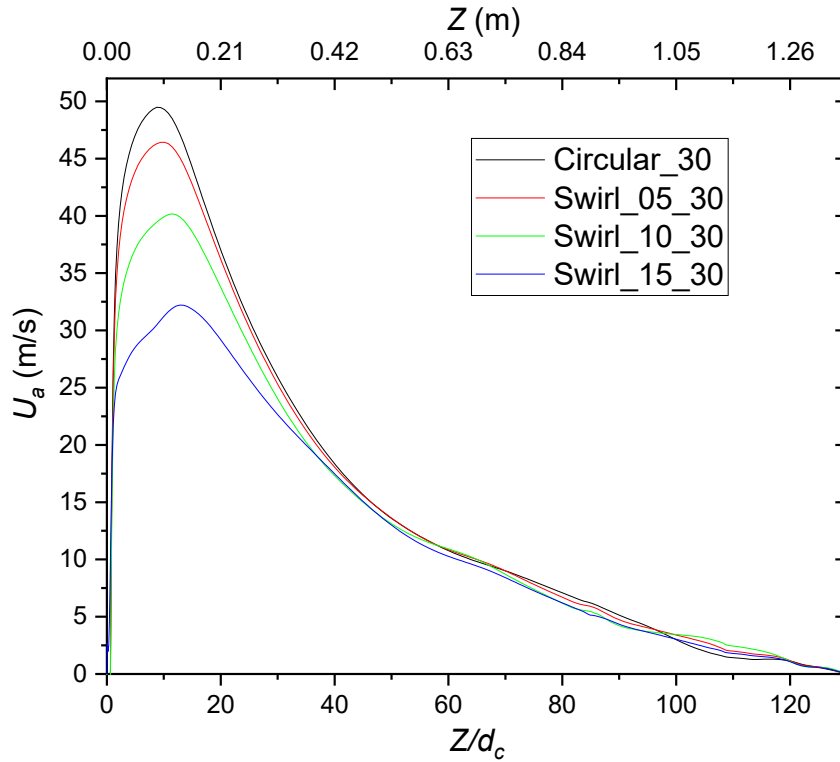
Figure 4.13: Axial component of flow velocity under oxidizer-jets.

Table 4.2: Axial and tangential components of velocity at inlet for cases presented in Figure 4.13.

Case	β	U_a (m/s)	$U_t = \beta U_a$ (m/s)
Circular_30	0	51.66	0
Swirl_05_30	0.075	51.61	3.89
Swirl_10_30	0.150	51.82	7.77
Swirl_15_30	0.225	51.82	11.66

Akin to the oxidizer-jet, in the far-field region ($20d_c - 80d_c$), the fuel jet for $S = 0.15$ also shows higher reactant concentrations. As opposed to the near-field behavior of the jet, the influence of swirl intensity is apparent in this region. Aggravated NOx for $S = 0.15$ cases can be attributed to reduced dilution of both, the fuel-jet and the oxidizer-jet.

4.4.3 Other pollutant emissions

Other pollutants considered in this study were products of incomplete combustion i.e. CO and THC (CH_4, C_2H_2, C_2H_4, C_2H_6, and C_3H_8) (Figure 4.14). For the test cases, the variations in THC (around 0 – 600 ppm) and CO (around 0 – 1600 ppm) take place over fairly narrow ranges. These pollutant emissions appear to be dictated by the same considerations as NOx, namely, X_{O2} and mixing. It must be noted that as X_{O2} increases for a fixed thermal input and ϕ, the net momentum input into the furnace reduces. For low swirl numbers ($S \leq 0.05$) both CO and THC monotonically increase as X_{O2} increases. For higher swirl numbers ($S \geq 0.10$), both drop for sufficiently high X_{O2}.

(a) THC emissions   **(b) CO emissions**
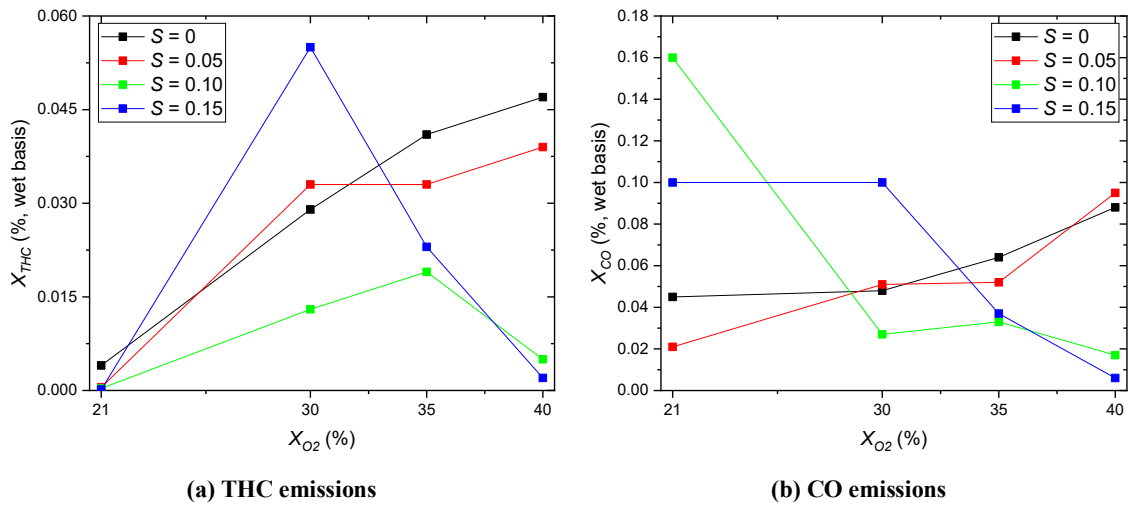
Figure 4.14: THC and CO emissions.

4.4.4 Mode of combustion

Standard deviation of heat release rate (σ_{HRR}) is used as a marker to identify the shift towards the conventional mode of combustion (Figure 4.15). It is opined that as research progresses in the field of oxy-enriched HC, the binary of flameless/flaming may be avoided. Instead, the spectrum over which this transition takes place needs to be acknowledged. Figure 4.15 shows that the metric of σ_{HRR} works well (reasonable R^2) over all X_{O2}'s tested while being statistically significant (p-value < 0.05). Most of the outliers are the cases with high swirl ($S = 0.15$) which suggests that the flow field and other properties for them are substantially different from the others.
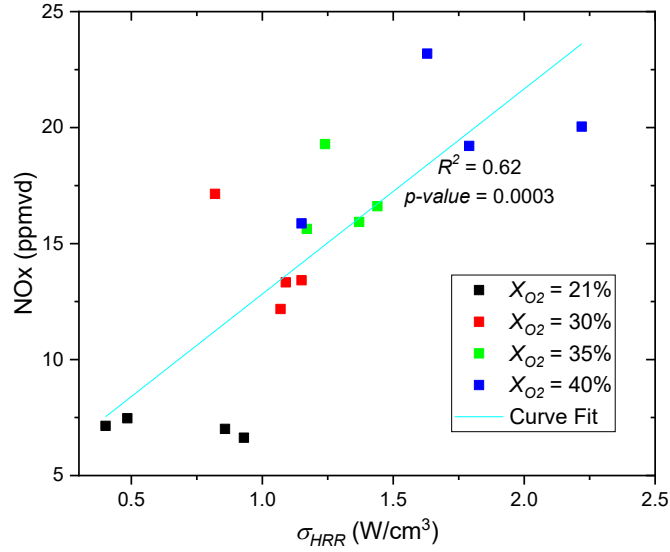
Figure 4.15: Mode of combustion.

4.4.5 *Damköhler number*

A progress variable (temperature) based *Damköhler* number was defined (Equation (3.7)) and used for comparative analysis on the effect of swirl intensity. Figure 4.16 presents the *Da* contour plots in the Y-plane for cases with $X_{O2} = 40\%$. The absolute values of *Da* are reasonably low, even for the cases with the highest X_{O2} tested here. Increasing swirl intensity causes a decrease in *Da* until $S = 0.10$. This decrease is most conspicuous in the far-field region. For $S = 0.15$, *Da* shows an increase (as compared to $S = 0.10$); which is again, most conspicuous in the far field region. In this way, the plots buttress the arguments presented in Section 4.4.2. Studying Figure 4.16 and Figure 4.17 in conjunction reveals that a significant amount of heat release happens at low *Da* conditions which are significantly away from the Burke-Schumann limit.

(a) Circular_40   **(b) Swirl_05_40**   **(c) Swirl_10_40**   **(d) Swirl_15_40**
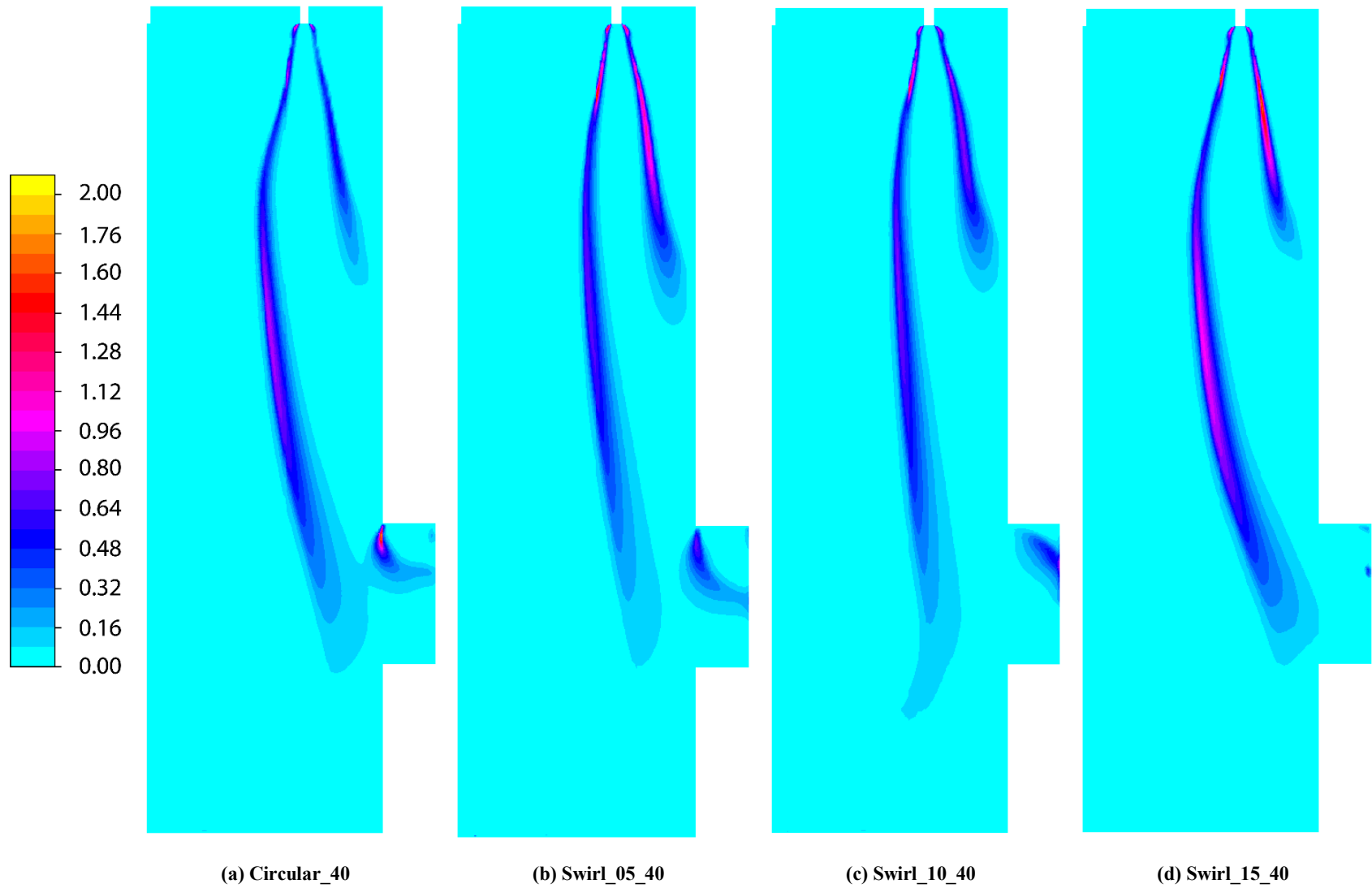
Figure 4.16: *Da* **contour plots (Y-plane) for cases with** X_{O2} **= 40%.**

(a) Circular_40   **(b) Swirl_05_40**   **(c) Swirl_10_40**   **(d) Swirl_15_40**
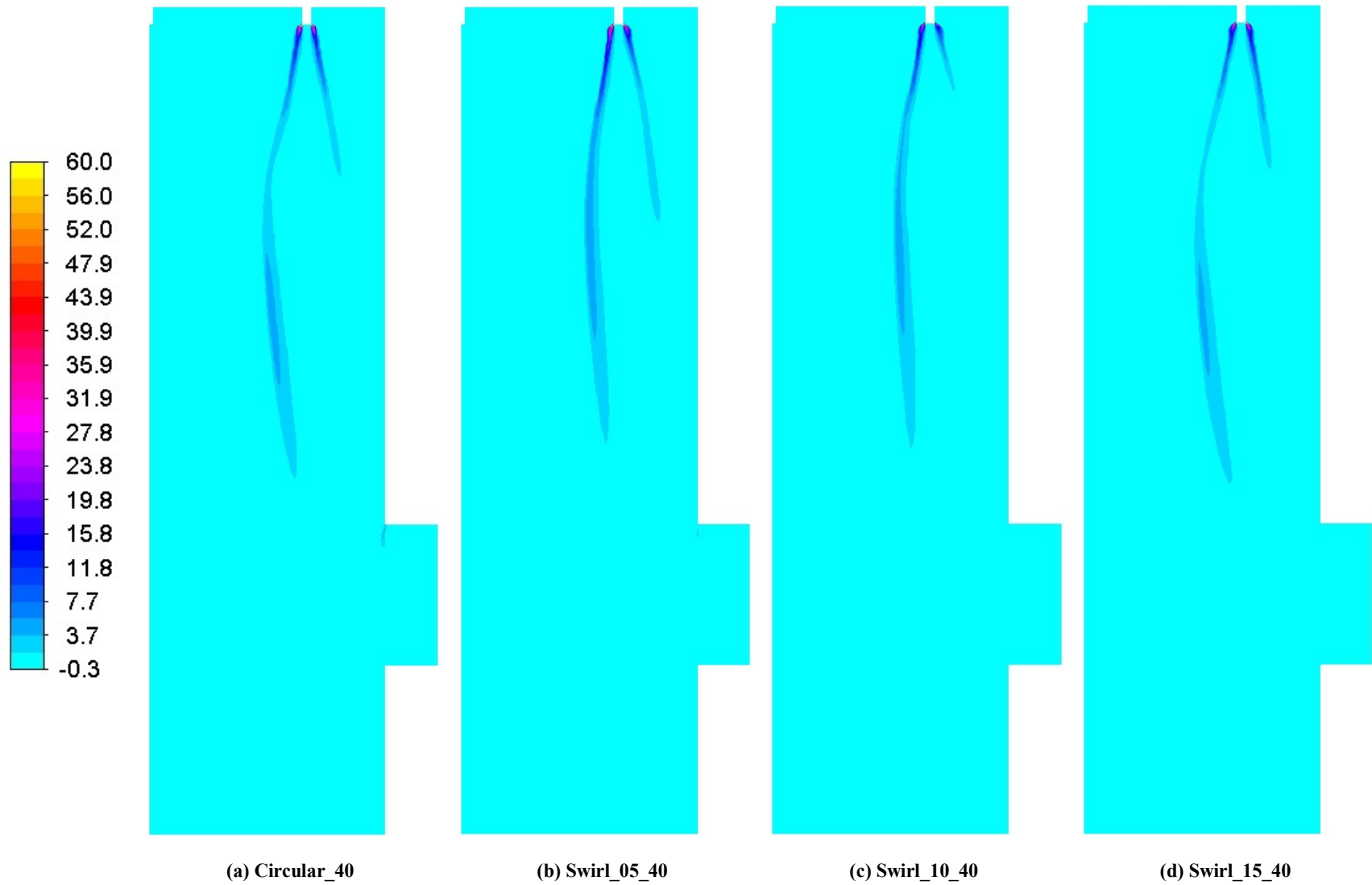
Figure 4.17: HRR (q_{sp}) contour plots (same cases as Figure 4.17). Units are W/cm³.

4.5   Concluding Remarks

The influence of nozzle geometry and of swirling injection in facilitating oxy-enriched HC has been tested here with X_{O2} up to 40%. The analysis was numerical with focus on practicality concerns so as to aid design for the industry. The aim was to enable a secondary mode of dilution (in addition to the primary i.e. entrainment) for the oxidizer jet like what was found for the fuel-jet in Chapter 3. The first strategy was to enhance vorticity driven mixing via sharp corners of the nozzle. However, the conjecture failed. It was found that altering the nozzle shape caused essentially no reduction in NOx emissions from the furnace. It was also found that NOx emissions were independent of the inlet temperature of the reactants.

The second strategy which was tested yielded more success. The strategy was to have a localized swirling injection for the oxidizer jet. While swirl did help in reducing NOx, there existed an optimal swirl number beyond which NOx emissions were aggravated to levels even higher than configurations with no swirl. Swirl, even though localized, was seen to affect the in-furnace flow field even in the far-field (~75 diameters). A mutual competition was seen between swirl assisted and entrainment driven dilution; and at higher swirl intensities, the reduction in the latter overwhelmed the enhancement accrued by the former (in terms of NOx emissions). Other pollutants tested were THC and CO. They were also found to be dictated by the same considerations as NOx, namely, oxygen content in the oxidizer stream and mixing.

The mutual competition of swirl assisted and entrainment driven dilution was also qualitatively brought out by *Damköhler* number contour plots. The absolute values of *Damköhler* numbers for the various cases were low in general and showed the same trends as NOx i.e. decreasing for swirl numbers from 0 to 0.10 and an increase for 0.15. Finally, the standard deviation of the heat release rate was used as a parameter to quantify the mode of combustion.

Chapter 5:

Conclusions, Limitations, and Future Work

5.1   Conclusions

This thesis presents three strategies that were tested towards facilitating HC in practically feasible industrial furnaces while operating with enriched oxidizers. Each chapter from Chapter 2 to Chapter 4 discuss one strategy each. The work presented in Chapter 2 is experimental in nature while that in Chapter 3 and 4 are predominantly numerical with some support from experiments. Numerical tools were employed for the work presented in Chapter 3 and 4 because the aim was to understand and explain the complex flow within a furnace with limited optical access.

Chapter 2 reports on the feasibility of soot loading in the gaseous domain to inhibit thermal runaway conditions. Fuel blends with ethylene as an additive to natural gas were tested; with the conjecture that soot will enhance heat removal via radiation and inhibit the self-accelerating cycle which causes thermal runaway. Through the usage of physics based regression models, soot was shown to enhance radiative heat-transfer. Further, it was observed that soot loading improved furnace performance and reduced emissions on a specific basis. Ethylene being an unsaturated hydrocarbon with higher reactivity tended to shift the mode of combustion away from the HC regime. While it did improve radiation, it simultaneously imposed a NOx penalty and thus, an optimal blend ratio was determined. The benefits outweighed the penalty for $X_{C2H4,f} \leq 15\%$; whereas beyond that, gains due to shift to HC regime, oxy-enriched operation, and soot loading were reversed.

Chapter 3 presents a simplified explanation of the complex 3-dimensional flow within the furnace. The furnace studied had a parallel jet configuration and by comparing the flows with canonical flows, predictive tools were developed for the flow underneath the jets. These were found to essentially be independent of the inlet chemical composition

of the incoming reactants and hence may be applicable to a broad range of reacting/non-reacting confined turbulent jet setups. Increasing recirculation rates by reducing fuel-jet size was shown to have negligible influence on NOx emissions. Stagnation length was suggested as a length scaling parameter to account for the influence of multiple nozzles. It performed well in describing a variety of cases with the shape of the velocity curve dependent only on inlet momentum ratio. Stagnation length was also seen to be indicative of the macro flow structure and it emerged as a parameter of interest in analyzing NOx emissions. A stronger fuel jet was seen to improve NOx reburn but the improvement was not significant enough to reduce overall emissions. It was shown that HC can be attained with enriched oxidizer streams for high-temperature industrial applications. Conditions which promote and inhibit HC were reported. CO and THC emissions were found to be dependent on the global equivalence ratio and largely independent of the geometry. Unlike the behavior of HC with respect to oxidizer-jet momentum, the behavior with respect to fuel-jet momentum was nuanced and not straightforward. It was opined that future work into expanding HC to attain low NOx performance with enriched oxidizers has to be guided by geometry and flow optimization; as opposed to high preheat of the incoming reactants (which is one of the most well-established ways to attain HC for $X_{O2} \leq 21\%$ [76]). Such work can potentially lead to development of ultra-low NOx systems while suffering no (or minimal) CO and hydrocarbon emissions penalty.

Chapter 4 describes the influence of nozzle geometry and of swirling injection in facilitating oxy-enriched HC with X_{O2} up to 40%. The aim was to enable a secondary mode of dilution (in addition to the primary i.e. entrainment) for the oxidizer jet like what was found for the fuel-jet in Chapter 3. The first strategy was to enhance vorticity driven mixing via sharp corners of the nozzle. However, the conjecture failed. It was found that altering the nozzle shape caused essentially no reduction in NOx emissions from the furnace. It was also found that NOx emissions were independent of the inlet temperature of the reactants. The second strategy which was tested yielded more success. The strategy was to have a localized swirling injection for the oxidizer jet. While swirl did help in reducing NOx, there existed an optimal swirl number beyond which NOx emissions were aggravated to levels even higher than configurations with no swirl. Swirl, even though localized, was seen to affect the in-furnace flow field even in the far-field (~75 diameters). A mutual competition

was seen between swirl assisted and entrainment driven dilution; and at higher swirl intensities, the reduction in the latter overwhelms the enhancement accrued by the former (in terms of NOx emissions). Other pollutants tested were THC and CO. They were also found to be dictated by the same considerations as NOx, namely, oxygen content in the oxidizer stream and mixing. The mutual competition of swirl assisted and entrainment driven dilution was also qualitatively brought out by *Damköhler* number contour plots. The absolute values of *Damköhler* numbers for the various cases were low in general and showed the same trends as NOx i.e. decreasing for swirl numbers from 0 to 0.10 and an increase for 0.15. Finally, the standard deviation of the heat release rate was used as a parameter to quantify the mode of combustion.

5.2   Limitations and Future Work

The first and most conspicuous limitation of the work in Chapter 2 is the lack of detailed soot field and soot size distribution within the furnace. A detailed soot field coupled with detailed species' and thermal fields can be used to build a comprehensive heat radiation model. To obtain a detailed soot field and soot size distribution, high power (Class 4) lasers would have to be used as scattered intensities need to be ascertained with a reasonable signal-to-noise ratio (SNR). In the current work, due to the size of the furnace the usage of an optical table was not feasible. Laser emitters and other optical equipment were placed on aluminum-strut rigs. Because of the unconventional setup, the department of Environment, Health & Safety (EHS) at the University of Michigan prohibited the usage of high-powered laser beams. To obtain a detailed soot field:

- In-situ: The experiment can be repeated with a scaled down combustor which can be placed on an optical table.
- Ex-situ: With the current combustor, the usage of specialized, custom-built, thermophoretic soot measurement equipment (like the one used by Hu et al. [57] and Puri et al. [42]) is needed.

Another limitation is the incomplete combustion of soot within the furnace. While within the furnace, soot may act beneficially, outside of the furnace, it is still an undesired pollutant. Within industrial setups, soot would need to be eliminated from the exhaust via

thermophoretic or electrophoretic scrubbers, and it also risks contaminating/deactivating the expensive catalytic converters used for after-treatment of exhaust. Future work may explore secondary oxidizer injection to oxidize soot.

Chapter 3 and 4 have similar limitations. The most prominent of which is the analysis being restricted to computational methods only. Since the aim was to understand and explain the complex 3-dimensional flow within a jet-driven combustor with limited optical access, experimental tools would not have served the purpose. Moreover, due to issues of size and required laser strengths (discussed above), even with sufficient optical access, the usage of tools like PIV would still have had concerns. This limitation can be overcome by repeating the analysis experimentally in a scaled down combustor with good optical access. Additionally, most of the discussion of the flow in Chapter 3 and 4 is limited to the Y-plane and/or under the jets. A wider analysis of the 3-dimensional flow structure along with species' fields can shed more light on dilution dynamics; especially for the analysis in Chapter 4.

On the small scale, the ISAT algorithm enables "learning" and interpolation for chemistry integration. There is an opportunity to further speed up computations (and hence the design cycle for the industry) with the application of machine-learning tools for chemistry and flow predictions. Such tools are being developed in industry (John Zink Hamworthy Combustion) and in academia (Prof. Venkat Raman's and Prof. Karthik Duraisamy's groups at the University of Michigan, Ann Arbor).

Finally, a reliable framework for scaling up of the combustor along with the understanding of the influence of combustion on materials' properties needs to be established to pave the way for industrial application.

Appendix A: Reporting NOx

Across literature, NOx is reported on dry or wet basis. Dry basis measurements are more common as they are less problematic to obtain experimentally. A cold trap (or a chiller) is placed upstream of the gas analyzers and water in the flue gas stream is condensed and drained out. The unit used in this work is *ppmvd* which stands for parts-per-million volumetric on a dry basis.

NOx measurements are sometimes normalized to a specific O_2 concentration to enable certification of a wide variety of combustion systems against regulations laid down by the federal government [120,121]. The value for *ppm$_{corr}$* or NOx at a certain O_2 is calculated using the following equation:

$$ppm_{corr} = ppm_{meas} \left[\frac{O_{2,oxid} - O_{2,basis}}{O_{2,oxid} - O_{2,meas}} \right]$$

Where,

ppm$_{meas}$ = measured pollutant concentration in flue-gases (ppmvd)

ppm$_{corr}$ = pollutant concentration corrected to a standard O_2 basis (ppmvd),

$O_{2,oxid}$ = O_2 concentration in the oxidizer (vol. %),

$O_{2,meas}$ = measured O_2 concentration in the flue gases (vol. %, dry basis)

$O_{2, basis}$ = standard O_2 basis

The standard O_2 basis is decided based on the type of the combustion system under consideration. It is set to 15% for stationary systems fueled by natural gas, 3% for aircraft engine gas turbine combustors etc [120,121].

Bibliography

[1]   EIA U. Annual energy outlook 2015: with projections to 2040. n.d.

[2]   Zeldovich YB. The oxidation of nitrogen in combustion and explosions. Acta Physicochim URSS 1946;21:577--628.

[3]   Lavoie GA, Heywood JB, Keck JC. Experimental and theoretical study of nitric oxide formation in internal combustion engines. Combust Sci Technol 1970;1:313–26. doi:10.1080/00102206908952211.

[4]   Atreya A, Baum HR. A Study of Radiative Flameless Combustion in a Furnace. ICHMT Digit Libr ONLINE Begel House Inc 2015:1221–34. doi:10.1615/ICHMT.2015.IntSympAdvComputHeatTransf.1150.

[5]   Cavaliere A, De Joannon M. Mild combustion. vol. 30. Elsevier; 2004. doi:10.1016/j.pecs.2004.02.003.

[6]   Dally BB, Riesmeier E, Peters N. Effect of fuel mixture on moderate and intense low oxygen dilution combustion. Combust Flame 2004;137:418–31. doi:10.1016/j.combustflame.2004.02.011.

[7]   Galletti C, Parente A, Tognotti L. Numerical and experimental investigation of a mild combustion burner. Combust Flame 2007;151:649–64. doi:10.1016/j.combustflame.2007.07.016.

[8]   Kumar S, Paul PJ, Mukunda HS. Studies on a New High-Intensity Low-Emission Burner. Proc. Combust. Inst., vol. 29, 2002, p. 1131–7.

[9]   Li P, Wang F, Mi J, Dally BB, Mei Z, Zhang J, et al. Mechanisms of NO formation in MILD combustion of CH4/H2 fuel blends. Int J Hydrogen Energy 2014;39:19187–203. doi:10.1016/j.ijhydene.2014.09.050.

[10] Özdemir, IB and Peters N. Characteristics of the reaction zone in a combustor operating at mild combustion. Exp Fluids 2001;30:683–95. doi:10.1007/s003480000248.

[11] Arghode VK, Gupta AK, Bryden KM. High intensity colorless distributed combustion for ultra low emissions and enhanced performance. Appl Energy 2012;92:822–30. doi:10.1016/j.apenergy.2011.08.039.

[12] Zhang H, Yue G, Lu J, Jia Z, Mao J, Fujimori T, et al. Development of high temperature air combustion technology in pulverized fossil fuel fired boilers. Proc Combust Inst 2007;31 II:2779–85. doi:10.1016/j.proci.2006.07.135.

[13] Gupta A. Flame characteristics and challenges with high temperature air combustion. Proccedings 2000 Int Jt Power Gener Conf Miami Beach, Florida, ASME 2000:1–18. doi:10.2514/6.2000-593.

[14] Arghode VK, Gupta AK. Development of high intensity CDC combustor for gas turbine engines. Appl Energy 2011;88:963–73. doi:10.1016/j.apenergy.2010.07.038.

[15] Khalil AEEE, Arghode VK, Gupta AK. Novel mixing for ultra-high thermal intensity distributed combustion. Appl Energy 2013;105:327–34. doi:10.1016/j.apenergy.2012.12.071.

[16] Arghode VK, Gupta AK. Effect of flow field for colorless distributed combustion (CDC) for gas turbine combustion. Appl Energy 2010;87:1631–40. doi:10.1016/j.apenergy.2009.09.032.

[17] Noguchi, Masaaki and Tanaka, Yukiyasu and Tanaka, Taro and Takeuchi Y. A study on gasoline engine combustion by observation of intermediate reactive products during combustion. 1979.

[18] Onishi, Shigeru and Jo, Souk Hong and Shoda, Katsuji and Do Jo, Pan and Kato S. Active thermo-atmosphere combustion (ATAC)-a new combustion process for internal combustion engines. 1979.

[19] Ishii H, Koike N, Suzuki H, Odaka M. Exhaust Purification of Diesel Engines by

Homogeneous Charge with Compression Ignition Part 2: Analysis of Combustion Phenomena and NOx Formation by Numerical Simulation with Experiment. Sae Tech Pap Ser 1997. doi:10.4271/970315.

[20] Najt PM, Foster DE. Compression-ignited homogeneous charge combustion. 1983.

[21] Suzuki H, Koike N, Ishii H, Odaka M. Exhaust Purification of Diesel Engines by Homogeneous Charge with Compression Ignition Part 1: Experimental Investigation of Combustion and Exhaust Emission Behavior Under Pre-Mixed Homogeneous Charge Compression Ignition Method. SAE Int J Engines 1997. doi:10.4271/970313.

[22] Krishnamurthy N, Paul PJ, Blasiak W. Studies on low-intensity oxy-fuel burner. Proc Combust Inst 2009;32 II:3139–46. doi:10.1016/j.proci.2008.08.011.

[23] Mancini M, Weber R, Bollettini U. Predicting NOx emissions of a burner operated in flameless oxidation mode. Proc Combust Inst 2002;29:1155–63. doi:10.1016/S1540-7489(02)80146-8.

[24] Plessing T, Peters N, Wünning JG. Laseroptical investigation of highly preheated combustion with strong exhaust gas recirculation. Symp Combust 1998;27:3197–204. doi:10.1016/S0082-0784(98)80183-5.

[25] Wünning J., Wünning J. Flameless oxidation to reduce thermal no-formation. Prog Energy Combust Sci 1997;23:81–94. doi:10.1016/S0360-1285(97)00006-3.

[26] Sánchez M, Cadavid F, Amell A. Experimental evaluation of a 20kW oxygen enhanced self-regenerative burner operated in flameless combustion mode. Appl Energy 2013;111:240–6. doi:10.1016/j.apenergy.2013.05.009.

[27] Tabacco D, Innarella C, Bruno C. Combustion Science and Technology THEORETICAL AND NUMERICAL INVESTIGATION ON FLAMELESS COMBUSTION. vol. 174. 2002. doi:10.1080/00102200290020796.

[28] Veríssimo AS, Rocha AMAA, Costa M. Operational, combustion, and emission characteristics of a small-scale combustor. Energy and Fuels 2011;25:2469–80. doi:10.1021/ef200258t.

[29] Wu KK, Chang YC, Chen CH, Chen Y Da. High-efficiency combustion of natural gas with 21-30% oxygen-enriched air. Fuel 2010;89:2455–62. doi:10.1016/j.fuel.2010.02.002.

[30] Wang L, Haworth DC, Turns SR, Modest MF. Interactions among soot, thermal radiation, and NOx emissions in oxygen-enriched turbulent nonpremixed flames: A computational fluid dynamics modeling study. Combust Flame 2005;141:170–9. doi:10.1016/j.combustflame.2004.12.015.

[31] Beltrame A, Porshnev P, Merchan-Merchan W, Saveliev A, Fridman A, Kennedy LA, et al. Soot and NO formation in methane-oxygen enriched diffusion flames. Combust Flame 2001;124:295–310. doi:10.1016/S0010-2180(00)00185-1.

[32] Li P, Dally BB, Mi J, Wang F. MILD oxy-combustion of gaseous fuels in a laboratory-scale furnace. Combust Flame 2013;160:933–46. doi:10.1016/j.combustflame.2013.01.024.

[33] Chen S, Zheng C. Counterflow diffusion flame of hydrogen-enriched biogas under MILD oxy-fuel condition. Int J Hydrogen Energy 2011;36:15403–13. doi:10.1016/j.ijhydene.2011.09.002.

[34] Liu Y, Chen S, Yang B, Liu K, Zheng C. First and second thermodynamic-law comparison of biogas MILD oxy-fuel combustion moderated by CO2 or H2O. Energy Convers Manag 2015;106:625–34. doi:10.1016/j.enconman.2015.09.076.

[35] Li P, Wang F, Tu Y, Mei Z, Zhang J, Zheng Y, et al. Moderate or intense low-oxygen dilution oxy-combustion characteristics of light oil and pulverized coal in a pilot-scale furnace. Energy and Fuels 2014;28:1524–35. doi:10.1021/ef402240w.

[36] Tu Y, Liu H, Su K, Chen S, Liu Z, Zheng C, et al. Numerical study of H$_2$O addition effects on pulverized coal oxy-MILD combustion. Fuel Process Technol 2015;138:252–62. doi:10.1016/j.fuproc.2015.05.031.

[37] Tu Y, Liu H, Chen S, Liu Z, Zhao H, Zheng C. Numerical study of combustion characteristics for pulverized coal under oxy-MILD operation. Fuel Process Technol 2015;135:80–90. doi:10.1016/j.fuproc.2014.10.025.

[38] Chen L, Yong SZ, Ghoniem AF. Oxy-fuel combustion of pulverized coal: Characterization, fundamentals, stabilization and CFD modeling. Prog Energy Combust Sci 2012;38:156–214. doi:10.1016/j.pecs.2011.09.003.

[39] Howell JR, Menguc MP, Siegel R. Thermal radiation heat transfer. 2015. doi:10.1533/9780857096081.73.

[40] Incropera FP, Lavine AS, Bergman TL, DeWitt DP. Fundamentals of heat and mass transfer. Wiley; 2007.

[41] Baukal Jr CE. The john zink combustion handbook. CRC press; 2001.

[42] Puri R, Santoro RJ, Smyth KC. The Oxidation of Soot and Carbon-Monoxide in Hydrocarbon Diffusion Flames. Combust Flame 1994;97:125–44. doi:10.1016/0010-2180(95)00045-8.

[43] Pourhoseini SH, Saeedi A, Moghiman M. Experimental and Numerical Study on the Effect of Soot Injection on NOx Reduction and Radiation Enhancement in a Natural Gas Turbulent Flame. Arab J Sci Eng 2013;38:69–75. doi:10.1007/s13369-012-0412-1.

[44] Brookes SJ, Moss JB. Measurements of soot production and thermal radiation from confined turbulent jet diffusion flames of methane. Combust Flame 1999;116:49–61. doi:10.1016/S0010-2180(98)00027-3.

[45] Al-Omari S-AB, Kawajiri K, Yonesawa T. Soot processes in a methane-fueled furnace and their impact on radiation heat transfer to furnace walls. Int J Heat Mass Transf 2001;44:2567–81. doi:10.1016/S0017-9310(00)00288-X.

[46] Effuggi A, Gelosa D, Derudi M, Rota R. Mild combustion of methane-derived fuel mixtures: Natural gas and biogas. Combust Sci Technol 2008;180:481–93. doi:10.1080/00102200701741368.

[47] Yang B, Koylu UO. Detailed soot field in a turbulent non-premixed ethylene/air flame from laser scattering and extinction experiments. Combust Flame 2005;141:55–65. doi:10.1016/j.combustflame.2004.12.008.

[48] Vander Wal RL, Weiland KJ. Laser-induced incandescence: Development and characterization towards a measurement of soot-volume fraction. Appl Phys B Laser Opt 1994;59:445–52. doi:10.1007/BF01081067.

[49] Williams TC, Shaddix CR, Jensen KA, Suo-Anttila JM. Measurement of the dimensionless extinction coefficient of soot within laminar diffusion flames. Int J Heat Mass Transf 2007;50:1616–30. doi:10.1016/j.ijheatmasstransfer.2006.08.024.

[50] Lee SC, Tien CL. Optical constants of soot in hydrocarbon flames. Symp Combust 1981;18:1159–66. doi:10.1016/S0082-0784(81)80120-8.

[51] Vaglieco BM, Beretta F, D'Alessio A. In situ evaluation of the soot refractive index in the UV-visible from the measurement of the scattering and extinction coefficients in rich flames. Combust Flame 1990;79:259–71. doi:10.1016/0010-2180(90)90138-H.

[52] Smyth K, Shaddix C. The elusive history of m= 1.57-0.56 i for the refractive index of soot. Combust Flame 2010;107:314–20. doi:10.1059/0003-4819-153-2-201007200-00257.

[53] Choi MY, Hamins A, Rushmeier H, Kashiwagi T. Simultaneous optical measurement of soot volume fraction, temperature, and CO2 in heptane pool fire. Symp Combust 1994;25:1471–80. doi:10.1016/S0082-0784(06)80791-5.

[54] Dalzell WH, Sarofim a. F. Optical Constants of Soot and Their Application to Heat-Flux Calculations. J Heat Transfer 1969;91:100. doi:10.1115/1.3580063.

[55] Wu JS, Krishnan SS, Faeth GM. Refractive indices at visible wavelengths of soot emitted from buoyant turbulent diffusion flames. J Heat Transfer 1997;119:230–7. doi:10.1115/1.2824213.

[56] Charalampopoulos TT, Chang H, Stagg B. The effects of temperature and composition on the complex refractive index of flame soot. Fuel 1989;68:1173–9. doi:10.1016/0016-2361(89)90191-9.

[57] Hu B, Yang B, Koylu UO. Soot measurements at the axis of an ethylene/air non-premixed turbulent jet flame. Combust Flame 2003;134:93–106.

doi:10.1016/S0010-2180(03)00085-3.

[58] Krishnan SS, Lin K-C, Faeth GM. Optical Properties in the Visible of Overfire Soot in Large Buoyant Turbulent Diffusion Flames. J Heat Transfer 2000;122:517–24. doi:10.1115/1.1288025.

[59] Yang B, Koylu UO. Soot processes in a strongly radiating turbulent flame from laser scattering/extinction experiments. J Quant Spectrosc Radiat Transf 2005;93:289–99. doi:10.1016/j.jqsrt.2004.08.026.

[60] Chang H, Charalampopoulos TT. Determination of the Wavelength Dependence of Refractive Indices of Flame Soot. Proc R Soc A Math Phys Eng Sci 1990;430:577–91. doi:10.1098/rspa.1990.0107.

[61] Charalampopoulos TT, Felske JD. Refractive indices of soot particles deduced from in-situ laser light scattering measurements. Combust Flame 1987;68:283–94. doi:10.1016/0010-2180(87)90005-8.

[62] Therssen E, Bouvier Y, Schoemaecker-Moreau C, Mercier X, Desgroux P, Ziskind M, et al. Determination of the ratio of soot refractive index function E(m) at the two wavelengths 532 and 1064 nm by laser induced incandescence. Appl Phys B Lasers Opt 2007;89:417–27. doi:10.1007/s00340-007-2759-7.

[63] Charalampopoulos TT, Chang H. In Situ Optical Properties of Soot Particles in the Wavelength Range from 340 nm to 600 nm. Combust Sci Technol 1988;59:401–21. doi:10.1080/00102208808947108.

[64] Köylü ÜÖ, Faeth GM. Spectral Extinction Coefficients of Soot Aggregates From Turbulent Diffusion Flames. J Heat Transfer 1996;118:415. doi:10.1115/1.2825860.

[65] Fenimore CP, Jones GW. Oxidation of soot by hydroxyl radicals. J Phys Chem 1967;71:593–7. doi:10.1021/j100862a021.

[66] Smith GP, Golden DM, Frenklach M, Moriarty NW, Eiteneer B, Goldenberg M, et al. GRI-Mech 3.0, 2000. URL Http//Www Me Berkeley Edu/Gri_mech n.d.

[67] Mi J, Li P, Dally BB, Craig RA. Importance of initial momentum rate and air-fuel

premixing on moderate or intense low oxygen dilution (MILD) combustion in a recuperative furnace. Energy and Fuels 2009;23:5349–56. doi:10.1021/ef900866v.

[68]   Szegö GG, Dally BB, Nathan GJ. Operational characteristics of a parallel jet MILD combustion burner system. Combust Flame 2009;156:429–38. doi:10.1016/j.combustflame.2008.08.009.

[69]   Khalil AEE, Gupta AK. The role of CO2 on oxy-colorless distributed combustion. Appl Energy 2017;188:466–74.

[70]   Mendiara T, Glarborg P. Reburn chemistry in oxy-fuel combustion of methane. Energy and Fuels 2009. doi:10.1021/ef9001956.

[71]   Wünning J. AJ. GA, Wünning J. AJ. GA. Flameless oxidation to reduce thermal no-formation. Prog Energy Combust Sci 1997;23:81–94. doi:10.1016/S0360-1285(97)00006-3.

[72]   Veríssimo AS, Rocha AMA, Costa M. Importance of the inlet air velocity on the establishment of flameless combustion in a laboratory combustor. Exp Therm Fluid Sci 2013;44:75–81. doi:10.1016/j.expthermflusci.2012.05.015.

[73]   Mi J, Li P, Zheng C. Numerical Simulation of Flameless Premixed Combustion with an Annular Nozzle in a Recuperative Furnace. Chinese J Chem Eng 2010;18:10–7. doi:10.1016/S1004-9541(08)60316-X.

[74]   Shin SJ. Homogeneous combustion and its application to industrial furnaces. University of Michigan, Ann Arbor, 2008. doi:10.1017/CBO9781107415324.004.

[75]   Lee I. An experimental and numerical study of confined non-reacting and reacting turbulent jets to facilitate homogeneous combustion in industrial furnaces. University of Michigan, Ann Arbor, 2015.

[76]   Tsuji H, Gupta AK, Hasegawa T, Katsuki M, Kishimoto K, Morita M. High temperature air combustion: from energy conservation to pollution reduction. CRC press; 2002. doi:10.2514/6.2003-4940.

[77]   Katsuki M, Hasegawa T. The science and technology of combustion in highly

preheated air. Symp. Combust., vol. 27, 1998, p. 3135–46.

[78]   Arghode VK, Gupta AK. Investigation of forward flow distributed combustion for gas turbine application. Appl Energy 2011;88:29–40. doi:10.1016/j.apenergy.2010.04.030.

[79]   Arghode VK, Gupta AK. Investigation of reverse flow distributed combustion for gas turbine application. Appl Energy 2011;88:1096–104. doi:10.1016/j.apenergy.2010.10.039.

[80]   Veríssimo AS, Rocha AMA, Costa M. Experimental study on the influence of the thermal input on the reaction zone under flameless oxidation conditions. Fuel Process Technol 2013;106:423–8. doi:10.1016/j.fuproc.2012.09.008.

[81]   Grandmaison EW, Yimer I, Becker HA, Sobiesiak A. The strong-jet/weak-jet problem and aerodynamic modeling of the CGRI burner. Combust Flame 1998;114:381–96. doi:10.1016/S0010-2180(97)00314-3.

[82]   Launder BE, Spalding DB. Mathematical models of turbulence. Academic press; 1972.

[83]   Kader BA. Temperature and concentration profiles in fully turbulent boundary layers. Int J Heat Mass Transf 1981;24:1541–4.

[84]   Raithby GD, Chui EH. A finite-volume method for predicting a radiant heat transfer in enclosures with participating media. ASME, Trans J Heat Transf 1990;112:415–23.

[85]   Modest MF. The weighted-sum-of-gray-gases model for arbitrary solution methods in radiative transfer. J Heat Transfer 1991;113:650–6.

[86]   Pope SB. An explanation of the turbulent round-jet/plane-jet anomaly. AIAA J 1978;16:279–81.

[87]   Magnussen BF, Hjertager BW. On the structure of turbulence and a generalized eddy dissipation concept for chemical reaction in turbulent flow. 19th AIAA Aerosp. Meet. St. Louis, USA, vol. 198, 1981.

[88]   Pope SB. Computationally efficient implementation of combustion chemistry using in situ adaptive tabulation. Combust Theory Model 1997;1:1:41–63. doi:https://doi.org/10.1080/713665229.

[89]   Evans MJ, Medwell PR, Tian ZF. Modeling lifted jet flames in a heated coflow using an optimized eddy dissipation concept model. Combust Sci Technol 2015;187:1093–109.

[90]   De A, Oldenhof E, Sathiah P, Roekaerts D. Numerical simulation of delft-jet-in-hot-coflow (djhc) flames using the eddy dissipation concept model for turbulence--chemistry interaction. Flow, Turbul Combust 2011;87:537–67.

[91]   Westbrook CK, Dryer FL. Simplified reaction mechanisms for the oxidation of hydrocarbon fuels in flames. Combust Sci Technol 1981;27:31–43.

[92]   Hussein HJ, Capp SP, George WK. Velocity measurements in a high-Reynolds-number, momentum-conserving, axisymmetric, turbulent jet. J Fluid Mech 1994;258:31–75. doi:10.1017/S002211209400323X.

[93]   Bowman CT, Hanson RK, Davidson DF, Gardiner WC, Lissianski V, Smith GP, et al. GRI-Mech 2.11, 1997. URL Http//Www Me Berkeley Edu/Gri_mech n.d.

[94]   Said A, Gupta AK. High Intensity Combustion of Methane and Propane using Oxygen Enhanced Air. 14th Int. Energy Convers. Eng. Conf., 2016, p. 4637.

[95]   Khalil AEE, Gupta AK. Flame fluctuations in Oxy-CO2-methane mixtures in swirl assisted distributed combustion. Appl Energy 2017;204:303–17.

[96]   Tu Y, Liu H, Chen S, Liu Z, Zhao H, Zheng C. Effects of furnace chamber shape on the MILD combustion of natural gas. Appl Therm Eng 2015;76:64–75. doi:10.1016/j.applthermaleng.2014.11.007.

[97]   Mahendra Reddy V, Kumar S. Development of high intensity low emission combustor for achieving flameless combustion of liquid fuels. Propuls Power Res 2013;2:139–47. doi:10.1016/j.jppr.2013.04.006.

[98]   Deng X, Xiong Y, Yin H, Gao Q. Numerical Study of the Effect of Nozzle

Configurations on Characteristics of MILD Combustion for Gas Turbine Application. J Energy Resour Technol 2016;138:1–8. doi:10.1115/1.4033141.

[99] Aanjaneya K, Cao W, Chen Y, Borgnakke C, Atreya A. A numerical study of confined turbulent jets for homogeneous combustion with oxygen enrichment. Fuel 2019;261:1–10. doi:10.1016/j.fuel.2019.116449.

[100] Callender B, Gutmark E, Martens S. Far-field acoustic investigation into chevron nozzle mechanisms and trends. AIAA J 2005;43:87–95. doi:10.2514/1.6150.

[101] Callender B, Gutmark E, Martens S. Near-field investigation of chevron nozzle mechanisms. AIAA J 2008;46:36–45. doi:10.2514/1.17720.

[102] W. Tam CK, M. Q. Zaman KB. Subsonic Jet Noise from Nonaxisymmetric and Tabbed Nozzles. AIAA J 2000;38:592–9. doi:10.2514/2.1029.

[103] Sheen HJ, Chen WJ, Jeng SY, Huang TL. Correlation of Swirl Number for a Radial-Type Swirl Generator. Exp Therm Fluid Sci 1996;12:444–51. doi:10.1016/0894-1777(95)00135-2.

[104] Khalil AE, Arghode VK, Gupta AK, Lee SC. Low calorific value fuelled distributed combustion with swirl for gas turbine applications. Appl Energy 2012;98:69–78. doi:10.1016/j.apenergy.2012.02.074.

[105] Khalil AEE, Gupta AK. Swirling flowfield for colorless distributed combustion. Appl Energy 2014;113:208–18. doi:10.1016/j.apenergy.2013.07.029.

[106] Khalil AEE, Gupta AK. Swirling distributed combustion for clean energy conversion in gas turbine applications. Appl Energy 2011;88:3685–93. doi:10.1016/j.apenergy.2011.03.048.

[107] Khalil AEE, Gupta AK. Distributed swirl combustion for gas turbine application. Appl Energy 2011;88:4898–907. doi:10.1016/j.apenergy.2011.06.051.

[108] Sorrentino G, Sabia P, De Joannon M, Cavaliere A, Ragucci R. The Effect of Diluent on the Sustainability of MILD Combustion in a Cyclonic Burner. Flow, Turbul Combust 2016;96:449–68. doi:10.1007/s10494-015-9668-3.

[109] Noor MM, Wandel AP, Yusaf T. Analysis of recirculation zone and ignition position of non-premixed bluff-body for biogas mild combustion. Int J Automot Mech Eng 2013;8:1176--1186.

[110] Khalil AEE, Gupta AK. Fostering distributed combustion in a swirl burner using prevaporized liquid fuels. Appl Energy 2018;211:513–22. doi:10.1016/j.apenergy.2017.11.068.

[111] Reddy VM, Katoch A, Roberts WL, Kumar S. Experimental and numerical analysis for high intensity swirl based ultra-low emission flameless combustor operating with liquid fuels. Proc Combust Inst 2015;35:3581–9. doi:10.1016/j.proci.2014.05.070.

[112] Karyeyen S, Feser JS, Gupta AK. Swirl assisted distributed combustion behavior using hydrogen-rich gaseous fuels. Appl Energy 2019;251:113354. doi:10.1016/j.apenergy.2019.113354.

[113] Karyeyen S, Feser JS, Gupta AK. Hydrogen concentration effects on swirl-stabilized oxy-colorless distributed combustion. Fuel 2019;253:772–80. doi:10.1016/j.fuel.2019.05.008.

[114] Feser JS, Karyeyen S, Gupta AK. Flowfield impact on distributed combustion in a swirl assisted burner. Fuel 2019:116643. doi:10.1016/j.fuel.2019.116643.

[115] Roy R, Gupta AK. Flame structure and emission signature in distributed combustion. Fuel 2020;262:116460. doi:10.1016/j.fuel.2019.116460.

[116] Launder BE, Reece GJ, Rodi W. Progress in the development of a Reynolds-stress turbulence closure. J Fluid Mech 1975;68:537–66. doi:10.1017/S0022112075001814.

[117] Gibson MM, Launder BE. Ground effects on pressure fluctuations in the atmospheric boundary layer. J Fluid Mech 1978;86:491–511. doi:10.1017/S0022112078001251.

[118] Launder BE. Second-moment closure: present... and future? Int J Heat Fluid Flow 1989;10:282–300. doi:10.1016/0142-727X(89)90017-9.

[119] Liu J, Chen S, Liu Z, Peng K, Zhou N, Huang X, et al. Mathematical modeling of air- and oxy-coal confined swirling flames on two extended eddy-dissipation models. Ind Eng Chem Res 2012;51:691–703. doi:10.1021/ie201430a.

[120] Baukal CE, Eleazer PB. Quantifying NOx for industrial combustion processes. J Air Waste Manag Assoc 1998;48:52–8. doi:10.1080/10473289.1998.10463664.

[121] U.S. Government. Protection of Environment - Code of Federal Regulations Title 40, Part 60. 1994.